

AD A104826

1
12

DNA 5418F

ANALYSIS OF SMALL-SCALE LABORATORY EXPERIMENTS OF DEEP-BASED STRUCTURES

Y. M. Ito

R. H. England

T. E. Wolverton

R. B. Nelson

California Research & Technology, Inc.

6269 Variel Avenue

Woodland Hills, California 91367

1 November 1978

Final Report for Period 20 May 1977—15 October 1978

CONTRACT Nos. DNA 001-77-C-0248

and DNA 001-78-C-0137

APPROVED FOR PUBLIC RELEASE;
DISTRIBUTION UNLIMITED.

THIS WORK SPONSORED BY THE DEFENSE NUCLEAR AGENCY
UNDER RDT&E RMSS CODES B344077464 Y99QAXSC06154 H2590D
AND B344078462 J34HAXSX31116 H2590D.

DNA FILE COPY

Prepared for

Director

DEFENSE NUCLEAR AGENCY

Washington, D. C. 20305

6 9 20 049

Destroy this report when it is no longer needed. Do not return to sender.

PLEASE NOTIFY THE DEFENSE NUCLEAR AGENCY,
ATTN: STI, WASHINGTON, D.C. 20305, IF
YOUR ADDRESS IS INCORRECT, IF YOU WISH TO
BE DELETED FROM THE DISTRIBUTION LIST, OR
IF THE ADDRESSEE IS NO LONGER EMPLOYED BY
YOUR ORGANIZATION.



UNCLASSIFIED

SECURITY CLASSIFICATION OF THIS PAGE (When Data Entered)

REPORT DOCUMENTATION PAGE		READ INSTRUCTIONS BEFORE COMPLETING FORM
1. REPORT NUMBER DNA/5418F	2. GOVT ACCESSION NO AD-A104	3. RECIPIENT'S CATALOG NUMBER 826
4. TITLE (and subtitle) ANALYSIS OF SMALL-SCALE LABORATORY EXPERIMENTS OF DEEP-BASED STRUCTURES.		5. TYPE OF REPORT & PERIOD COVERED Final Report, for Period 20 May 77-15 Oct 78.
7. AUTHOR(s) Y. Marvin Ito Russell H. England		6. PERFORMING ORG. REPORT NUMBER CRT-3210-1
8. CONTRACT OR GRANT NUMBER(s) DNA 001-77-C-0248 DNA 001-78-C-0137		9. PERFORMING ORGANIZATION NAME AND ADDRESS California Research & Technology, Inc. 6269 Variel Avenue Woodland Hills, California 91367
11. CONTROLLING OFFICE NAME AND ADDRESS Director Defense Nuclear Agency Washington, D.C. 20305		10. PROGRAM ELEMENT, PROJECT, TASK AREA & WORK UNIT NUMBERS Subtask Y99QAXSC06154 Subtask J34HAXSK31116
14. MONITORING AGENCY NAME & ADDRESS (if different from Controlling Office) DCNS-X311		12. REPORT DATE 1 November 1978
		13. NUMBER OF PAGES 122
		15. SECURITY CLASS. (of this report) UNCLASSIFIED
		15a. DECLASSIFICATION/DOWNGRADING SCHEDULE
16. DISTRIBUTION STATEMENT (of this Report) Approved for public release; distribution unlimited.		
17. DISTRIBUTION STATEMENT (of the abstract entered in Block 20, if different from Report)		
18. SUPPLEMENTARY NOTES This work sponsored by the Defense Nuclear Agency under RDT&E RMSS Codes B344077464 Y99QAXSC06154 H2590D and B344078462 J34HAXSX31116 H2590D.		
19. KEY WORDS (Continue on reverse side if necessary and identify by block number) Deep Basing Laboratory Tests Numerical Simulations Scale Models Static Tests NONSAP Structures Dynamic Tests Finite Element Models Rock Simulant Strain Rate Material Models Lined Tunnels Porewater Plasticity		
20. ABSTRACT (Continue on reverse side if necessary and identify by block number) Numerical simulations were performed in support of the SRI small-scale laboratory experiments of deep-based structures. The experiments, in which small cylinders of rock simulant SRI RMG 2C2 with lined tunnels were loaded statically and dynamically to represent deep-based structure response, were investigated analytically by use of the CRT/NONSAP nonlinear finite element computer code. The computer code, which employed refined material models for the rock simulant was used to simulate the SRI test procedure for both static		

UNCLASSIFIED

SECURITY CLASSIFICATION OF THIS PAGE (When Data Entered)

20. Abstract (continued)

and dynamic loading and the free-field (in-situ) behavior of deep-based structures.

Results show that the primary physical parameter in structural response is the lateral confinement of the test specimen. Tunnel response is shown to be highly sensitive to underconfinement, although relatively insensitive to moderate overconfinement. The SRI test procedure provides slight overconfinement in static tests designed to represent the uniaxial strain free-field conditions. Therefore, the static test gives a good estimate of tunnel closure under uniaxial strain conditions. The static isotropic (hydrostatic) loading gives smaller (less conservative) tunnel closures than uniaxial strain loading.

Tunnel closures in dynamic loading tests were observed to be much smaller than in comparable static loading tests. Based on experimental and numerical results the reduction in dynamic closures are most likely the result of strain-rate material effect, porewater pressure and overconfinement. The accuracy of the SRI test facility in indicating the response of actual deep-based structures in a dynamic environment cannot be determined given the unresolved questions of material behavior and confinement. Because of this uncertainty it is recommended that the SRI dynamic tests for tunnel closure *not* be continued. However, since strain-rate material effects, as well as porewater pressure, appear to be significant, it is recommended that static and dynamic tests of *solid* specimens of site material and rock simulant be conducted by SRI to provide valuable material property data.

UNCLASSIFIED

SUMMARY

S-1 BACKGROUND

Test facilities have been developed at SRI International with the objective of providing inexpensive small-scale experimental techniques capable of investigating the response of deep-based tunnel structures to underground loadings. The two SRI experimental facilities utilize a small 4 to 12 inch diameter cylindrical rock specimen into which is cast, perpendicular to the axis of the cylinder, a 5/8 to 2 inch cylindrical tunnel liner, as shown in Figure S-1. These scale models of tunnel/rock structure are subjected to specified (static or dynamic) pressure loads, P_V and P_H in Figure S-1, on the ends of the test cylinder and on its lateral surface.

This report presents an analysis performed in support of the SRI experimental program with the primary objective being to evaluate the capability of the test apparatus to represent the response of deep-based tunnel structures. In order to meet this objective, it was necessary to first develop an understanding of the actual experiments and to then isolate the most significant aspects of the SRI test procedure as a representation of actual field conditions.

Of the various modeling questions associated with the SRI experiments the ones which were believed most important, and which received the most attention in the present investigation were the following:

- (1) Given the applied vertical pressure, what is the effect of lateral confinement and how is this effect taken into account in the SRI tests?
- (2) What is the sensitivity of the material variability on the test results?

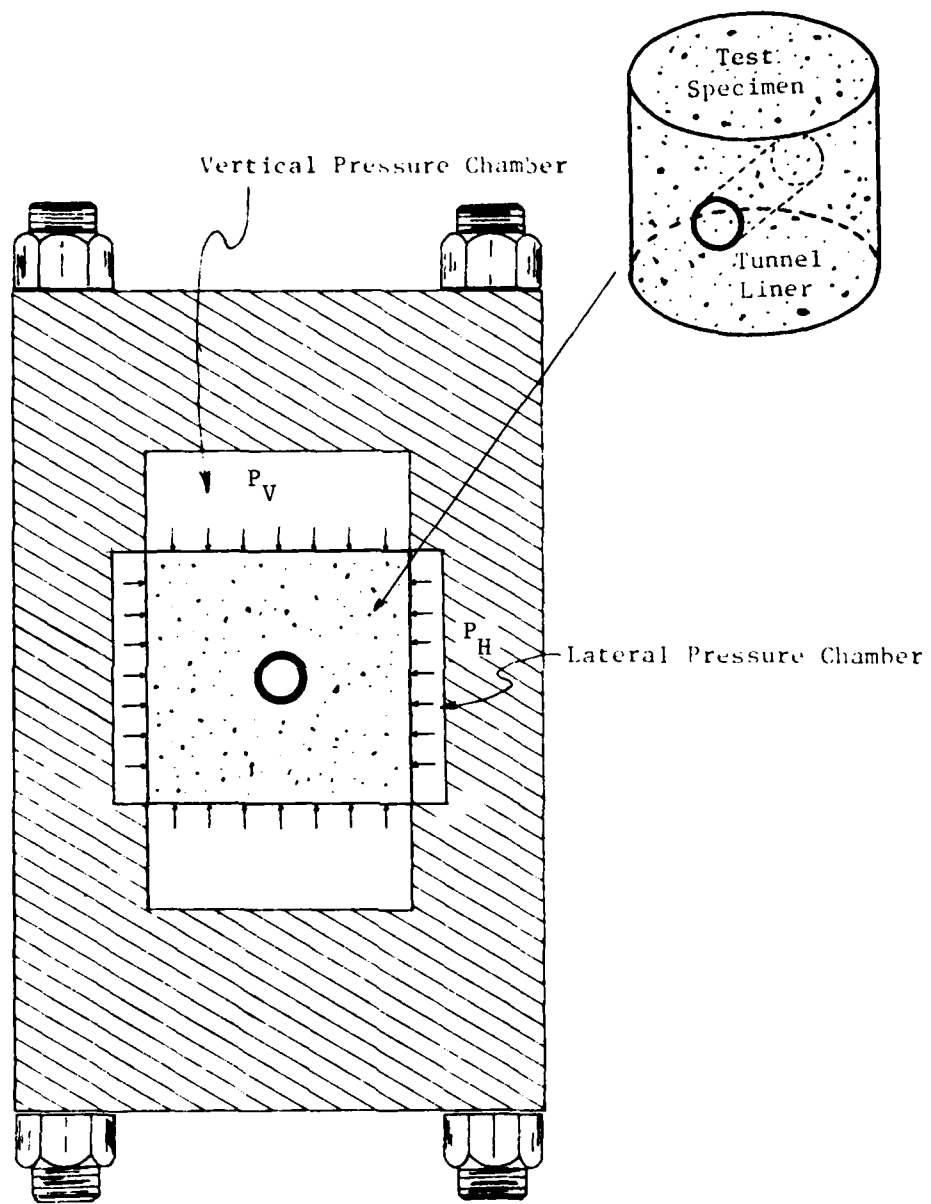


Figure S-1. Schematic of SRI Triaxial Test Apparatus.

(3) What is the significance of SRI test results in regard to actual deep-based structural response?

Although all these questions pertain to the SRI tests, the first one is of primary consideration in evaluating the capability of the test facility. The last two are, in addition, important questions which must be dealt with in order to design deep-based structures.

In order to answer these questions and to evaluate the SRI small-scale test facility, a comprehensive analysis program was established using as the basis the CRT/NONSAP finite element nonlinear analysis code. Several finite element models were employed using plane strain and *generalized* plane strain elastic-plastic representations of the rock simulant/tunnel structure. These computer models were used to analyze the results of the SRI test facility for both dynamic and static loadings.

S-2 DISCUSSION OF RESULTS

Under the initial program, plane strain finite element analyses of certain of the SRI small-scale tunnel response experiments were performed. The general objective was to help understand and interpret the significance of some of the observations from the nominally uniaxial strain loading tests. In particular, substantially smaller tunnel distortions were observed in dynamic-loaded tunnels as compared to static-loaded tunnels.

Figure S-2 summarizes the most important results of the preliminary analyses. Using the available material property data (from the SRI experiments), the plane strain analyses essentially duplicated the tunnel closure versus applied stress observed by SRI in static uniaxial strain test SUX-103. Then, using the same properties but loading the tunnel along the moderately *overconfined* stress path which occurred in SRI dynamic test DUX-77, the observed

LINED TUNNEL IN SRI DRY RMG 2C2 (SCALE MODEL)
COMPARISON OF CLOSURE

15

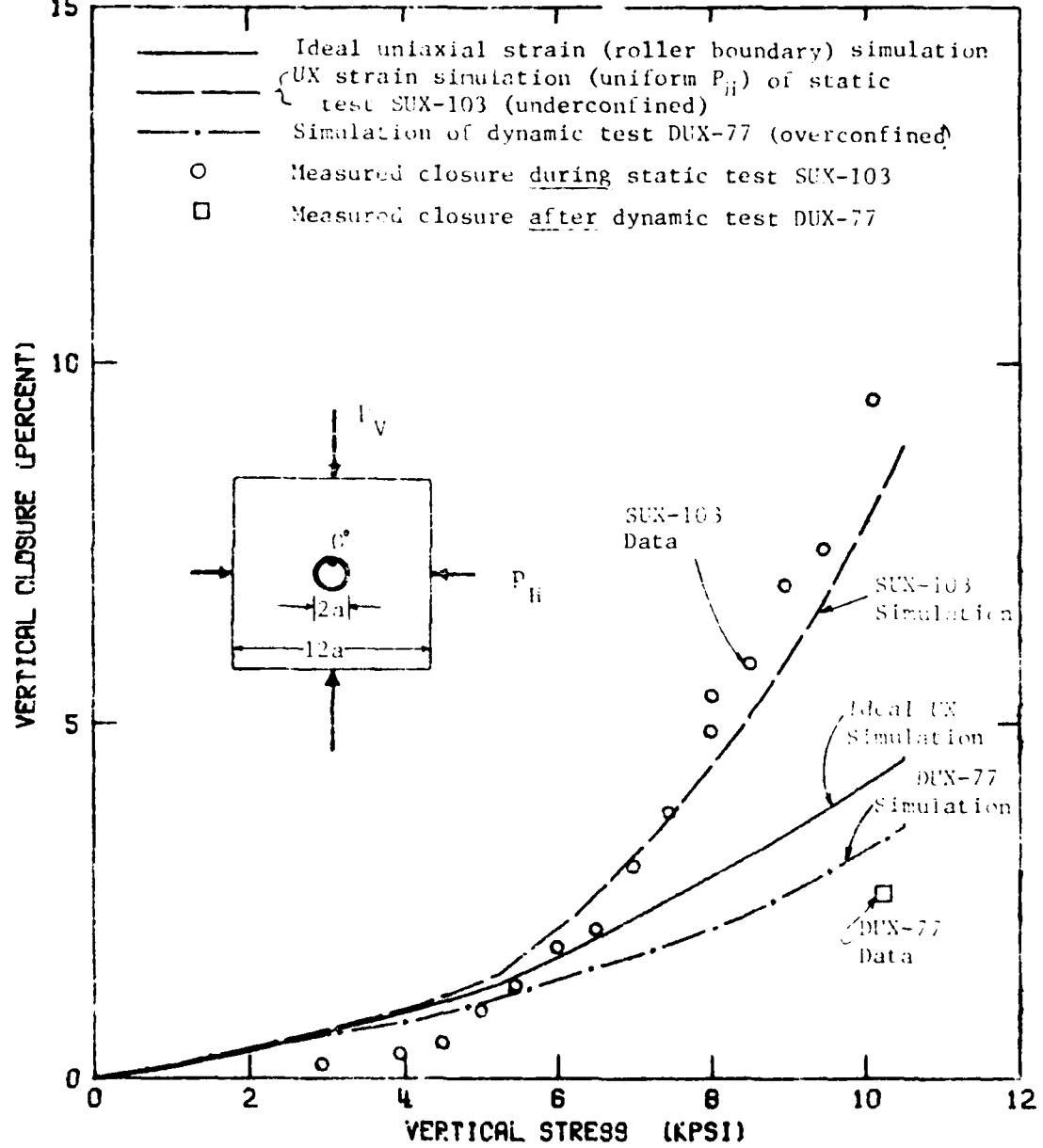


Figure S-2. Preliminary Analysis Comparison of Experimental and Theoretical Crown Closure in SRI RMG 2C2.

closure in that test was also essentially duplicated by numerical analyses. In both cases, the results may have been fortuitous, so additional analyses were clearly desirable before firm conclusions could be drawn. However, these results are self-consistent, and they do suggest that the differences in lateral confinement could be responsible for the differences in the static-dynamic results. As a corollary, the results suggest that tunnel response may be sensitive to the degree of lateral confinement. This could be important to buried structure design criteria.

The results of the generalized plane strain numerical calculations demonstrate the usefulness of theoretical analyses for interpretation of deep-based tunnel structures. The analytical results are in good agreement with experimental, given the uncertainty in material behavior. For example, Figures S-3 and S-4 compare the numerical and experimental crown tunnel closure and lateral strain variation with lateral confinement. The experimental and calculated results show similar trends, with the calculated closure being consistently less than the experimental.

These differences between theoretical and experimental results are well within the range of material variability typical of SRI RMG 2C2. From the analyses of the effect of material behavior on tunnel response, it appears that (for a given confinement) material strain rate is the dominant effect in reducing tunnel closure in dynamic tests and porewater pressure is the dominant effect in increasing tunnel closure in static tests.

Perhaps the most significant question in regard to the SRI test apparatus is its capabilities to simulate the response of actual deep-based tunnels. To evaluate and interpret the effectiveness of the SRI experiment, numerical calculations were performed to isolate and identify discrepancies that could occur between ideal free-field tests and SRI tests performed on finite samples. Thus,

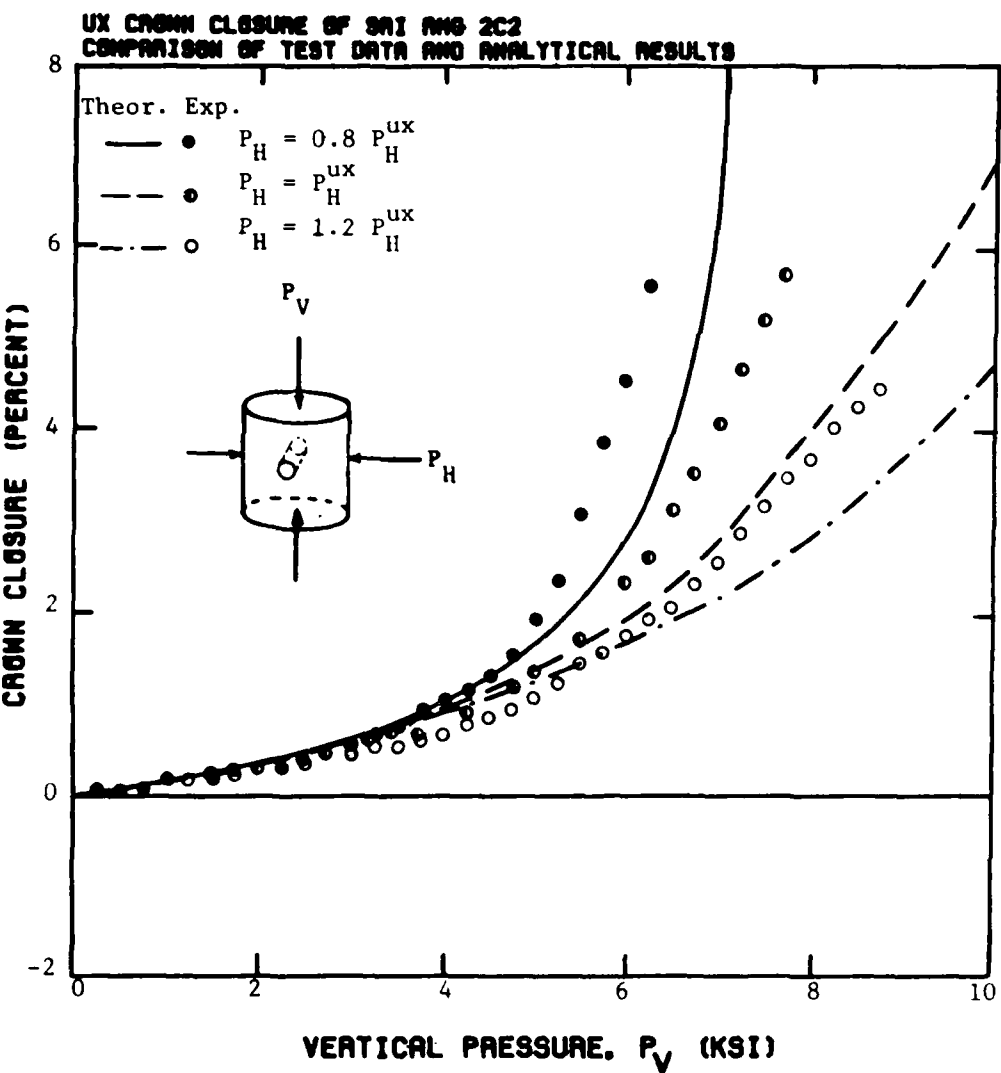


Figure S-3. Comparison of Experimental and Theoretical Crown Closure in SRI RMG 2C2 for Uniaxial Strain, Overconfined and Underconfined Loadings. (Aluminum liner, $a/h = 11.5$. P_H^{UX} is lateral pressure required to maintain uniaxial strain as defined by SRI.)

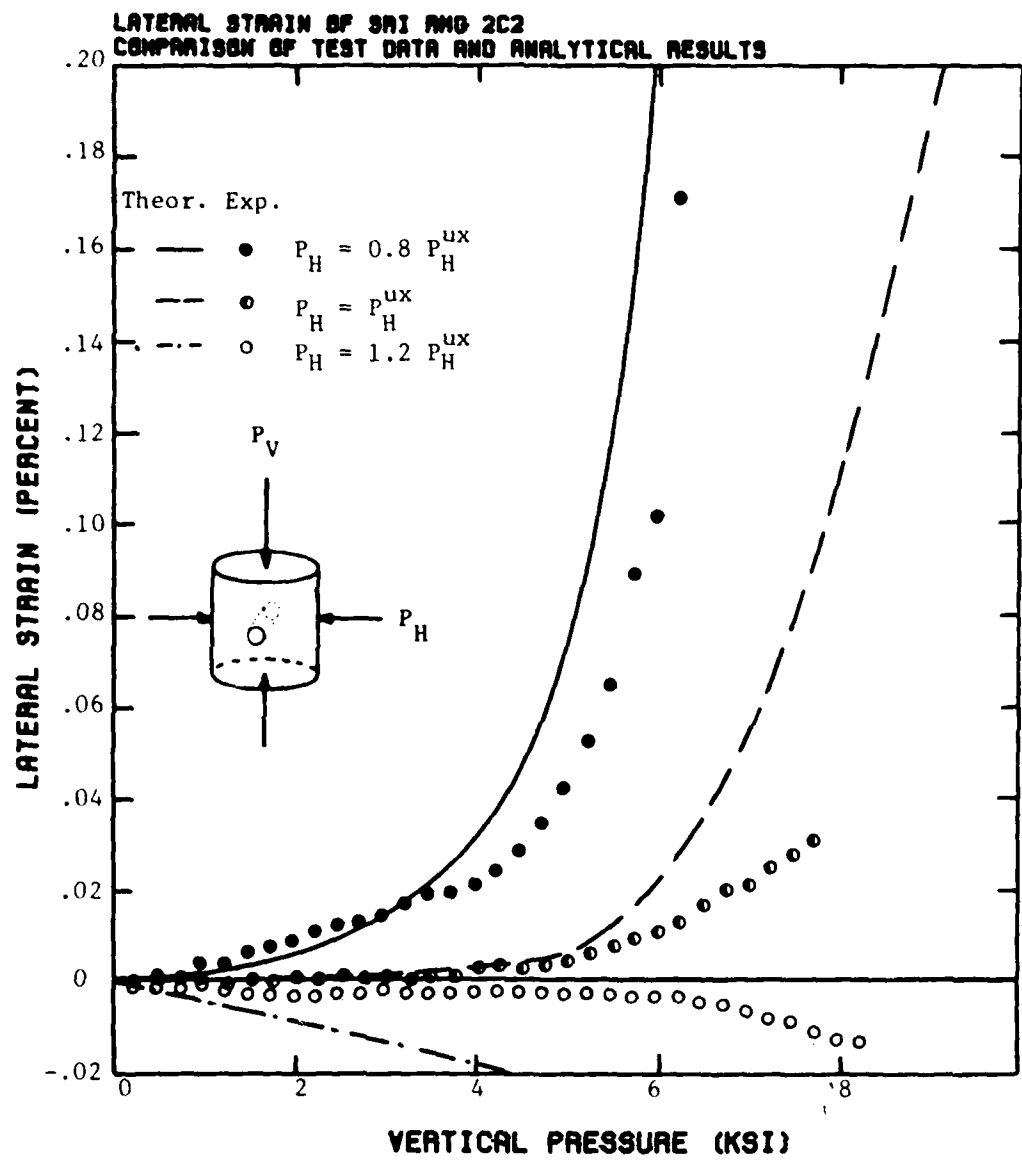


Figure S-4. Comparison between Experimental and Theoretical Specimen Lateral Strain at Mid-Height Versus Vertical Pressure, for Uniaxial Strain, Over-confined and Underconfined Loadings of SRI RMG 2C2. ($\bar{a}/h = 11.5$. P_H^{ux} is lateral pressure required to maintain uniaxial strain as defined by SRI.)

several analyses were performed using finite element grids where the boundaries were far removed from the tunnel. These analyses indicate a slightly overconfined condition along the surface of the SRI test specimen, as compared to the associated free-field surface.

In order to show the sensitivity of tunnel closure to confinement, the results of the present study are re-plotted in Figure S-5 and compared with four definitions of neutral confinement. Examining Figure S-5 shows tunnel closures to be extremely sensitive to underconfinement using all four definitions of neutral confinement. These results also show that the definition of neutral confinement can significantly influence the behavior of tunnel closure (and lateral boundary) response. On the other hand, as the test specimen is overconfined, the tunnel *crown* closure approaches that for the ideal uniaxial strain (roller) boundary state. The isotropic (hydrostatic) loading condition gives smaller (less conservative) tunnel closures than uniaxial strain loading.

These analyses support the general validity of the SRI experiments as a means for predicting tunnel response of an idealized uniaxial strain test under a *static* loading environment. (However, some of the results, specifically lateral boundary behavior appear inconsistent. For example, numerical analyses of the SRI simulated uniaxial strain test indicate that significant lateral bulging occurs especially at high pressure levels. This leads to the obvious question as to how the SRI test appears to deviate from the ideal uniaxial strain configuration, yet give tunnel closures which are essentially equal.) This follows from the fact that lateral boundary behavior has only a secondary effect on tunnel closures when *overconfined*. Thus, any simulated uniaxial strain test that is slightly overconfined will essentially duplicate tunnel response of ideal uniaxial strain tests.

EFFECTS OF LATERAL CONFINEMENT STRESS ON CROWN CLOSURES
VDP/SHIP

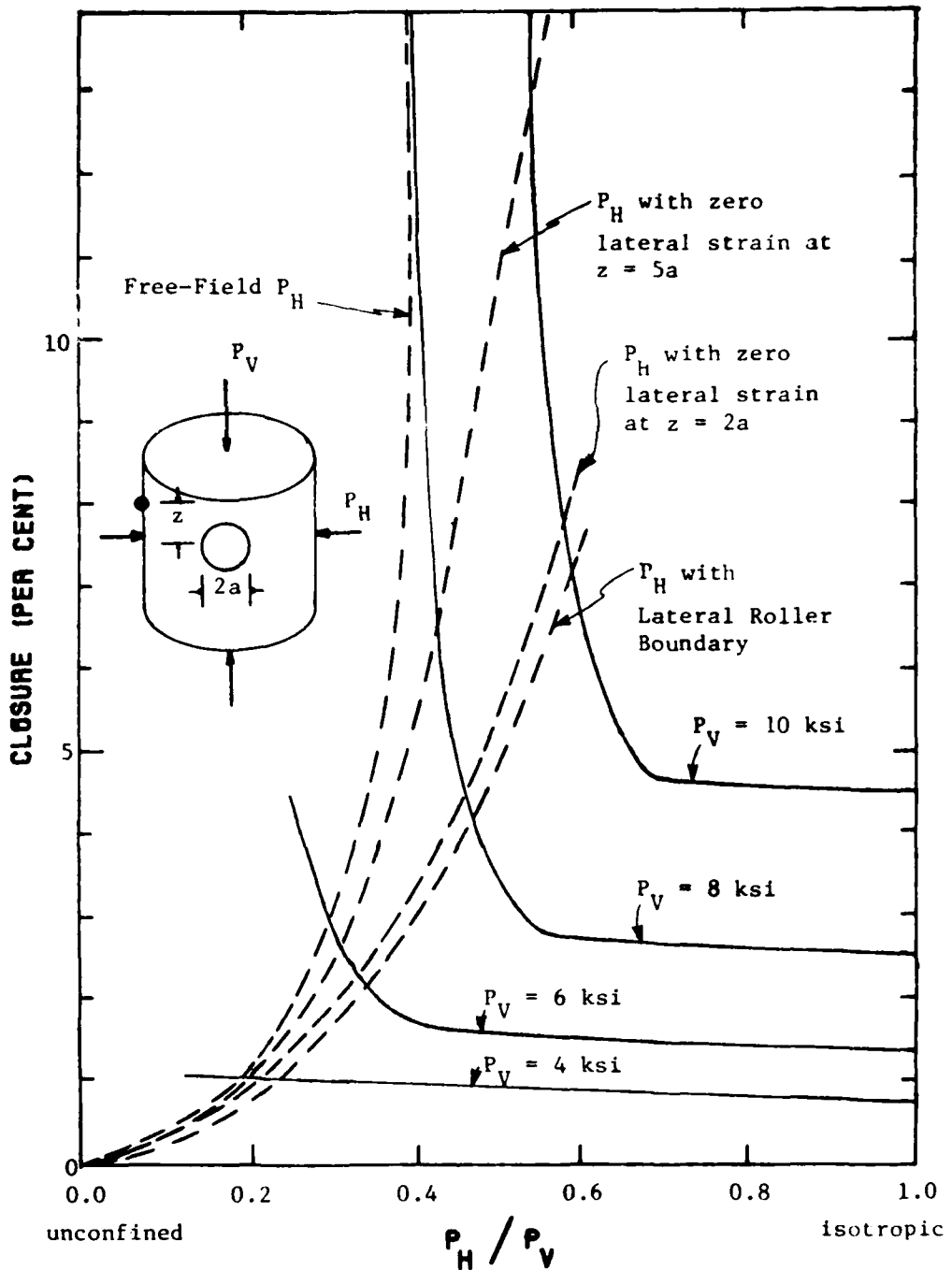


Figure S-5. Sensitivity of Tunnel Crown Closure to Lateral Confinement Pressure for SRI RMG 2C2 Specimen with Aluminum Liner, $\bar{a}/h = 11.5$.

S-3 RECOMMENDATIONS

The present analyses of the SRI tests support the capability of the uniaxial strain test in predicting ideal free-field tunnel closure for *static* loads. These tunnel closure results are, however, very sensitive to lateral (under) confinement, which SRI controls through instrumentation at two boundary stations. It is recommended that this lateral confinement be more carefully controlled by instrumenting the specimens at several stations and controlling maximum lateral deformation to insure that overconfinement will always be present. It should be recognized that as overconfinement increases, vertical tunnel closure decreases. Therefore, in order for the test to be relatively conservative, it is necessary for the tests to be *only slightly* overconfined.

Since lateral confinement in the SRI dynamic loading test facility is difficult if not impossible to control and since dynamical material property data is not available for either tuff or rock simulant, it is not possible to evaluate the capability of the SRI test to simulate far field dynamical response. Given these uncertainties, it is not possible to support additional dynamical tests for tunnel response using the SRI test facility.

However, since a knowledge of rate-dependent material properties of both tuff and rock simulant is of fundamental importance to the determination of deep-based structural response to dynamical loads, it is recommended that the SRI facility be used to determine the response of *solid* specimens to dynamical loads. In this way a data base can be established which will be essential for determining the dynamical material properties necessary for analyzing and designing dynamically loaded deep-based structures.

PREFACE

This report describes a two part investigation performed for the Defense Nuclear Agency under Contracts DNA001-77-C-0248 and DNA001-78-C-0137 during the period 20 May 1977 through 15 October 1978. The technical monitors for this investigation were LTC John C. Galloway and Dr. Kent L. Goering.

The authors wish to acknowledge the support provided by Kenneth N. Kreyenhagen who supervised this investigation and the valuable discussions with Herbert E. Lindberg and Paul E. Senseny of SRI International.

Conversion Factors for U.S. Customary
to Metric (SI) Units of Measurement

To Convert From	To	Multiply By
angstrom	meters (m)	1.000 000 X E -10
atmosphere (normal)	kilo pascal (kPa)	1.013 25 X E +2
bar	kilo pascal (kPa)	1.000 000 X E +2
barn	meter ² (m ²)	1.000 000 X E -28
British thermal unit (thermochemical)	joule (J)	1.054 350 X E +3
calorie (thermochemical)	joule (J)	4.184 000
cal (thermochemical)/cm ²	mega joule/m ² (MJ/m ²)	4.184 000 X E -2
curie	giga becquerel (GBq)*	3.700 000 X E +1
degree (angle)	radian (rad)	1.745 329 X E -2
degree Fahrenheit	degree kelvin (K)	$T_K = (t^{\circ} F + 459.67)/1.8$
electron volt	joule (J)	1.602 19 X E -19
erg	joule (J)	1.000 000 X E -7
erg/second	watt (W)	1.000 000 X E -7
foot	meter (m)	3.048 000 X E -1
foot-pound-force	joule (J)	1.355 818
gallon (U.S. liquid)	meter ³ (m ³)	3.785 412 X E -3
inch	meter (m)	2.540 000 X E -2
jerk	joule (J)	1.000 000 X E +9
joule/kilogram (J/kg) (radiation dose absorbed)	Gray (Gy)**	1.000 000
kilotons	terajoules	4.183
kip (1000 lbf)	newton (N)	4.448 222 X E +3
kip/inch ² (ksi)	kilo pascal (kPa)	6.894 757 X E +3
ktap	newton-second/m ² (N-s/m ²)	1.000 000 X E +2
micron	meter (m)	1.000 000 X E -6
mil	meter (m)	2.540 000 X E -5
mile (international)	meter (m)	1.609 344 X E +3
ounce	kilogram (kg)	2.834 952 X E -2
pound-force (lbf avoirdupois)	newton (N)	4.448 222
pound-force inch	newton-meter (N-m)	1.129 848 X E -1
pound-force/inch	newton/meter (N/m)	1.751 268 X E +2
pound-force/foot ²	kilo pascal (kPa)	4.788 026 X E -2
pound-force/inch ²	kilo pascal (kPa)	6.894 757
pound-mass (lbf avoirdupois)	kilogram (kg)	4.535 924 X E -1
pound-mass-foot ² (moment of inertia)	kilogram-meter ² (kg/m ³)	1.601 846 X E +1
rad (radiation dose absorbed)	Gray (Gy)**	1.000 000 X E -2
roentgen	coulomb/kilogram (C/kg)	2.579 760 X E -4
shake	second (s)	1.000 000 X E -8
slug	kilogram (kg)	1.459 390 X E +1
torr (mm Hg, 0° C)	kilo pascal (kPa)	1.333 22 X E -1

*The becquerel (Bq) is the SI unit of radioactivity; 1 Bq = 1 event/s.

**The Gray (Gy) is the SI unit of absorbed radiation.

A more complete listing of conversions may be found in "Metric Practice Guide E 380-74,"
American Society for Testing and Materials.

TABLE OF CONTENTS

<u>Section</u>	<u>Page</u>
SUMMARY - - - - -	1
S-1 Background - - - - -	1
S-2 Discussion of Results - - - - -	3
S-3 Recommendations - - - - -	10
PREFACE - - - - -	11
LIST OF ILLUSTRATIONS - - - - -	15
1 INTRODUCTION - - - - -	21
1.1 Review of SRI Small-Scale Test Facility - - - - -	21
1.2 Review of SRI Test Procedure - - - - -	24
1.3 Review of SRI Small-Scale Experiments - - - - -	25
1.4 Review of SRI RMG 2C2 Material Data - - - - -	27
1.5 Objectives of Numerical Investigation - - - - -	32
1.6 Report Organization - - - - -	33
2 MATHEMATICAL MODELS FOR ROCK SIMULANT, SRI RMG 2C2 - -	34
2.1 Background - - - - -	34
2.2 Drucker-Prager Model - - - - -	34
2.3 Variable Friction Angle, Strain Hardening Drucker-Prager Material Model - - - - -	37
2.4 Modified Mohr-Coulomb Material Model - - - - -	42
3 FINITE ELEMENT MODELS OF UNIAXIAL STRAIN LOADING EXPERIMENTS - - - - -	44
4 PRELIMINARY NUMERICAL ANALYSIS OF SRI EXPERIMENTS - -	48
5 IDEAL FREE-FIELD SIMULATION - - - - -	58
6 EFFECT OF MATERIAL BEHAVIOR ON TUNNEL RESPONSE - - -	64
6.1 Effect of Material Property Variations - - - - -	64
6.2 Rate Effects - - - - -	67
7 SENSITIVITY OF TUNNEL RESPONSE TO LATERAL CONFINEMENT - - - - -	75
8 NUMERICAL SIMULATION OF STATIC UNIAXIAL STRAIN EXPERIMENTS - - - - -	85

TABLE OF CONTENTS (continued)

<u>Appendix</u>	<u>Page</u>
A COMBINED VARIABLE FRICTION ANGLE AND STRAIN HARDENING DRUCKER-PRAGER MATERIAL MODEL - - - - -	95
B ELASTIC-PLASTIC MODIFIED MOHR-COULOMB MATERIAL MODEL - - - - -	103
REFERENCES - - - - -	115

LIST OF ILLUSTRATIONS

<u>Figure</u>		<u>Page</u>
S-1	Schematic of SRI Triaxial Test Apparatus - - - - -	2
S-2	Preliminary Analysis Comparison of Experimental and Theoretical Crown Closure in SRI RMG 2C2 - - - - -	4
S-3	Comparison of Experimental and Theoretical Crown Closure in SRI RMG 2C2 for Uniaxial Strain, Overconfined and Underconfined Loadings. (Aluminum liner, $a/h = 11.5$. P_H^X is lateral pressure required to maintain uniaxial strain as defined by SRI.) - - - - - - - - - - - - - - - - -	6
S-4	Comparison between Experimental and Theoretical Specimen Lateral Strain at Mid-Height Versus Vertical Pressure, for Uniaxial Strain, Overconfined and Underconfined Loadings of SRI RMG 2C2. (Aluminum liner, $a/h = 11.5$. P_H^X is lateral pressure required to maintain uniaxial strain as defined by SRI.) - - - - - - - - - - - - - - - - -	7
S-5	Sensitivity of Tunnel Crown Closure to Lateral Confinement Pressure for SRI RMG 2C2 Specimen with Aluminum Liner, $a/h = 11.5$ - - - - - - - - - - -	9
1.1	Schematic of SRI Triaxial Test Apparatus - - - - -	22
1.2	Various Loading Conditions Possible with the SRI Static Test Apparatus - - - - - - - - - - -	23
1.3	Comparison of an Ideal Uniaxial Strain Condition with the SRI Simulated Uniaxial Strain Test - - - - -	26
1.4	Vertical Tunnel Closure Versus Applied Vertical Pressure for Uniaxial Strain Loading of SRI RMG 2C2. Liner: 6061-T0 Aluminum, $a/h = 11.5$ From SRI [5] - - - - - - - - - - - - - - - - -	28
1.5	Tunnel Closure Versus Applied Pressure for Isotropic Loading of SRI RMG 2C2. Liner: 6061-T0 Aluminum, $a/h = 11.5$ From SRI [5] - - - - - - - - - - -	29
1.6	Lateral Confining Pressure Versus Vertical Pressure Needed to Maintain Uniaxial Strain Conditions in SRI RMG 2C2. From SRI [5] - - - - - - - - - - -	30

LIST OF ILLUSTRATIONS (continued)

<u>Figure</u>		<u>Page</u>
2.1	II-Plane Comparison of Various Yield Functions - - -	36
2.2	Preliminary Analysis Comparison of Analytical and Numerical Results for the Drucker-Prager Model - - - - -	38
2.3	Comparison of Typical Experimental Failure and Yield Surface Data with a Perfectly-Plastic Drucker-Prager Model- - - - -	39
2.4	Comparison of Typical Unconfined Stress-Strain Data with Perfectly-Plastic Drucker-Prager and Mohr-Coulomb Models - - - - -	39
2.5	Comparison of Typical Uniaxial Strain Loading Applied Stress-Confinement Stress Data with Perfectly-Plastic Drucker-Prager and Mohr-Coulomb Models- - - - -	41
2.6	Uniaxial Strain, Applied Stress-Confinement Stress for Perfectly-Plastic Drucker-Prager and Mohr-Coulomb Material Models- - - - -	41
3.1	Comparison of the SRI Simulated Uniaxial Strain Test with Free-Field Condition- - - - -	45
3.2	Comparison of the Plane Strain and the Generalized Plane Strain Models Used to Simulate the SRI Uniaxial Strain Experiments - - - - -	47
4.1	SRI Vertical Closure Data for Static and Dynamic Uniaxial Strain Loading of SRI RMG 2C2- - - - -	49
4.2	CRT/NONSAP Material Model Fit to SRI Test Data on Dry Sample (SUX-103) - - - - -	50
4.3	Numerical Simulation of Static Test SUX-103, using Roller and Pressure Boundary Conditions- - - - -	51
4.4	Numerical Analysis of Crown Closure Comparison between Dry SRI RMG 2C2 having Cylinder to Tunnel Diameter Ratios of 8/1 and 6/1- - - - -	52

3

LIST OF ILLUSTRATIONS (continued)

<u>Figure</u>		<u>Page</u>
4.5	Numerical Simulation of Dynamic Test DUX-77, using Simple Linear Loading Path and Actual Fit to Measured Path- - - - -	53
4.6	Loading Paths for Numerical Simulations of SRI Static and Dynamic Tests- - - - -	55
4.7	Preliminary Analysis Comparison of Experimental and Theoretical Crown Closure in SRI RMG 2C2- - -	56
5.1	Comparison of Tunnel Crown Closures for Plane Strain and Generalized Plane Strain Analyses with Boundary Conditions Applied at 18a - - - - -	59
5.2	Comparison of Tunnel Springline Closures for Plane Strain and Generalized Plane Strain Analyses with Boundary Conditions Applied at 18a- -	60
5.3	Stress Distribution at 6a Boundary for the Generalized Plane Strain Analysis with Roller Boundaries at 18a - - - - -	62
5.4	Strain Distribution at 6a Boundary for the Generalized Plane Strain Analysis with Roller Boundaries at 18a - - - - -	63
6.1	Failure Envelopes for MIGHTY EPIC/DIABLO HAWK Tuff and Grout Simulants. From SRI [5] - - - - -	65
6.2	Variations in Material Properties for Sensitivity Study - - - - -	66
6.3	Effects of Material Property Variations on the Confinement Stress at the 6.4a Boundary - - - - -	68
6.4	Effects of Material Property Variations on Tunnel Crown Closures- - - - -	69
6.5	Effects of Material Property Variations on Tunnel Springline Closures - - - - -	70
6.6	Comparison of Inertia and Strain Rate Effects for Dynamic Hydrostatic Loading Simulations - - - - -	73

LIST OF ILLUSTRATIONS (continued)

<u>Figure</u>		<u>Page</u>
7.1	Ratios of Applied Stress/Confinement Stress Used for Sensitivity Study- - - - -	77
7.2	Sensitivity Effect of Lateral Confinement Pressures on Tunnel Crown Closures- - - - -	78
7.3	Sensitivity Effect of Lateral Confinement Pressures on Tunnel Springline Closures - - - - -	79
7.4	Lateral Confinement Pressure Sensitivity Effects on the Strain Profile at the 6.4a Boundary for a Vertical Applied Pressure of 8 ksi- - - - -	80
7.5	Sensitivity of Tunnel Crown Closure to Lateral Confinement Pressure for SRI RMG 2C2 Specimen with Aluminum Liner, $a/h = 11.5$ - - - - -	81
7.6	Comparison of Experimental and Theoretical Crown Closure in SRI RMG 2C2 for Uniaxial Strain, Over- confined and Underconfined Loadings. (Aluminum liner, $a/h = 11.5$. P_{H^X} is lateral pressure required to maintain uniaxial strain as defined by SRI.)- - - - -	83
7.7	Comparison between Experimental and Theoretical Specimen Lateral Strain at Mid-Height Versus Vertical Pressure, for Uniaxial Strain, Over- confined and Underconfined Loadings of SRI RMG 2C2. (Aluminum liner, $a/h = 11.5$. p_{ux} is lateral pressure required to maintain uniaxial strain as defined by SRI.)- - - - -	84
8.1	Effects of the Tunnel on the Confinement Stress at the 6.4a Boundary- - - - -	86
8.2	Comparison of Tunnel Crown Closures for Plane Strain and Generalized Plane Strain Analyses with Boundary Conditions Applied at 6.4a- - - - -	87
8.3	Comparison of Tunnel Springline Closures for Plane Strain and Generalized Plane Strain Anal- yses with Boundary Conditions Applied at 6.4a - - -	88

LIST OF ILLUSTRATIONS (continued)

<u>Figure</u>		<u>Page</u>
8.4	Strain Distribution at the 6.4a Boundary for the Plane Strain Analysis with Roller Boundaries at 6.4a - - - - -	89
8.5	Strain Distribution at the 6.4a Boundary for the Generalized Plane Strain Analysis with Stress Boundaries at 6.4a - - - - -	90
8.6	Stress Distribution at the 6.4a Boundary for the Plane Strain Analysis with Roller Boundaries at 6.4a - - - - -	92
8.7	Stress Distribution at the 6.4a Boundary for the Generalized Plane Strain Analysis with Stress Boundaries at 6.4a - - - - -	93
A-1	Comparison of Failure and Yield Surfaces for the Combined Variable Friction Angle and Strain Hardening Versus Perfectly-Plastic Drucker-Prager Models of SRI RMG 2C2. ($\nu=0.182$, $\phi=2.5^\circ$) - - - - -	99
A-2	Comparison of Unconfined Compression Stress-Strain Characteristics for the Combined Variable Friction Angle and Strain Hardening Versus Perfectly-Plastic Drucker-Prager Models of SRI RMG 2C2. ($E=1.16 \times 10^6$, $\sigma_u=3200$ psi) - - - - -	100
A-3	Comparison of Uniaxial Strain Loading Applied Stress-Confinement Stress for the Combined Variable Friction Angle and Strain Hardening Versus Perfectly-Plastic Drucker-Prager Models of SRI RMG 2C2. ($\nu=0.182$, $\phi=2.5^\circ$) - - - - -	101
B-1	Mohr Circle Representation of Mohr-Coulomb Yield Surface - - - - -	104
B-2	Mohr-Coulomb Yield Function - - - - -	105
B-3	The Π -Plane in Stress Space - - - - -	107
B-4	Modified Mohr-Coulomb Yield Function - - - - -	110

LIST OF ILLUSTRATIONS (continued)

<u>Figure</u>		<u>Page</u>
B-5	SRI RMG 2C2 Closure Comparison between Drucker-Prager and Modified Mohr-Coulomb for Hydrostatic Loading with Both Roller and Stress Confinement- - - - -	113
B-6	SRI RMG 2C2 Closure Comparison between Drucker-Prager and Modified Mohr-Coulomb for Plane Strain Roller Boundary Conditions - - - -	114

SECTION 1 INTRODUCTION

1.1 REVIEW OF SRI SMALL-SCALE TEST FACILITY.

SRI International has developed [1-4]* laboratory-scale test facilities for the response of tunnel liners and other buried structures (as well as their internal components) under static or dynamic loading. A small-scale test apparatus provides a cost-effective way of screening structural concepts and conducting parametric studies of buried structural response. Figure 1.1 illustrates SRI's small-scale test apparatus, with independent application of vertical and lateral pressure under both static and dynamic load environments. The initial apparatus was designed [1] to test a 4-inch diameter cylinder with tunnel models of approximately 5/8-inch diameter, as shown in Figure 1.1. Later, a larger apparatus was developed [4] that could test 12-inch diameter cylinders with larger diameter tunnel models.

For static loading (see Figure 1.2), the pressures on the top surface, P_V , and on the sides of the test cylinder, P_H , are manually adjusted. For dynamic loading, explosives are used indirectly to generate the pressures P_H and P_V . The test cylinder "floats" on a lower reservoir of oil which applies (nominally) equal pressure P_V to the top and bottom surfaces.

The apparatus was originally designed to give loading rise times of the order of 50-100 μ sec. Such rapid loading, however, led to high frequency wave reverberation. Therefore, the apparatus was modified to produce relatively gradual dynamic loads, with rise times of about 5 msec. This is equivalent to a rise time of perhaps a full second on a real tunnel liner. Based on this modified rise time, the dynamic tests appear to be quasi-static in nature.

* Numbers in brackets designate references at the end of the report.

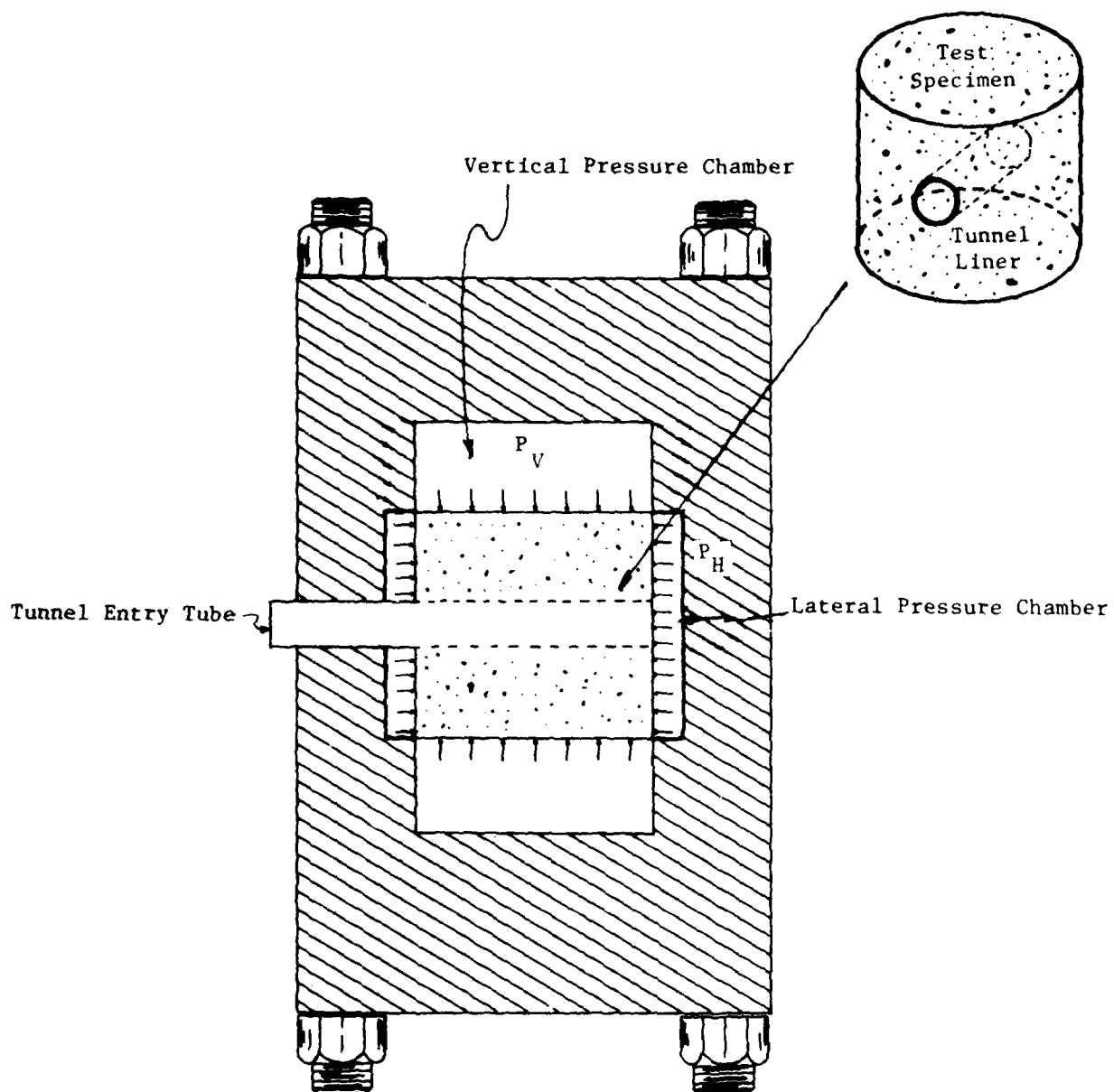


Figure 1.1. Schematic of SRI Triaxial Test Apparatus.

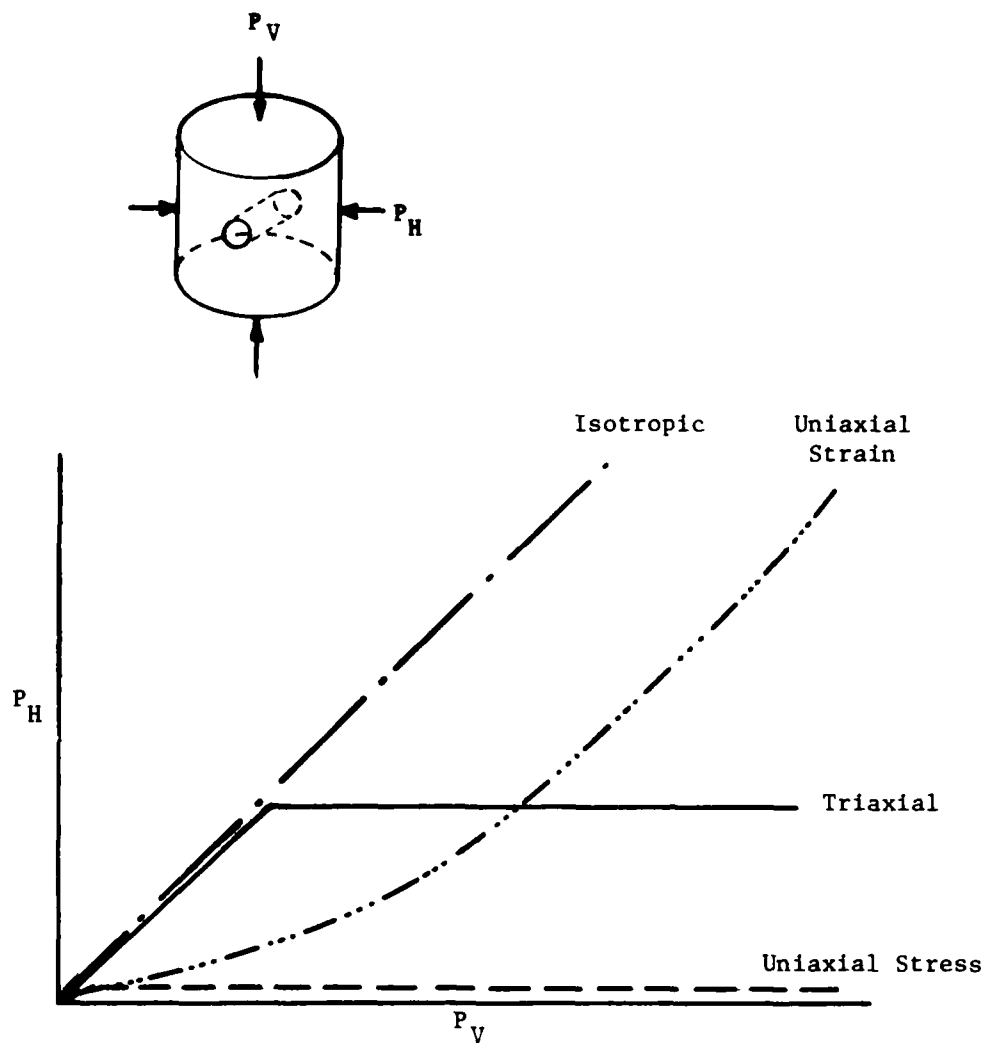


Figure 1.2. Various Loading Conditions Possible with the SRI Static Test Apparatus.

The data collected from a dynamic test consist of pre- and post-test measurements* of the crown-invert and springline diameters, time histories of the vertical and lateral pressures and time histories of hoop strain on the specimen's lateral surface. In a static test, the vertical and lateral pressures, hoop strain, crown-invert and springline diameters were recorded during each increment (~500 psi) of loading.

1.2 REVIEW OF SRI TEST PROCEDURE.

The primary objective of the SRI test fixture is to simulate a uniaxial strain condition as would be expected in-situ. It was assumed that ideal uniaxial strain of the *finite* specimen boundary was a reasonable approximation. In static tests, the test fixture approximates the ideal uniaxial strain lateral boundary using the following procedures:

- (1) A uniform vertical pressure is applied hydraulically to the cylindrical test specimen while the lateral pressure is held constant. Vertical load increments are applied in ~0.5 ksi steps.
- (2) For each vertical load increment a uniform lateral pressure is then applied hydraulically until the lateral boundary indicates zero lateral motion. Lateral motion is approximated by the hoop strain on the lateral boundary as measured by the average of two strain gauges diametrically opposed on the cylinder, at stations one tunnel diameter above the mid-height.

* In the larger test apparatus, additional stress and strain gauges could be placed at various locations in the specimen. Thus, a dynamic history of liner deformations could be made based on strain gauges placed in the tunnel.

Figure 1.3 illustrates the differences that can exist on the lateral boundary for an ideal uniaxial strain boundary and the SRI static test.

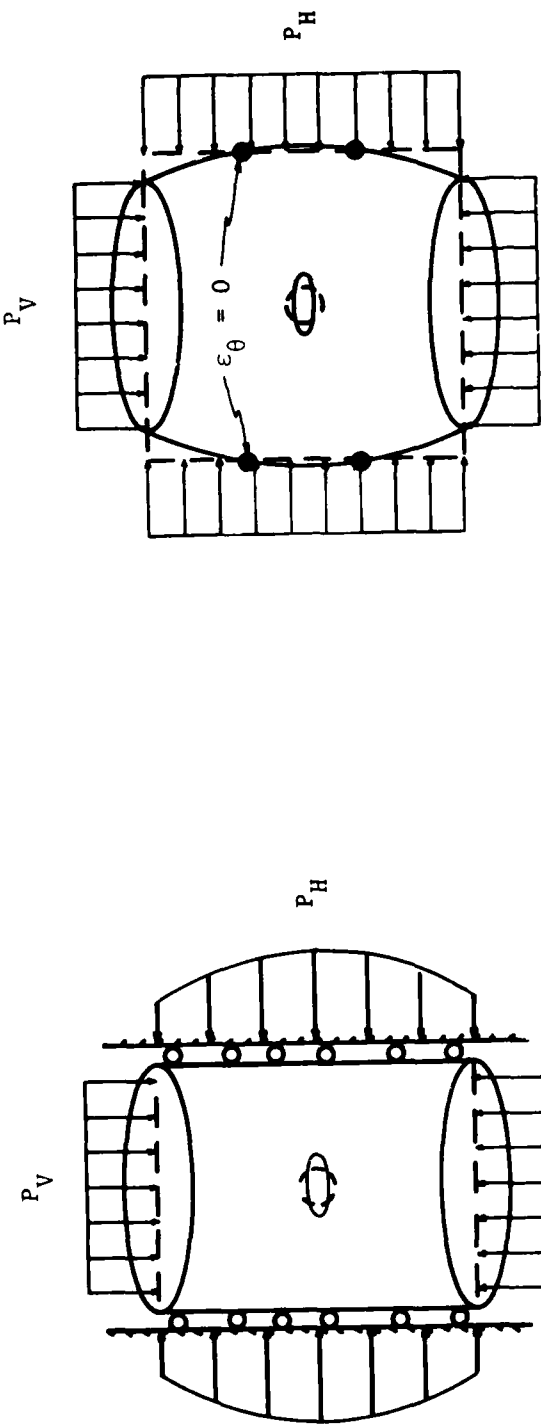
In the dynamic test, the vertical and lateral loadings are controlled separately but with a fixed ratio using low-density explosive charges. Unlike the static test, incremental lateral loads cannot be adjusted to maintain a zero hoop strain measurement on the lateral boundary. Instead, the uniaxial strain (non-linear) load path is approximated by an assumed linear loading path and the hoop strains are recorded. The magnitudes of these lateral strains indicate the degree of overconfinement or underconfinement of the specific test.

1.3 REVIEW OF SRI SMALL-SCALE EXPERIMENTS.

Using the small-scale test machine, SRI has performed [3,5] tests on scale models of MIGHTY EPIC/DIABLO HAWK structures in a tuff simulant, SRI RMG 2C2. Both dry and water-saturated models were tested under static and dynamic conditions.

These test specimens, made of the rock or tuff matching grout, provided a greater specimen homogeneity than found in normal geological test samples. The small-scale test cylinders were 4 inches in diameter and 4 inches high, with a tunnel bored through the cylinder along a diameter at a point halfway along its height. Each of the several tunnel liner models tested were inserted into the tunnel and grouted with a high strength gypsum cement.

For saturated tests in which porewater drainage was permitted, eight 1/32-inch holes were drilled in the tunnel liner near its ends to allow the seepage of porewater. In the tests where the saturated specimen had no porewater drain holes, a porewater pressure buildup gave anomalous tunnel deformations. Some of the static tests had drain holes only at



Ideal Uniaxial Strain Boundary

(Roller boundary gives non-uniform pressure on the lateral boundary to vary due to the presence of the tunnel)

SRI Simulation of Uniaxial Strain

(The application of uniform lateral pressure to maintain zero hoop strain at the station shown above, results in a departure from ideal uniaxial strain lateral boundary due to the presence of the tunnel)

Figure 1.3. Comparison of an Ideal Uniaxial Strain Condition with the SRI Simulated Uniaxial Strain Test.

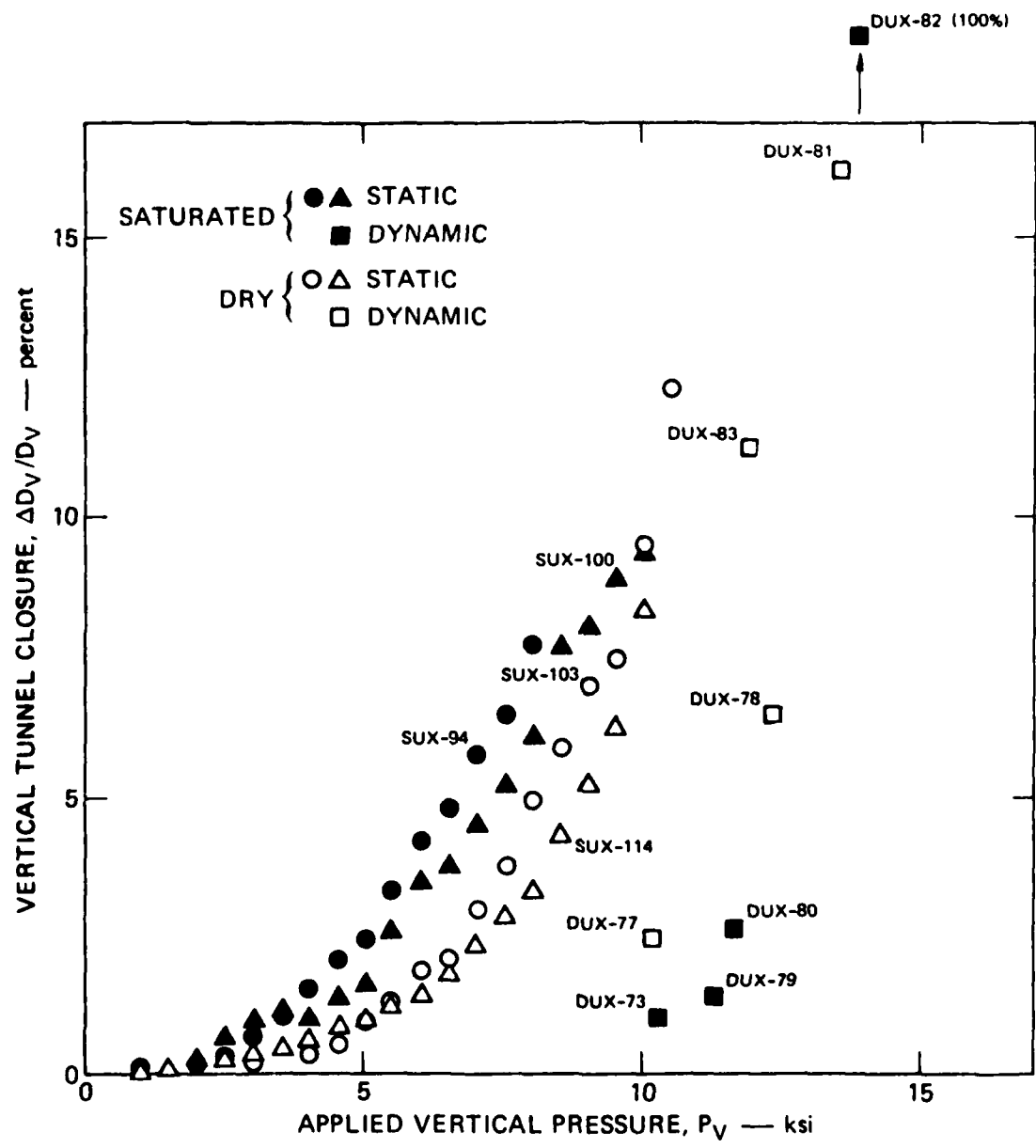
one end of the liner (creating a porewater pressure bulge at the undrained end) while others had drain holes at both ends. In dynamic cases, the drainage was not necessary since the time of porewater migration was much longer than the time frame of the test.

Closure data of SRI RMG 2C2 is shown in Figures 1.4 and 1.5. A basic trend appears in the data showing that the closures for the dynamic tests were considerably less than the corresponding static tests.

1.4 REVIEW OF SRI RMG 2C2 MATERIAL DATA

Since the rock matching grout, SRI RMG 2C2, was a special material, the existing constitutive properties were not readily available and had to be determined by material testing. Initially, it was assumed that tunnel response would not influence the uniaxial strain behavior of the SRI test specimens and that these tests could be used to determine material properties. Using the SRI static tests of *tunnelled* specimens, a lateral versus vertical pressure relation, Figure 1.6, was generated as if it were a solid test specimen under ideal uniaxial strain conditions. A bilinear fit based on an elastic-perfectly plastic material was then used to approximate the SRI data, as shown in Figure 1.6, to determine a working set of material constants. This technique is recognized as being approximate since the SRI lateral versus vertical pressure data could be influenced by the tunnel.

Standard material tests from WES and Terra Tek were also available. These tests (triaxial and unconfined compression and uniaxial strain) were conducted on solid cylinders of SRI RMG 2C2. Table 1.1 summarizes the interpretation of the available data, based on the assumption of elastic-perfectly plastic behavior. The differences between data from the three laboratories are not



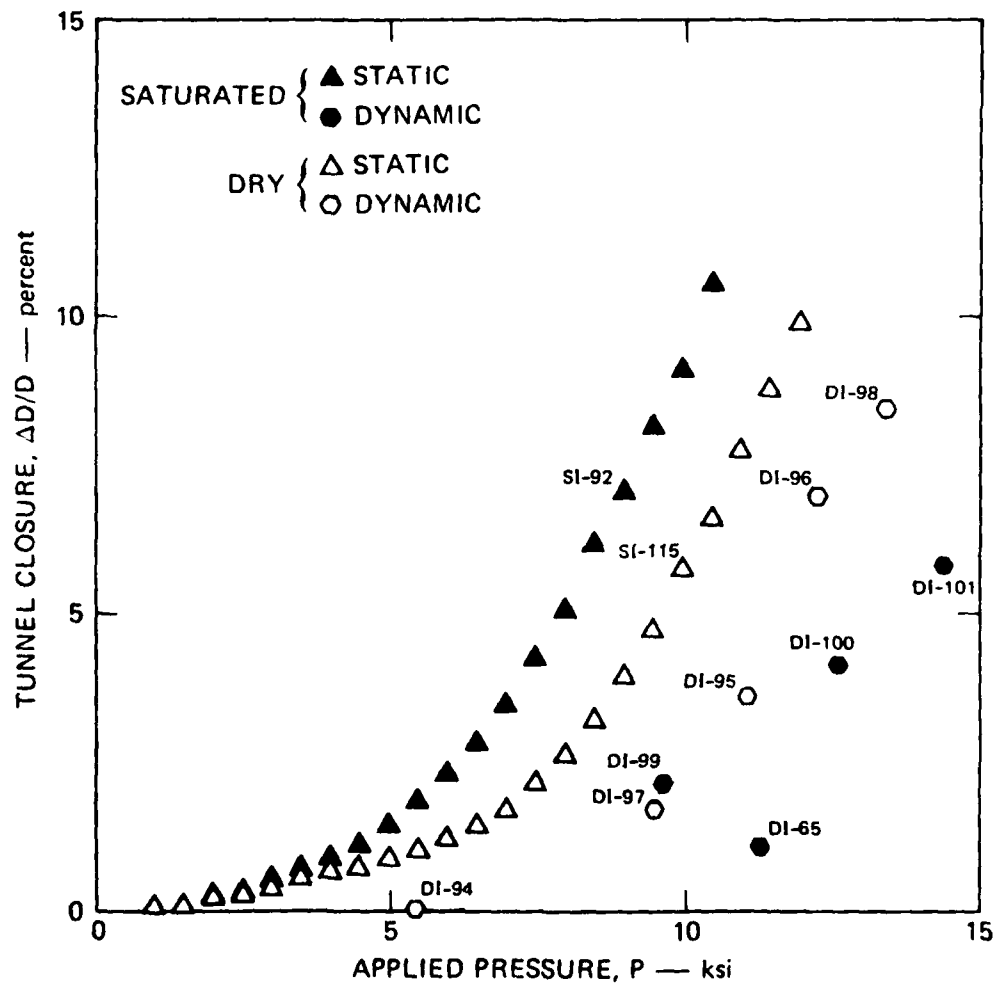


Figure 1.5. Tunnel Closure Versus Applied Pressure for Iso-tropic Loading of SRI RMG 2C2. Liner: 6061-T0 Aluminum, $a/h = 11.5$. From SRI [5].

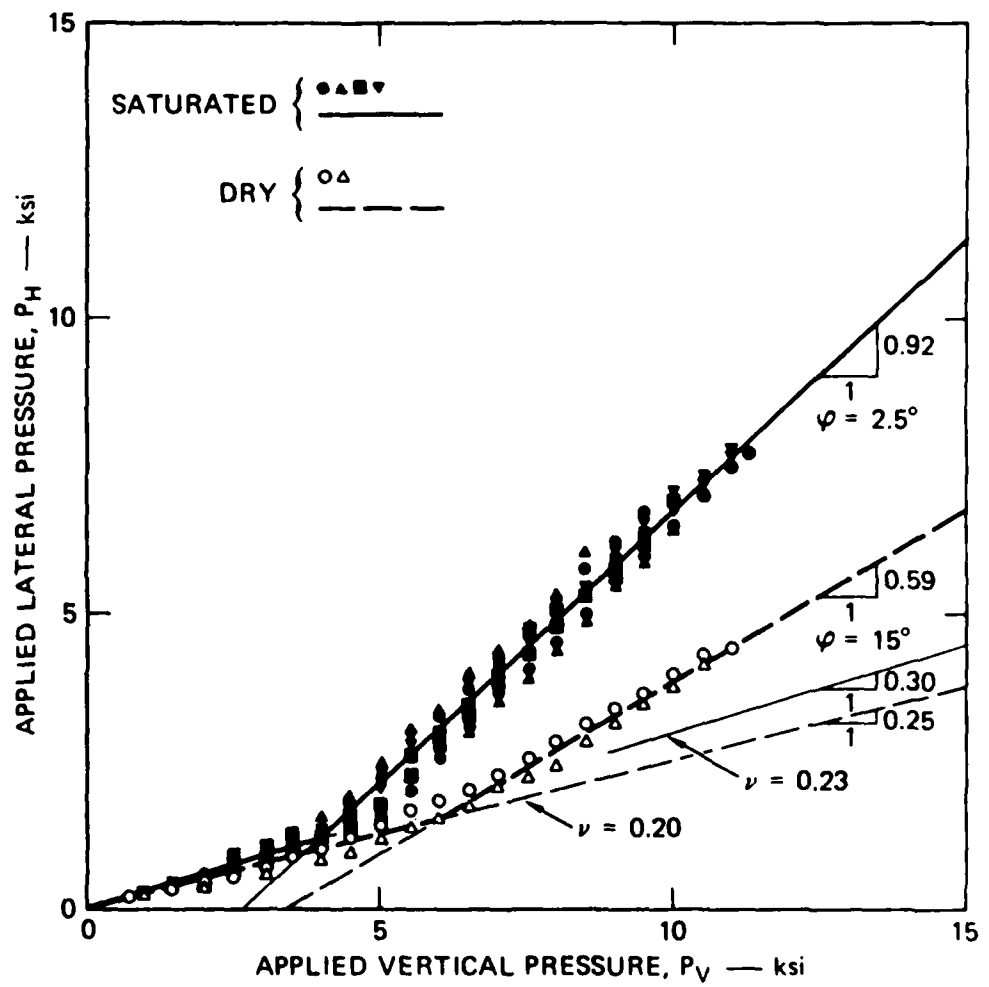


Figure 1.6. Lateral Confining Pressure Versus Vertical Pressure Needed to Maintain Uniaxial Strain Conditions in SRI RMG 2C2. From SRI [5].

Table 1.1. Available Material Parameters for SRI RMG 2C2.

Laboratory	WES	TERRA TEK	SRI
Specimen State	Saturated(?)	Saturated (?)	Saturated
Young's Modulus (10^6 psi)	1.82 ^a	1.16 ^a	1.15 ^a
Poisson's Ratio	0.23 ^a 0.21 ^b	0.18 ^a ----	---- * 0.23 ^b * 0.20 ^b
Unconfined Compressive Strength (psi)	3190 ^a 2740 ^b	3200 ^a ----	3675 ^a * 2695 ^b * 3640 ^b
Internal Friction Angle (degrees)	15 ^b (23-5) ^c	0.3 ^b (?) ^c	* 2.5 ^b ---- * 15.0 ^b ----

^a unconfined compression test

^b uniaxial strain test

^c triaxial failure envelope

* test specimen contains tunnel 1

generally large, except in the friction angle, which is much larger in the WES data. This observation, combined with the substantially greater compaction encountered in the WES data, suggests that the specimens tested by WES may have been less saturated than the samples tested at SRI and Terra Tek.

In summary, these tests show the likelihood of a moderate scatter and consequently an uncertainty as to what were the actual properties in the SRI RMG 2C2 when tested at SRI.

1.5 OBJECTIVES OF NUMERICAL INVESTIGATION

The preliminary SRI results indicated some sensitivity to strain rate in dynamic tests and to porewater pressure in static tests. A major reduction in tunnel closure (by factors of 10) was observed when dynamic tests results were compared to similar static tests. Also, porewater pressure buildup gave anomalous tunnel deformations in static tests of saturated specimens.

Clearly these observations have important implications with regard to both the SRI apparatus and the development of design data for buried structures. Also, lateral confinement conditions are important but rather difficult to control. (At the same time variations in confinement will likely occur in actual geologic conditions because of anisotropy, geologic variations, proximity of interfaces, etc.)

Changes in tunnel closure observed for dynamic laboratory tests versus similar static tests were thought to be due to differences in lateral confinement and to material property variations from strain-rate and porewater pressure effects.

These considerations were the motivation for the following objectives of the present investigation:

- (1) To understand and interpret the results of the small-scale SRI tests.
- (2) To evaluate the capability of the small-scale tests to simulate deep-based structural response.
- (3) To determine the areas of greatest sensitivity in the test, namely (a) the effect of lateral confinement; (b) the effect of material property variation and/or definition.

The analyses required to reach these objectives are detailed in the remainder of this report. The CRT version of the NONSAP finite element computer code [6,7] was used to perform the numerical calculations.

1.6 REPORT ORGANIZATION

The next two chapters give the numerical models used to perform the present analyses. Chapter 2 describes the mathematical material models for the rock simulant, and Chapter 3 gives the finite element model representations of the uniaxial strain loading experiments. Then, Chapter 4 presents the preliminary numerical analysis of the SRI experiments. The results on the ideal free-field simulation, the effect of material (including rate) behavior on tunnel response and the sensitivity of tunnel response to lateral confinement are given in Chapters 5, 6, and 7, respectively. Finally, Chapter 8 presents the numerical simulation of the static uniaxial strain loading experiments.

SECTION 2

MATHEMATICAL MODELS FOR ROCK SIMULANT, SRI RMG 2C2

2.1 BACKGROUND

In the initial (preliminary) phase of the numerical analyses, the rock simulant, SRI RMG 2C2, was idealized with an elastic perfectly-plastic material model using the Drucker-Prager yield criterion and its associated flow rule. The material parameters for the model were determined from P_V - P_H experimental data on tunnelled cylinder tests provided by SRI. The material constants (cohesion and friction angle) were evaluated assuming that the tunnel had an insignificant effect on the boundary response (i.e., P_V - P_H relationships for solid cylindrical specimens correspond to P_V - P_H relationships of tunnelled specimens). However, the preliminary calculations (Section 4) did not support the validity of this assumption. That is, based on the finite sample size used in the SRI tests, lateral boundary behavior is influenced by the presence of the tunnel. Thus, the material constituents used in the preliminary analysis did not necessarily reflect the characteristics of the test material.

For subsequent phases of the analyses (Sections 5 to 8), material constituents and the mathematical description thereof were evaluated from test data corresponding to experiments performed on solid cylinders. Triaxial compression and uniaxial strain test data provided by WES and Terra Tek was used to formulate material constituent models and to evaluate their material parameters.

2.2 DRUCKER-PRAGER MODEL

The Drucker-Prager model based on the Coulomb rule for slipping, has a conical yield surface in principal stress space. The yield function resembles von Mises in the π -plane but with a pressure term

added to account for the Coulomb effects [8]

$$F = \alpha J_1 + \sqrt{J_2^*} - k \quad (2.1)$$

where α and k are positive constants and J_1 and J_2^* are the first stress invariant and second deviatoric stress invariant, respectively. Drucker and Prager proposed [9] this model for limit design, so they considered rigid-plastic strain conditions, i.e., the only non-zero strains are plastic strains. For this case, they showed that this yield function fits the Mohr-Coulomb yield condition for the case of plastic plane strain, i.e., $e_{33}^P = e_{13}^P = e_{23}^P = 0$, if the α and k values were taken as:

$$\alpha = \frac{\sin\phi}{\sqrt{9 + 3\sin^2\phi}} \quad \text{and} \quad k = \frac{3c\cos\phi}{\sqrt{9 + 3\sin^2\phi}} \quad (2.2)$$

where ϕ and c are properties of friction angle and cohesion, respectively. If triaxial test results are used to find ϕ and c , then the plastic plane strain condition is no longer valid and a new Drucker-Prager condition is derived. This will be designated as a triaxial Drucker-Prager condition to clarify it from the original Drucker-Prager plane strain condition. Using triaxial test results, the α and k terms take the form:

$$\alpha = \frac{2\sin\phi}{\sqrt{3}(3-\sin\phi)} \quad \text{and} \quad k = \frac{6c\cos\phi}{\sqrt{3}(3-\sin\phi)} \quad (2.3)$$

In comparing several of these surfaces at their π -plane [8] intersections, see Figure 2.1, it should be noted that the triaxial Drucker-Prager circumscribes the Mohr-Coulomb surface, while the plane strain Drucker-Prager inscribes it. The plane strain Drucker-Prager

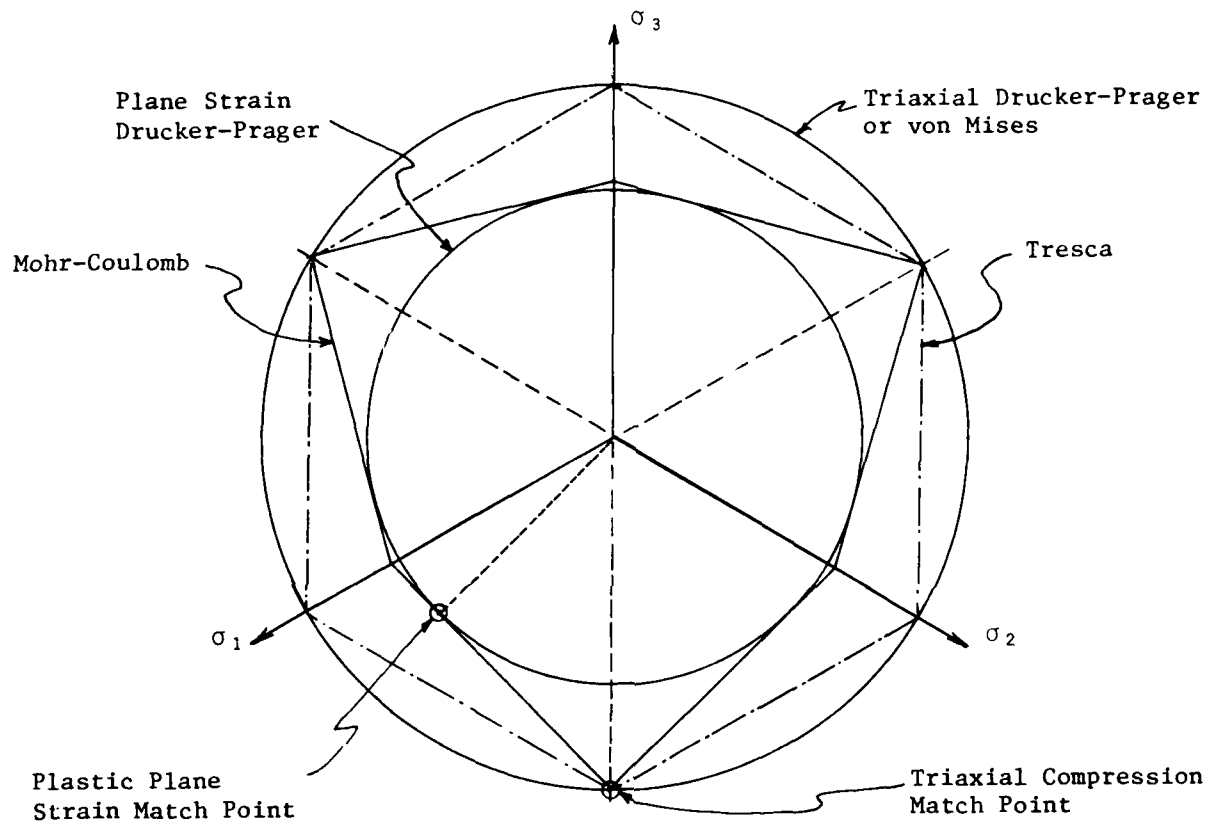


Figure 2.1. II-Plane Comparison of Various Yield Functions
 $(\sigma_1 + \sigma_2 + \sigma_3 = \text{Constant})$.

surface matches the Mohr-Coulomb surface at the rigid plastic plane strain points, while the triaxial Drucker-Prager model matches the Mohr-Coulomb at the triaxial compression locations.

Because of the nature of the SRI tests where some plastic flow occurs, and triaxial compression governs, the triaxial Drucker-Prager model was used. (The NONSAP Drucker-Prager has the triaxial formulation built into it, although, the plane strain formulation is easy to incorporate.)

The validity of the Drucker-Prager model was verified under uniaxial strain conditions by applying stress and roller boundary conditions. The NONSAP results were then compared against the analytical solution as shown in Figure 2.2.

This Drucker-Prager model representation of the SRI RMG 2C2 material was used in the preliminary numerical simulation of the SRI uniaxial strain experiments given in Section 4.

2.3 VARIABLE FRICTION ANGLE, STRAIN HARDENING DRUCKER-PRAGER MATERIAL MODEL

When typical experimental data for SRI RMG 2C2 is compared with the modeling capabilities of either a perfectly-plastic Drucker-Prager or Mohr-Coulomb model, the following deficiencies become apparent:

- (1) Figure 2.3 indicates typical experimental values of octahedral shear stress, $\sqrt{\frac{2}{3}J_2'}$, as a function of mean pressure for both initial yield and failure. This data was obtained from triaxial compression tests. Experimental data shows that both the initial yield and failure surfaces vary non-linearly with respect to mean pressure. Thus, Drucker-Prager or Mohr-Coulomb model at best can only fit the data for a small range of mean pressure.

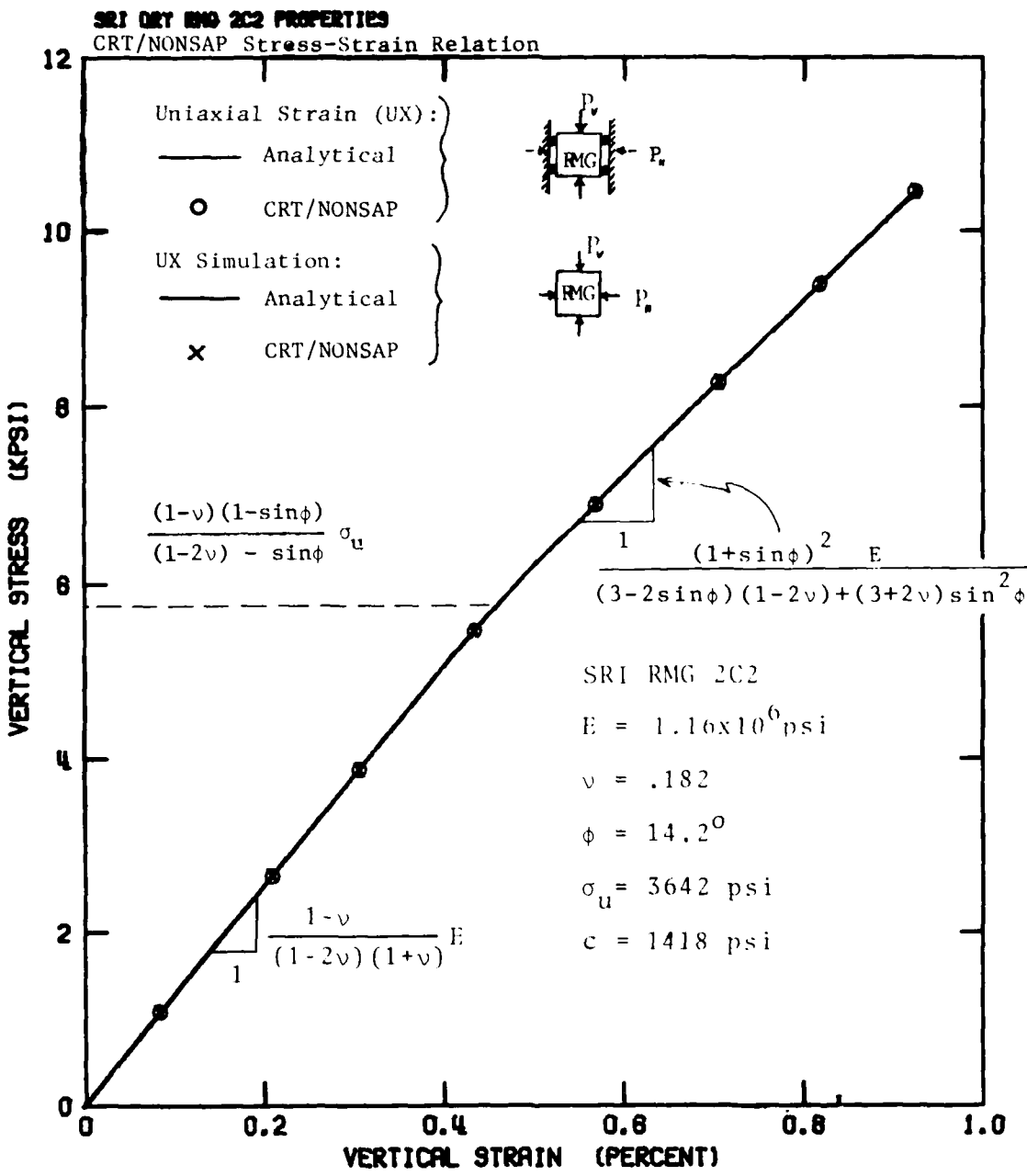


Figure 2.2. Preliminary Analysis Comparison of Analytical and Numerical Results for the Drucker-Prager Model.

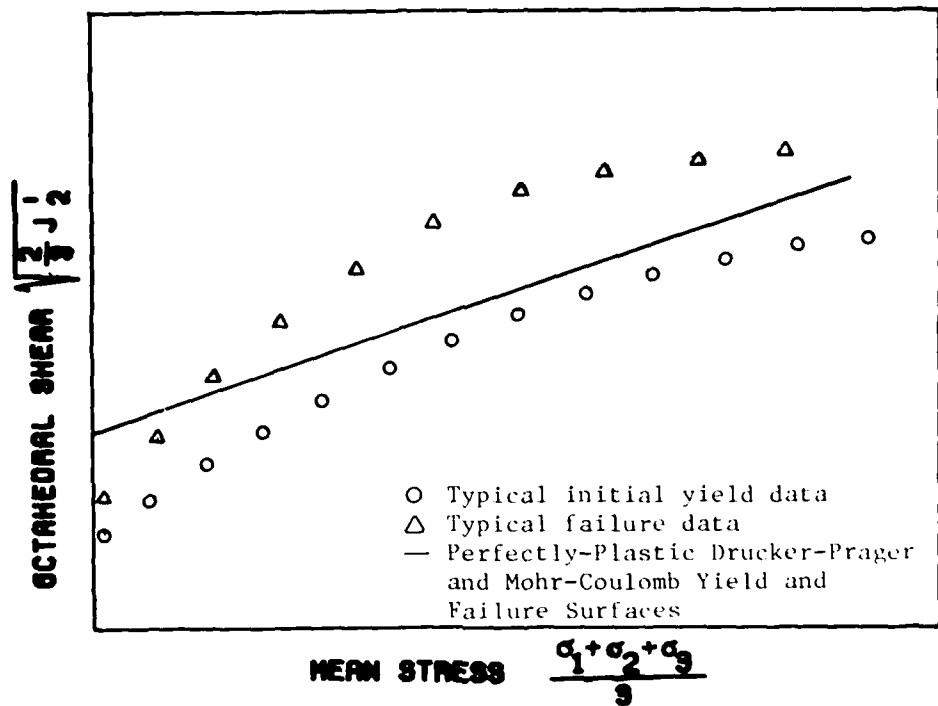


Figure 2.3. Comparison of Typical Experimental Failure and Yield Surface Data with a Perfectly-Plastic Drucker-Prager Model.

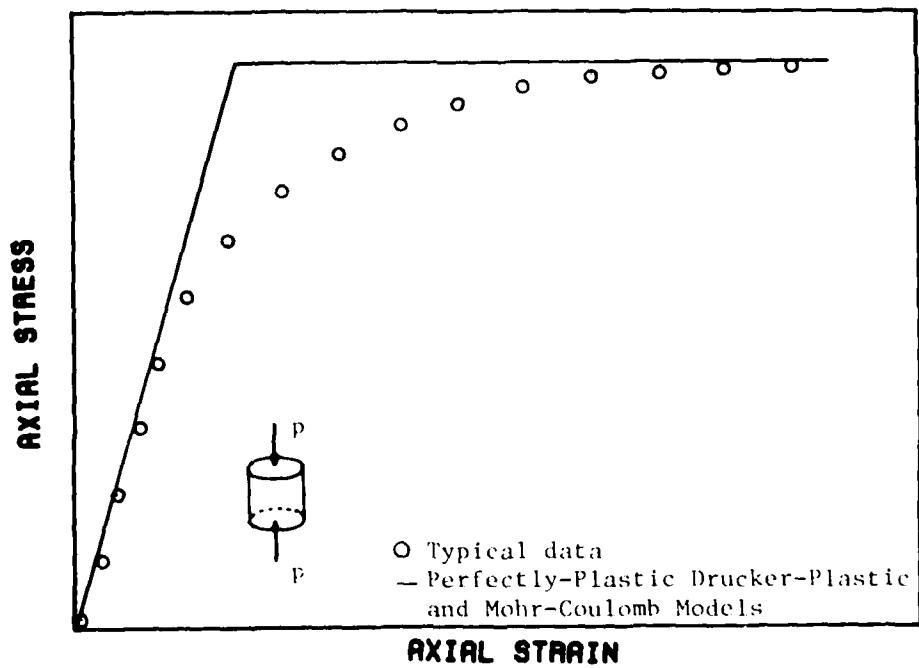


Figure 2.4. Comparison of Typical Unconfined Stress-Strain Data with Perfectly-Plastic Drucker-Prager and Mohr-Coulomb Models.

(2) A typical unconfined compression test for SRI RMG 2C2 is shown in Figure 2.4. After the onset of plastic flow, the data illustrates the strain-hardening characteristics of SRI RMG 2C2. Strain-hardening behavior of SRI RMG 2C2 is also indicated in the expansion from the virgin yield surface to the failure surface (See Figure 2.3). The disadvantage of a perfectly-plastic model is that it does not allow for yield surface to change either in size or shape.

(3) The applied stress-confinement stress ratios for a uniaxial strain test of SRI RMG 2C2 is shown in Figure 2.5. The test data indicates that after yielding, the applied-confinement pressure relation varies non-linearly. Perfectly-plastic Drucker-Prager and Mohr-Coulomb material models do not predict this non-linear behavior, in fact these models lead to bilinear applied-confinement stress relationships.

(4) The numerical simulation in the inelastic regime of a uniaxial strain test by the application of confinement pressure to an unconfined specimen is not possible using perfectly-plastic material models. When yielding occurs in a geometrically unconfined specimen (uniaxial simulation provided through the application of lateral confinement pressure), the resulting system stiffness is semi-definite, so that complete collapse results. Figure 2.6 shows the applied-confinement pressure that exists in a state of uniaxial strain assuming a perfectly-plastic material model. Any value of confinement stress that lies slightly to the right of the uniaxial strain results will produce collapse of a simulated uniaxial strain test. On the other hand, applied-confinement stress relations that

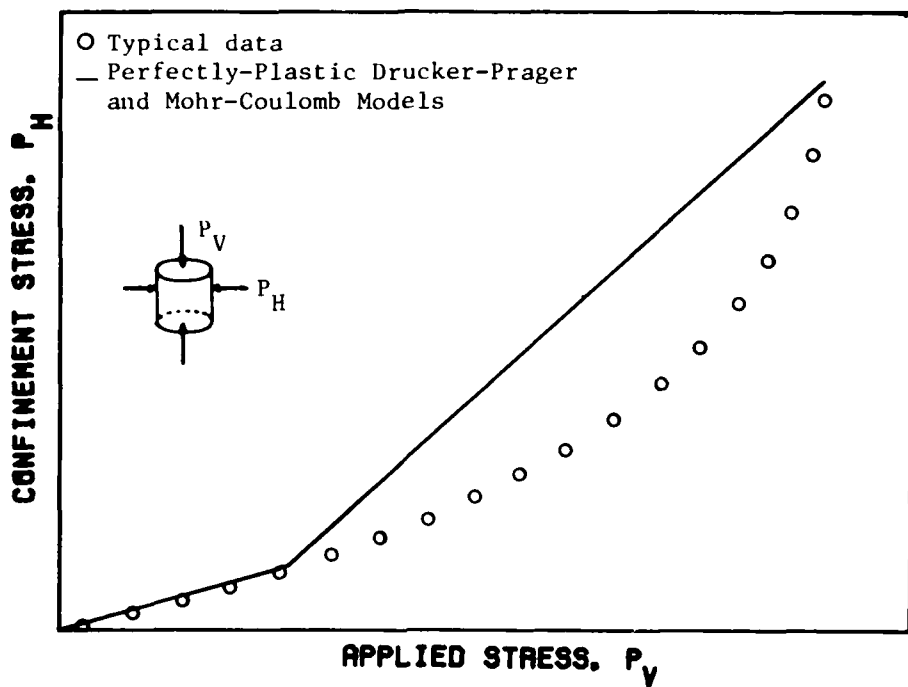


Figure 2.5. Comparison of Typical Uniaxial Strain Loading Applied Stress-Confinement Stress Data with Perfectly-Plastic Drucker-Prager and Mohr-Coulomb Models

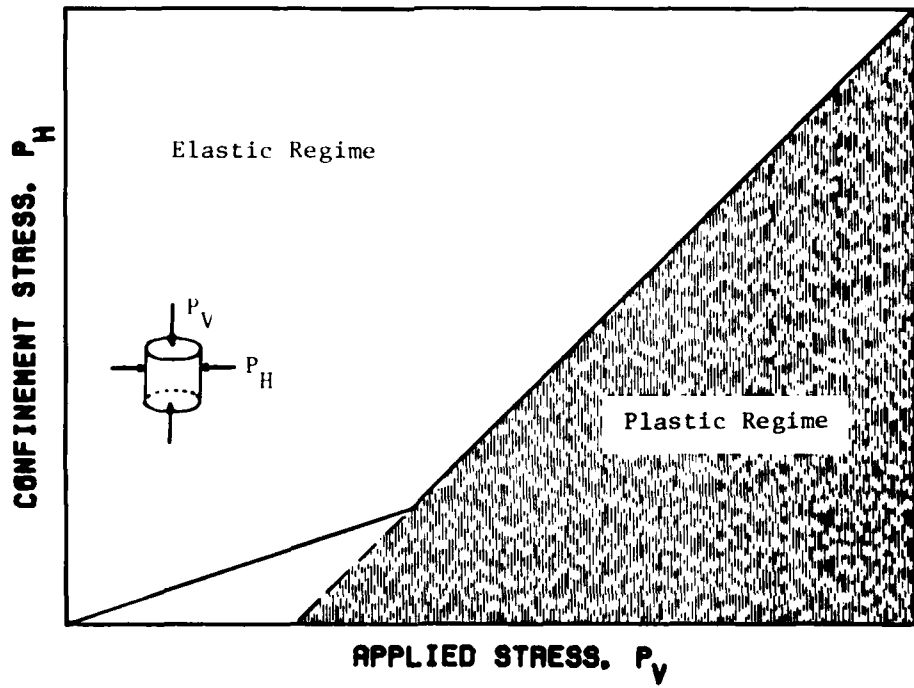


Figure 2.6. Uniaxial Strain, Applied Stress-Confinement Stress for Perfectly-Plastic Drucker-Prager and Mohr-Coulomb Material Models

lie to the left cause the geometrically unconfined specimen to behave elastically. This will cause the simulated uniaxial strain to deviate substantially from the uniaxial strain state. The nature of the SRI test implies that the SRI RMG 2C2 must strain-harden. Otherwise, the SRI static load controlled test for a perfectly-plastic or strain-softening material would result in collapse.

The above-mentioned inadequacies of a perfect-plastic Drucker-Prager or Mohr-Coulomb model for the idealization of SRI RMG 2C2 led to the development of an improved plastic material model with the following capabilities:

- (1) Both the yield surface and failure surface indicated by the experimental data can vary with increasing pressure in a non-linear manner.
- (2) The material model has work dependent variable isotropic hardening which gives improved simulation of experimental data and permits the numerical modeling of a geometrically unconfined simulated uniaxial test.

The details involved with NONSAP implementation of the variable Drucker-Prager model and a comparison of its fit with experimental data is given in Appendix A. This model is used in Sections 5 to 8.

2.4 MODIFIED MOHR-COULOMB MATERIAL MODEL

SRI has also performed theoretical NONSAP analyses to help in their evaluation and interpretation of the experimental results. Their representation of the material constitutive behavior of the rock medium, SRI RMG 2C2, consisted of an elastic-perfectly plastic material model using the Mohr-Coulomb yield criterion with an associated plastic flow rule. The Mohr-Coulomb material subroutine (10) was added to the NONSAP code by SRI for the specific purpose of performing these calculations. SRI completed theoretical calcula-

tions for *isotropic* loading, which compared reasonably well with static experimental results. However, SRI had difficulties when they attempted to apply NONSAP, specifically their Mohr-Coulomb material model, to numerically simulate their *uniaxial strain* tests.

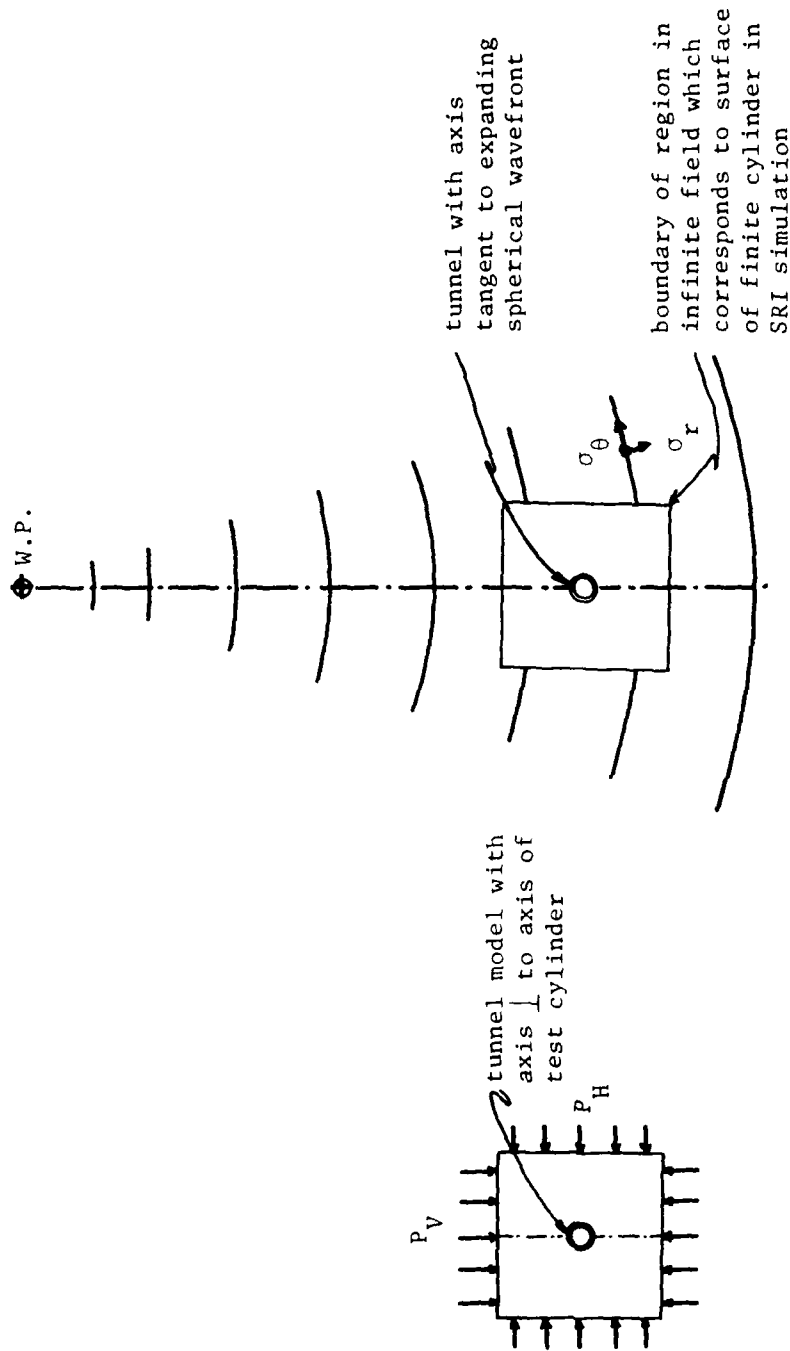
The Mohr-Coulomb material model was modified in the current program to alleviate the difficulties encountered by SRI. In this modification, the corners of the traditional Mohr-Coulomb yield criterion were rounded, so that the yield criterion has continuous normal derivatives, and hence unique plastic-flow conditions for all states of stress (see Ref. [8]). The problem encountered by SRI was a consequence of non-unique plastic flow that occurred in the corners of the conventional Mohr-Coulomb yield surface. To see this effect, consider the state of stress under uniaxial strain conditions ($\sigma_1 = P_V$, $\sigma_2 = \sigma_3 = P_H$). When the initial yielding occurs, the stress state lies at a corner of the traditional Mohr-Coulomb surface. Thus, any round-off error introduced by a computer will produce any arbitrary value for the gradient, introducing asymmetry and numerical instability in the problem. The modified Mohr-Coulomb criterion eliminates this problem by the rounding of the corners. The details of this model are described in Appendix B.

SECTION 3

FINITE ELEMENT MODELS OF UNIAXIAL STRAIN LOADING EXPERIMENTS

The intent of the SRI uniaxial strain loading test is to represent the response of buried structures using small-scale finite specimens. The validity of the SRI test is in a sense dependent on the assumption that the finite boundary (approximately 6 tunnel diameters) behavior in the free-field is essentially equivalent to the boundary behavior of the test specimen (see Figure 3.1). The SRI test was conducted under the assumption that for practical purposes a uniaxial strain condition at the finite boundary is equivalent to the free-field condition (which implies that the tunnel response does not influence the behavior on the finite boundary). Hence, uniform lateral stress is applied and a uniaxial strain condition is prescribed (actually hoop strain) at a point along the boundary (see Figure 1.3).

In the initial (preliminary) phase of the analysis, numerical studies were performed (see Section 4) with a plane strain finite element representation of the SRI test. The steps employed in this analysis are described as follows. First, the results of the SRI simulated uniaxial strain tests (applied pressure-confinement pressures, P_V - P_H) were used to evaluate the material parameters for a perfectly-plastic Drucker-Prager model as discussed in Section 2.2. (The validity of this assumption requires the tunnel to have an insignificant effect on the response at the boundary of SRI test specimen. That is, the P_V - P_H relation for a uniaxial strain test of a solid specimen would be essentially equivalent to that with a tunnel.) Then, having established the material properties, the plane strain numerical simulation of the SRI test was performed by applying the experimental P_V - P_H pressure relation as stress boundary conditions. (With this stress condition no lateral strain reference location was used.)



SRI Simulation
(cylindrical test sample loaded by uniform pressure on ends and side so as to maintain $\epsilon_\theta \approx 0$ at a particular station on side.)

Idealized Free Field Condition
(contained burst in homogeneous, isotropic field)

- * Are these essentially equivalent?
- * If not, can simulation be improved?

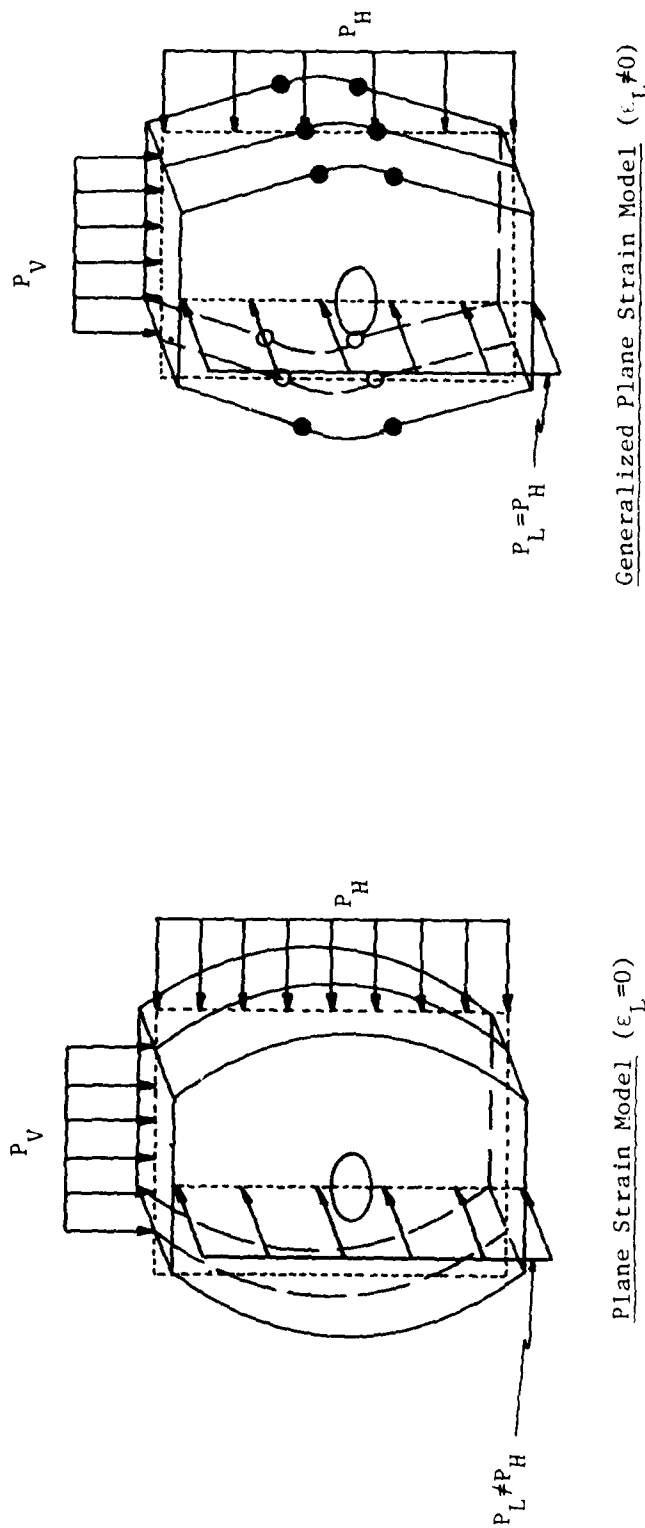
Figure 3.1. Comparison of the SRI Simulated Uniaxial Strain Test with Free-Field Condition.

Figure 3.2 illustrates the plane strain modeling capabilities and limitations with regard to the SRI test. The plane strain simulation can be visualized as a rectangular slab with a lateral hole through the center, with uniform stresses applied to the top and lateral surfaces. Because of plane strain assumption, the resultant force in the plane strain direction may not be equal to the resultant lateral force. This is not necessarily consistent with the SRI test where both are essentially equal. This inconsistency can be resolved by removing the plane strain constraint (i.e., $\epsilon_L \neq 0$), as shown in Figure 3.2

Also, the sensitivity of the preliminary analysis to lateral confinement led to the development of an alternate procedure for applying the lateral constraint. The procedure used in the numerical approach was identical* to the experimental procedure. That is, lateral pressures were adjusted until zero lateral displacement was obtained at a point on the lateral boundary corresponding to the location of the SRI reference strain gauges.

Thus, in the subsequent phase of the analysis, numerical simulations of the SRI tests were performed using a *generalized* plane strain finite element model with material parameters evaluated independently of the SRI test data. The analysis incorporates two basic improvements over the preliminary analysis: (a) the zero lateral strain location on the lateral boundary matches the experimental location and (b) the plane strain constraint is relaxed, i.e., $\epsilon_L \neq 0$, which allows the out-of-plane force to be specified (in this case, equal to the resultant lateral force).

*The two hoop strain gauges located on the lateral boundary of the SRI test specimen were intended to provide a measure of the lateral displacement. However, due to asymmetry, one gauge gave a positive strain while the other gave a negative strain for an average strain of zero. This constraint does not necessarily imply that the lateral displacement at this location is zero.



Plane Strain Model ($\epsilon_L = 0$)

(Uniform vertical and lateral pressures applied based on SRI's P_V - P_H data. Plane strain assumption can cause resultant out-of-plane pressure to differ from lateral pressure.)

Generalized Plane Strain Model ($\epsilon_L \neq 0$)

(Uniform vertical and lateral pressures applied to maintain zero lateral strain at same location as the SRI test. Generalized plane strain formulation allows for equal resultant out-of-plane and lateral pressures).

Figure 3.2. Comparison of the Plane Strain and the Generalized Plane Strain Models Used to Simulate the SRI Uniaxial Strain Experiments.

SECTION 4

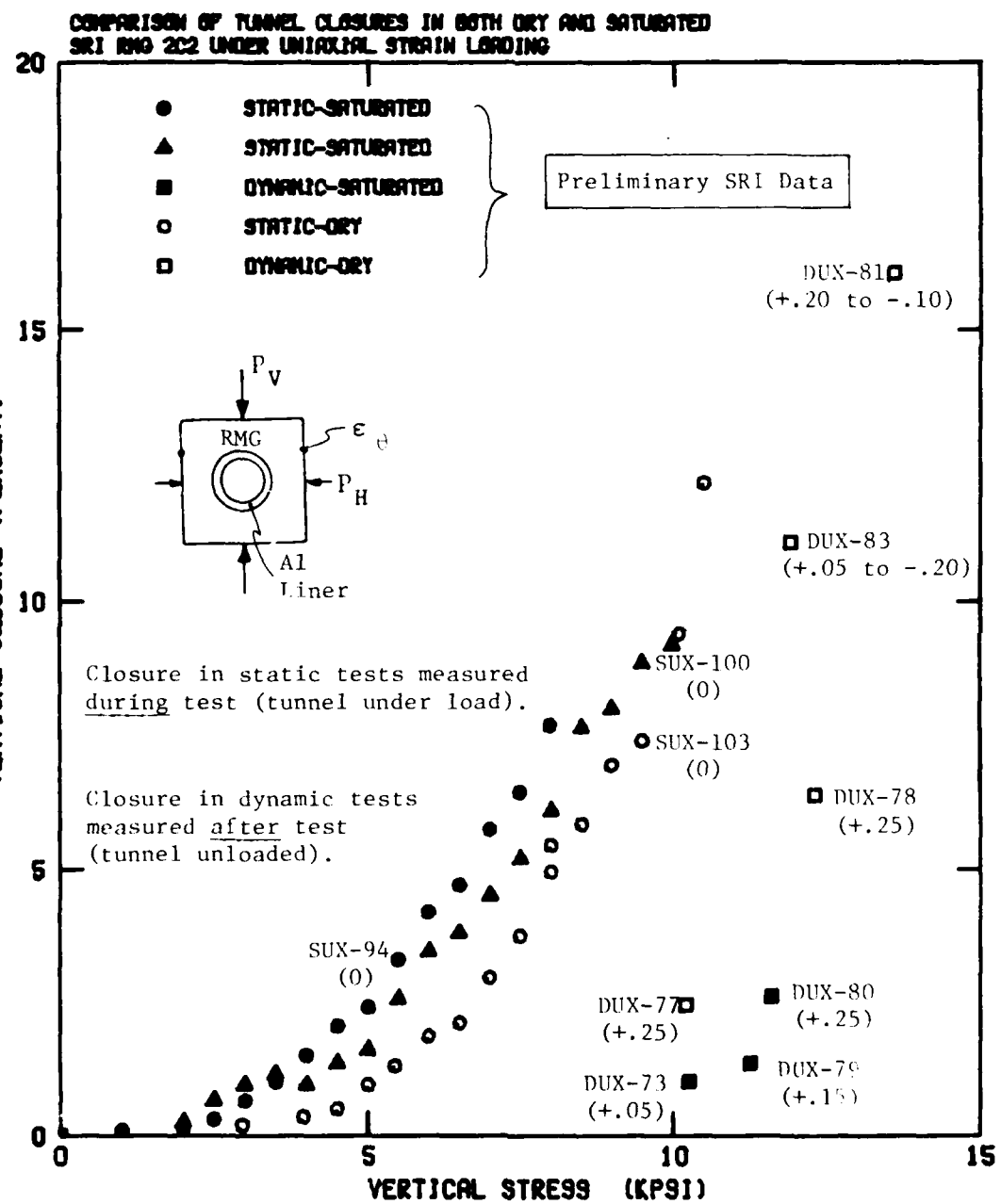
PRELIMINARY NUMERICAL ANALYSIS OF SRI EXPERIMENTS

Under the first phase of the program, preliminary analyses were made in order to develop a numerical model of the SRI test and to find the sensitive factors governing test data, Figure 4.1.

The preliminary model used a plane strain finite element representation of the SRI test specimen (see Section 3). At the lateral boundaries either a roller boundary condition could be applied (an ideal uniaxial strain situation in a solid specimen) or a uniform pressure could be applied based on the SRI test (see Figure 4.2). The material model used was the Drucker-Prager model described in Section 2.2 and shown in Figure 4.2.

Analyses were performed with the ideal uniaxial strain (roller) conditions on the lateral boundary and compared with a uniform stress boundary condition, as shown in Figure 4.3. Although a roller boundary condition gives a state of uniaxial strain on the sample, the presence of a tunnel alters the lateral pressure condition. Figure 4.4 shows the results of the analyses performed to evaluate the effects that tunnel size has on closure.

Several sets of material properties representing both dry and water saturated SRI RMG 2C2 were simulated. The material data were obtained from P_V - P_H curves from SRI's static tests. Because the SRI dynamic tests were essentially quasi-static, the tests were initially analyzed by duplicating the load paths in a static solution. The load paths were taken from the SRI dynamic test data and applied to the plane strain grid, so that the amount of stress confinement occurring in the SRI dynamic test is duplicated. In addition, a straight line approximation to the load path was used as a check on path dependence. These results are shown in Figure 4.5. Since the dynamic test was more overconfined than the static



Quantity in parenthesis refers to nominal maximum percent hoop strain, ϵ_θ , measured on test cylinders (near station indicated by sketch) during test. Positive values indicate compressive strains (overconfinement).

Figure 4.1. SRI Vertical Closure Data for Static and Dynamic Uniaxial Strain Loading of SRI RMG 2C2.

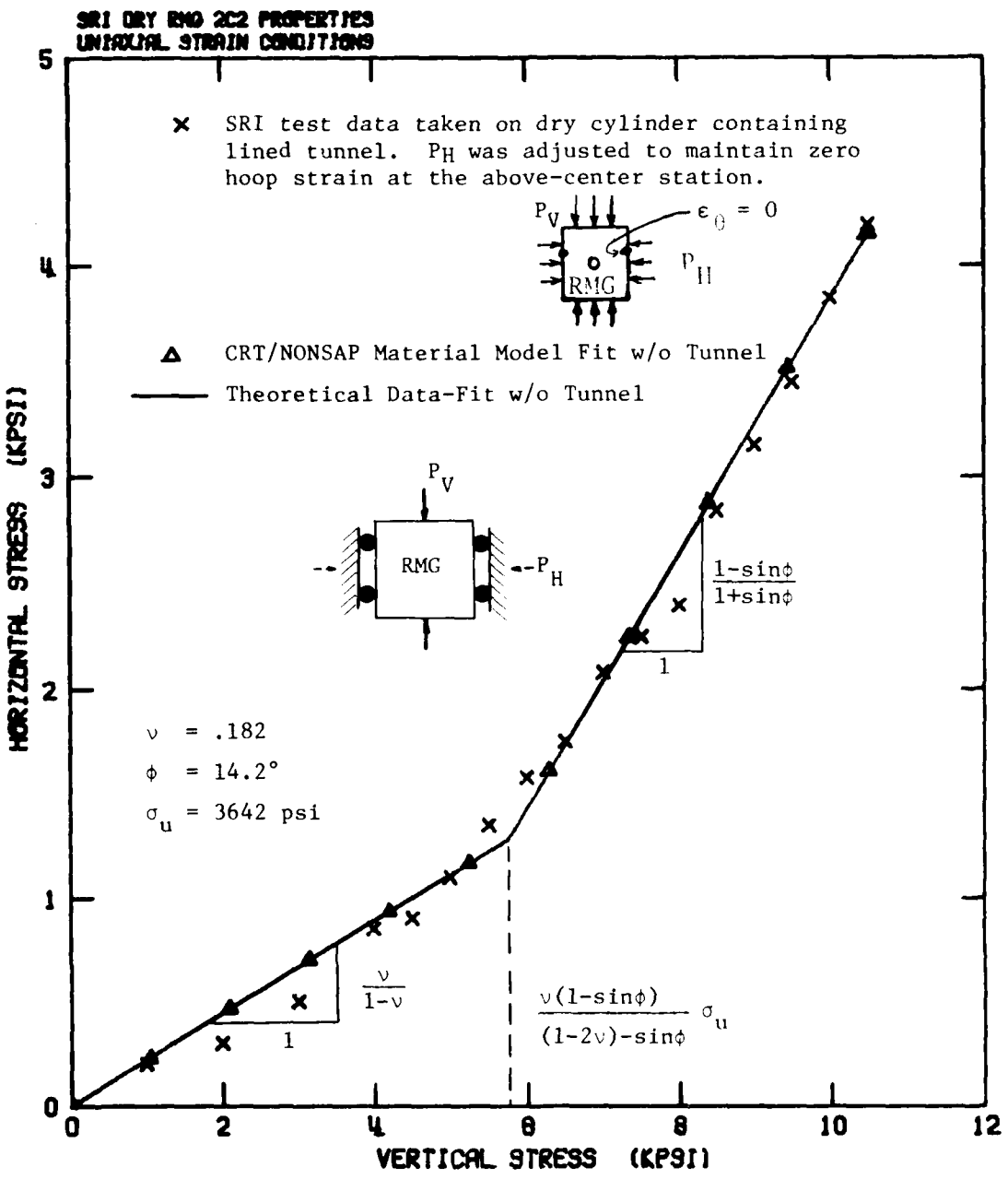


Figure 4.2. CRT/NONSAP Material Model Fit to SRI Test Data on Dry Sample (SUX-103).

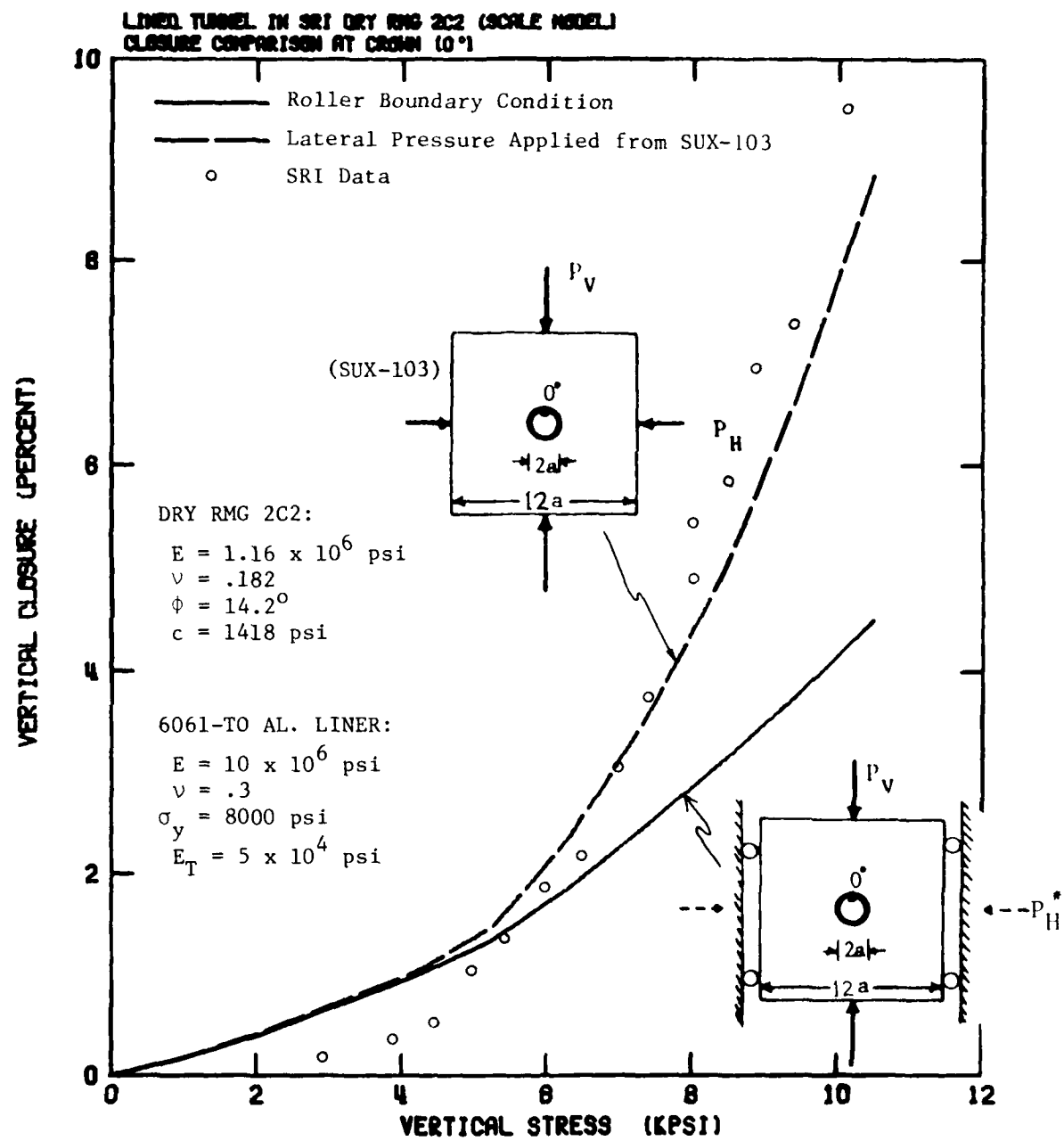


Figure 4.3. Numerical Simulation of Static Test SUX-103, using Roller and Pressure Boundary Conditions.

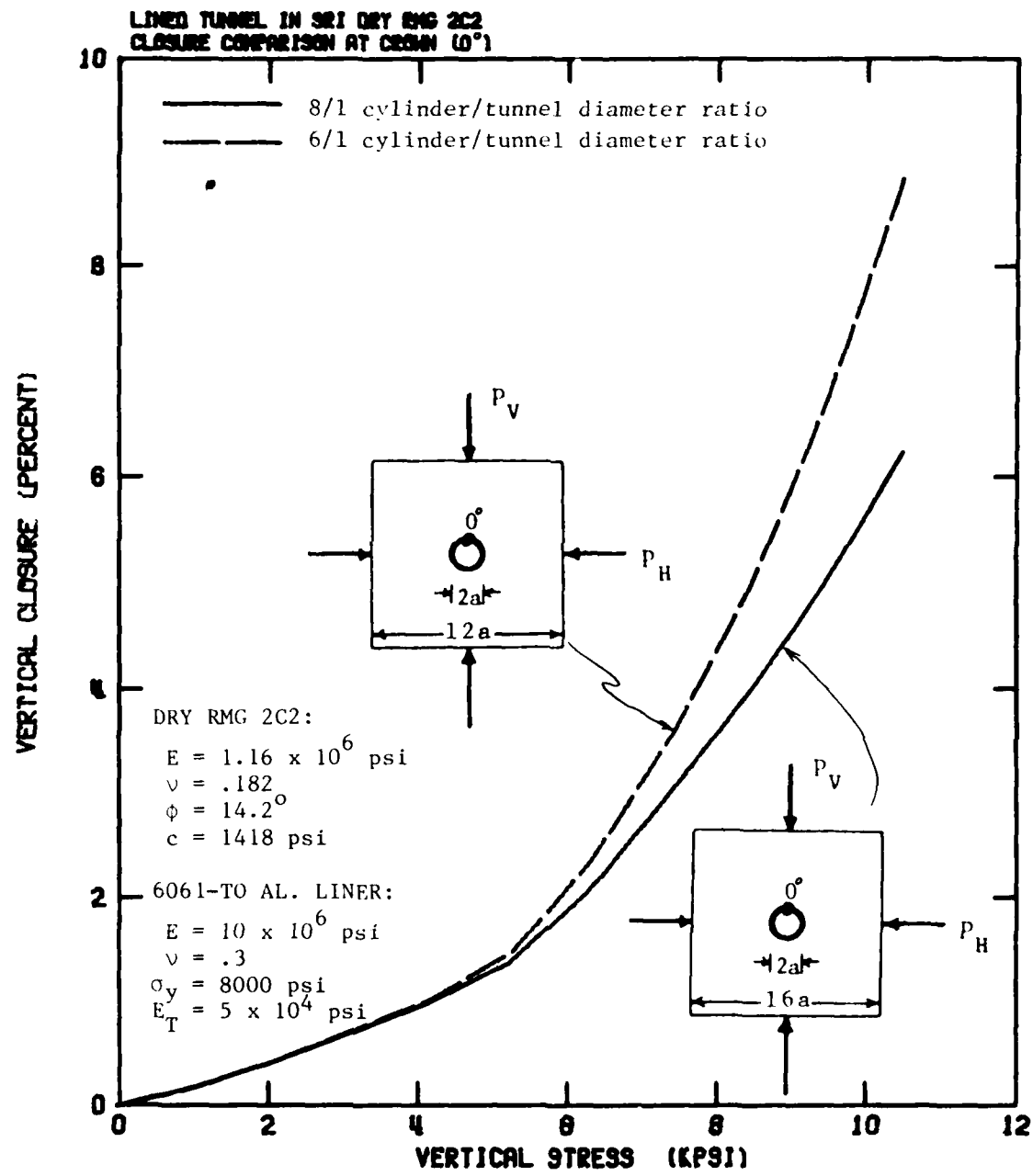


Figure 4.4. Numerical Analysis of Crown Closure Comparison between Dry SRI RMG 2C2 having Cylinder to Tunnel Diameter Ratios of 8/1 and 6/1.

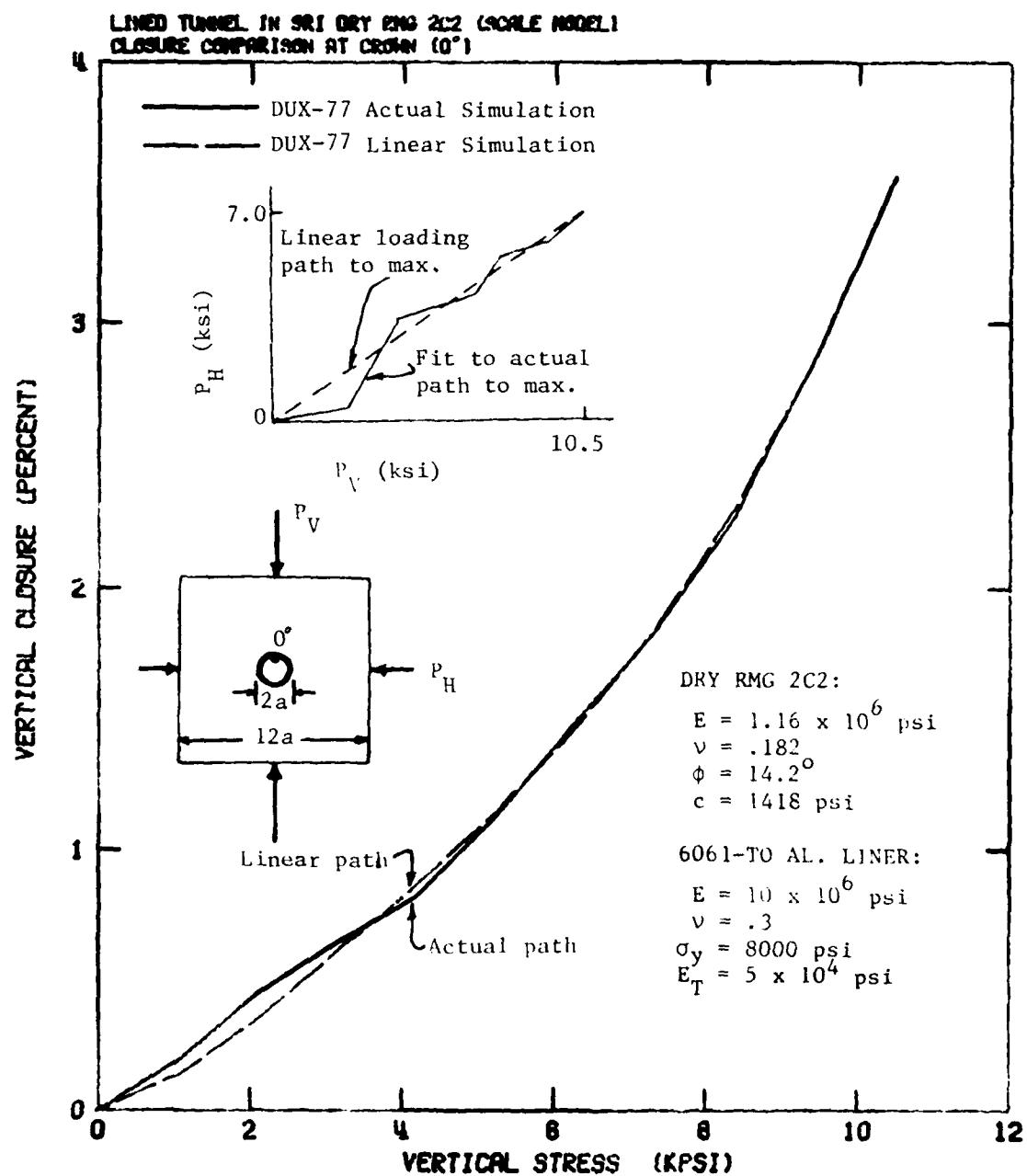


Figure 4.5. Numerical Simulation of Dynamic Test DUX-77, using Simple Linear Loading Path and Actual Fit to Measured Path.

test, as shown in Figure 4.6, the results should be essentially path independent, as indicated in Section 7.

The preliminary analysis exposed several trends in the SRI test apparatus (see Figure 4.7). These initial conclusions were then examined more carefully in the second phase of the program.

The first conclusion reached was that measurement of non-linear material properties and of pressure ratios required to maintain uniaxial strain by using test cylinders containing tunnels gives misleading information. Thus, tunnelled specimens should not be used to simultaneously define material properties and analyze the SRI test. Clearly, solid test specimens should have been used in the SRI test apparatus to first define the material behavior. As a consequence it appears that the ratio of test cylinder diameter to tunnel diameter effects the closure, especially after the onset of material plasticity.

Static tests should be emphasized, at least for now. They are much less expensive, yield more complete data, are more reliable, and are inherently easier to specify and control. As such, static tests are a good way to ferret out such things as the possible sensitivity to lateral confinement.

Dynamic loading has been harder to control, and most of the dynamic tests have been overconfined (as compared to the nominally uniaxial strain loading in the static tests).

Figure 4.7 summarizes the most important results of the preliminary analyses. Using the available material property data, the plane strain finite element analyses essentially duplicated the tunnel closure versus applied stress observed by SRI in static uniaxial strain test SUX-103. Then, using the same properties but loading the tunnel along the moderately *overconfined* stress path which occurred in SRI dynamic test DUX-77, the observed

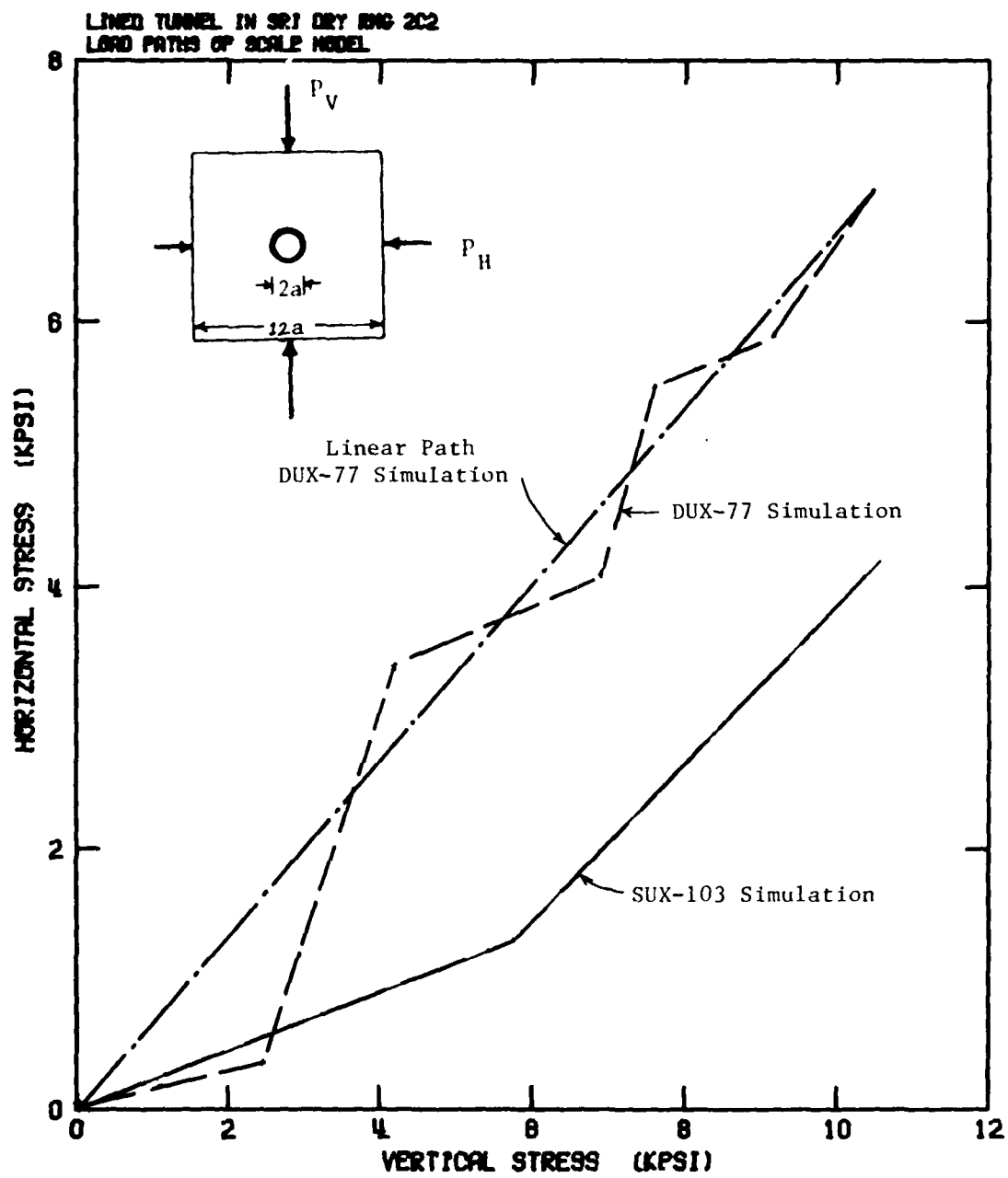


Figure 4.6. Loading Paths for Numerical Simulations of SRI Static and Dynamic Tests.

LINED TUNNEL IN SRI DRY RMG 2C2 (SCALE MODEL)
COMPARISON OF CLOSURE

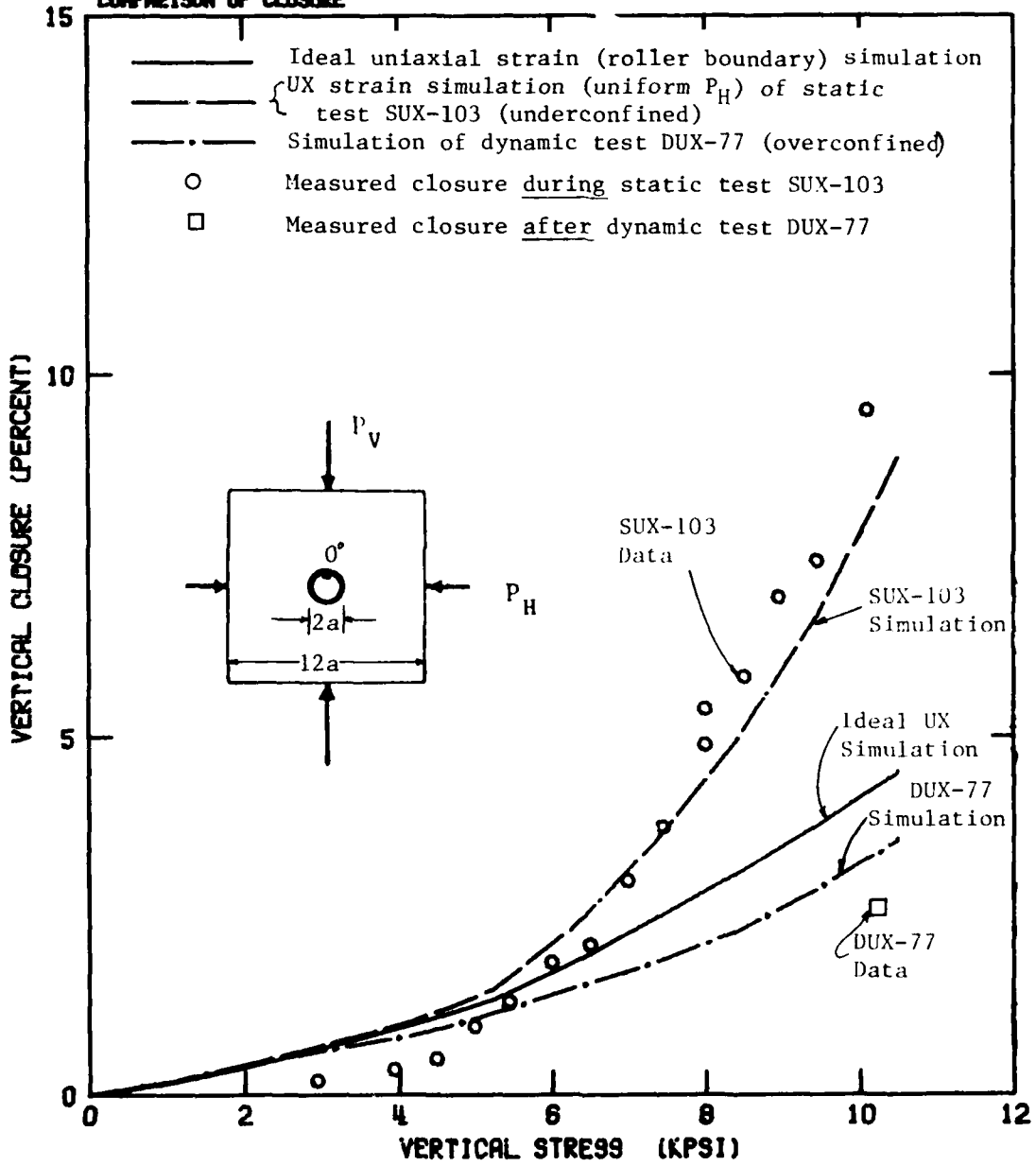


Figure 4.7. Preliminary Analysis Comparison of Experimental and Theoretical Crown Closure in SRI RMG 2C2.

closure in that test was also essentially duplicated by numerical analyses. In both cases, the results may have been fortuitous, so additional analyses are clearly desirable before firm conclusions are drawn. However, these results are self-consistent, and they do suggest that the differences in lateral confinement could be responsible for the differences in the static-dynamic results. As a corollary, the results suggest that tunnel response may be sensitive to the degree of lateral confinement. This could be important to buried structure design criteria.

SECTION 5

IDEAL FREE-FIELD SIMULATION

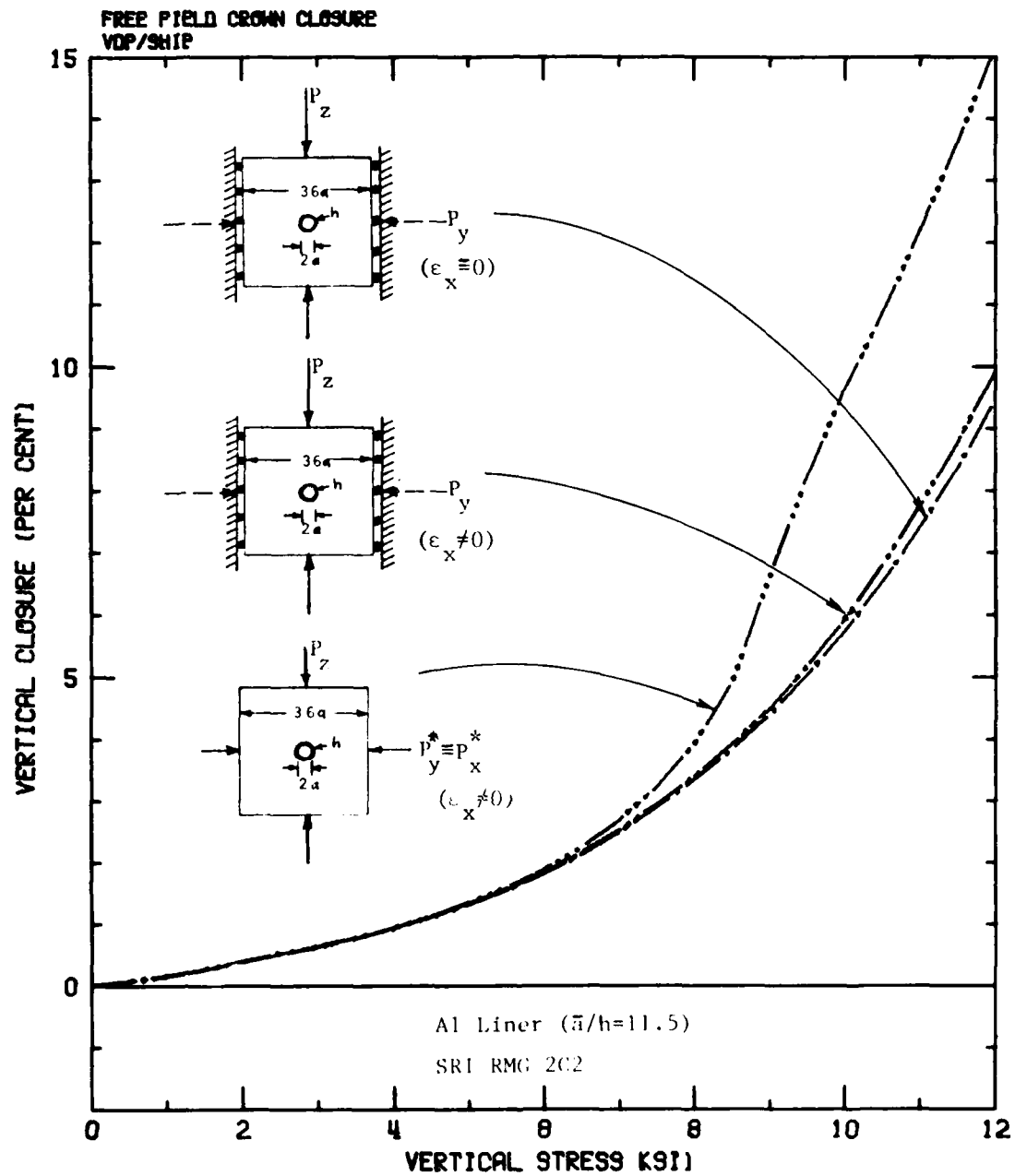
Perhaps the most significant question in regard to the SRI test apparatus is its capabilities to simulate the response of actual deep-based tunnels. To evaluate and interpret the effectiveness of the SRI experiment, numerical calculations were performed to isolate and identify discrepancies that could occur between ideal free-field tests and SRI tests performed on finite samples. Thus, several analyses were performed using grids where the boundaries were far removed from the tunnel (ratio of tunnel diameter to cylinder diameter of 18) and the improved material model given in Appendix A.

In the SRI uniaxial strain test, uniform stress is applied to the lateral boundary at $\sim 6a$ so that nearly zero strain occurs (2a above the mid-height). Using the results of the far-field boundary analysis, the stress and strain distribution along the $6a$ lateral boundary can be compared with the SRI test.

A comparison of the lateral boundary conditions for the SRI test with free-field conditions is a key consideration, since these boundary conditions have a very strong influence on the specimen response. Nevertheless, the fundamental question is how do the tunnel *closures* for the SRI test compare with free-field? Is the SRI test overconfined (non-conservative) or underconfined (conservative)?

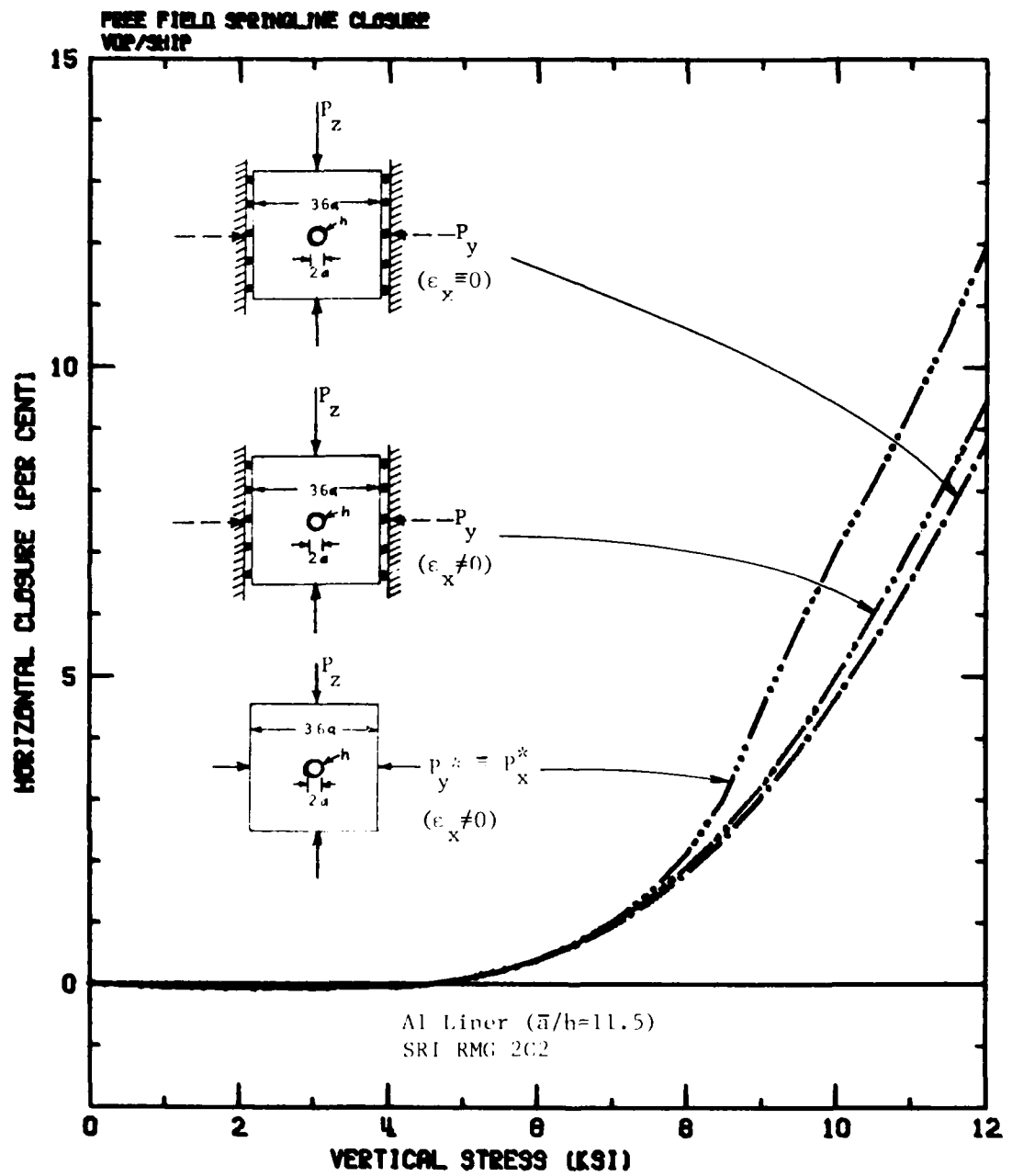
The numerical results obtained for tunnel crown and springline closures for the simulated free-field condition are shown in Figures 5.1 and 5.2, respectively. Three different assumptions regarding the nature of the lateral boundary conditions in the far-field (ratio of tunnel diameter to cylinder diameter of 18) were used:

- (1) Plane strain analysis assuming uniaxial strain (roller) condition on the far-field lateral boundary.



$(p_y^*$ is the confinement pressure which maintains uniaxial strain condition for a tunnelless analysis.)

Figure 5.1. Comparison of Tunnel Crown Closures for Plain Strain and Generalized Plane Strain Analyses with Boundary Conditions Applied at 18a.



(P_y^* is the confinement pressure which maintains uniaxial strain condition for a tunnelless analysis.)

Figure 5.2. Comparison of Tunnel Springline Closures for Plain Strain and Generalized Plane Strain Analyses with Boundary Conditions Applied at $18a$.

- (2) Generalized plane strain analysis with a uniaxial strain (roller) condition on the far-field lateral boundary where the average out-of-plane stress is equal in magnitude to the ideal free-field lateral stress.
- (3) Generalized plane strain analysis with uniform lateral stress applied to the far-field lateral boundary where both the lateral stress and the average out-of-plane stress are equal to the ideal free-field lateral stress.

The closure results are nearly identical for the two cases in which the lateral boundary is confined with a roller boundary; however, closure increases when the free-field lateral stress boundary is used. This clearly suggests that a relatively small change to underconfinement causes rather large changes in tunnel closures.

The non-uniform stress and strain distributions at the $6a$ boundary obtained for the uniaxial strain boundary condition at $18a$ are shown in Figures 5.3 and 5.4, respectively. Figure 5.4 indicates that in the SRI tests an improved idealization of the free-field test could result by zeroing the strain along the lateral boundary at a location $5a$ above the mid-height, instead of $2a$. Thus, the SRI test procedure is essentially overconfined and non-conservative.

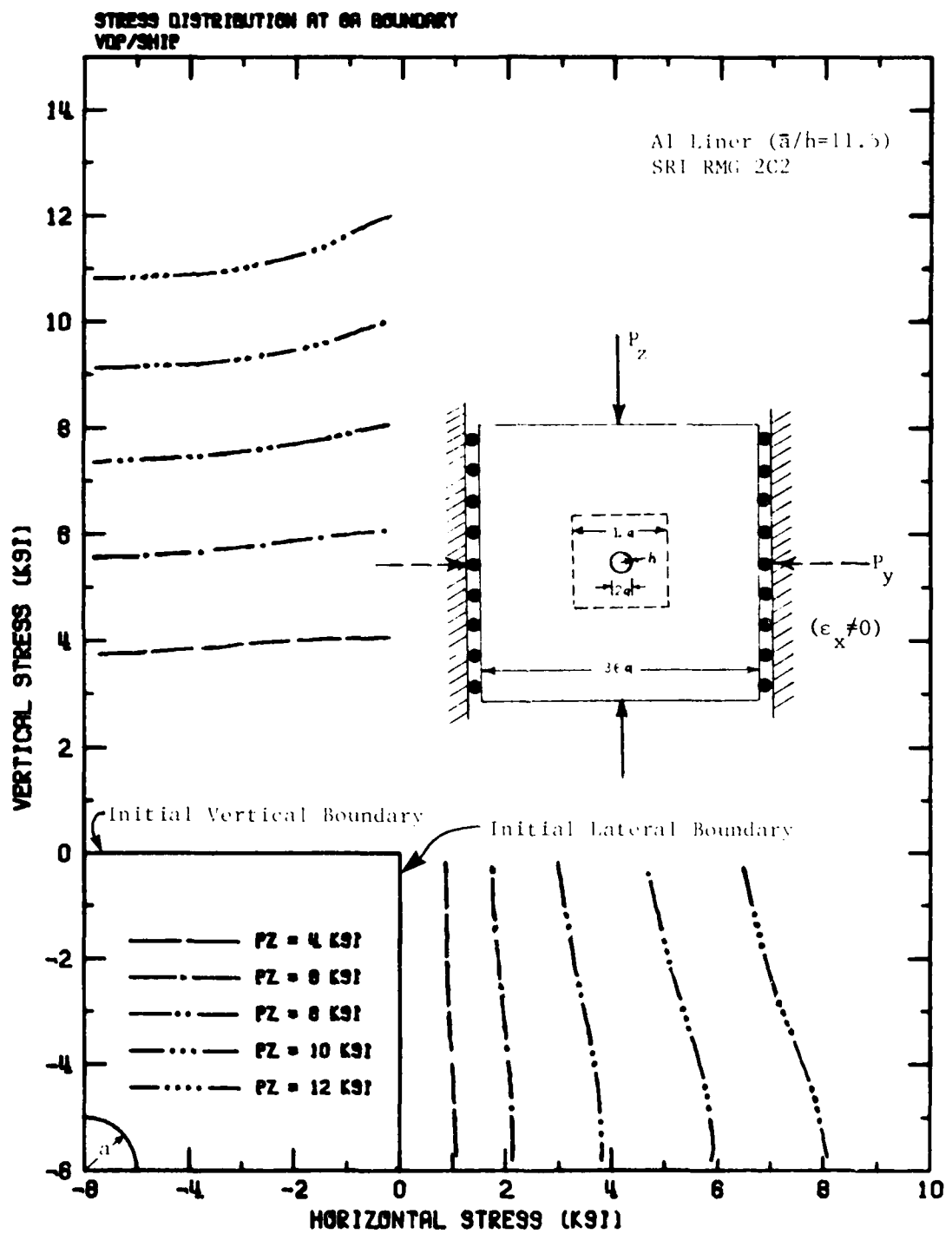


Figure 5.3. Stress Distribution at $6a$ Boundary for the Generalized Plane Strain Analysis with Roller Boundaries at $18a$.

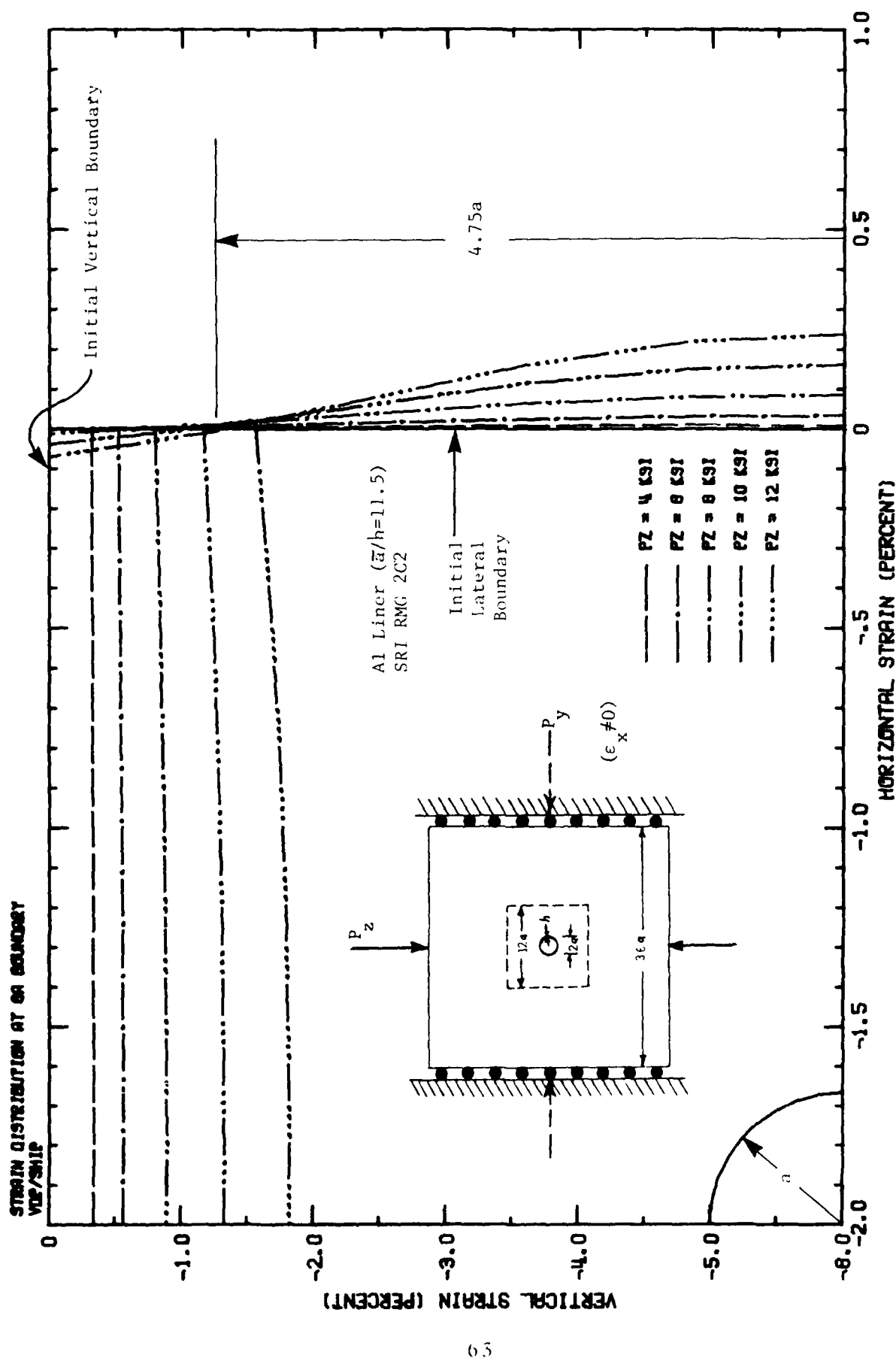


Figure 5.4. Strain Distribution at 6a Boundary for the Generalized Plane Strain Analysis with Roller Boundaries at 18a.

SECTION 6

EFFECT OF MATERIAL BEHAVIOR ON TUNNEL RESPONSE

This section presents the numerical analyses of tunnel response to variations in material behavior. Variability in material characteristics for RMG 2C2 (material used in the SRI static and dynamic tests) appears to be important, based on deviations in tunnel response that occurred in "identical" static and dynamic tests. The numerical analyses show the sensitivity of tunnel response to material strength (i.e., SRI test sensitivity to RMG 2C2 strength). In addition, they provide data on the variations in tunnel response which are likely to occur from differences in RMG 2C2 and actual tuff material strengths.

6.1 EFFECT OF MATERIAL PROPERTY VARIATIONS

Triaxial compression tests on material samples taken from the MIGHTY EPIC/DIABLO HAWK site indicate considerable variability. Figure 6.1 illustrates the scatter in the failure surface data corresponding to 31 triaxial compression tests of MIGHTY EPIC tuff. The material selected for the majority of the testing performed at SRI was RMG 2C2, a tuff simulant. RMG 2C2 has a material behavior which reasonably approximates MIGHTY EPIC tuff for a wide range of pressure. Nevertheless, the geological heterogeneity in MIGHTY EPIC tuff will inevitably be greater than RMG 2C2, hence the variation in tunnel closures in the SRI tests are likely to be less than in actual site tests.

Figure 6.2 shows the scatter in failure surface data corresponding to five separate tests performed on RMG 2C2 by WES. Also indicated in this figure are the three sets of material properties used for the present sensitivity study. The variability in the assumed material properties exceeds the scatter in the WES experimental data. However, the WES tests were performed on specimens

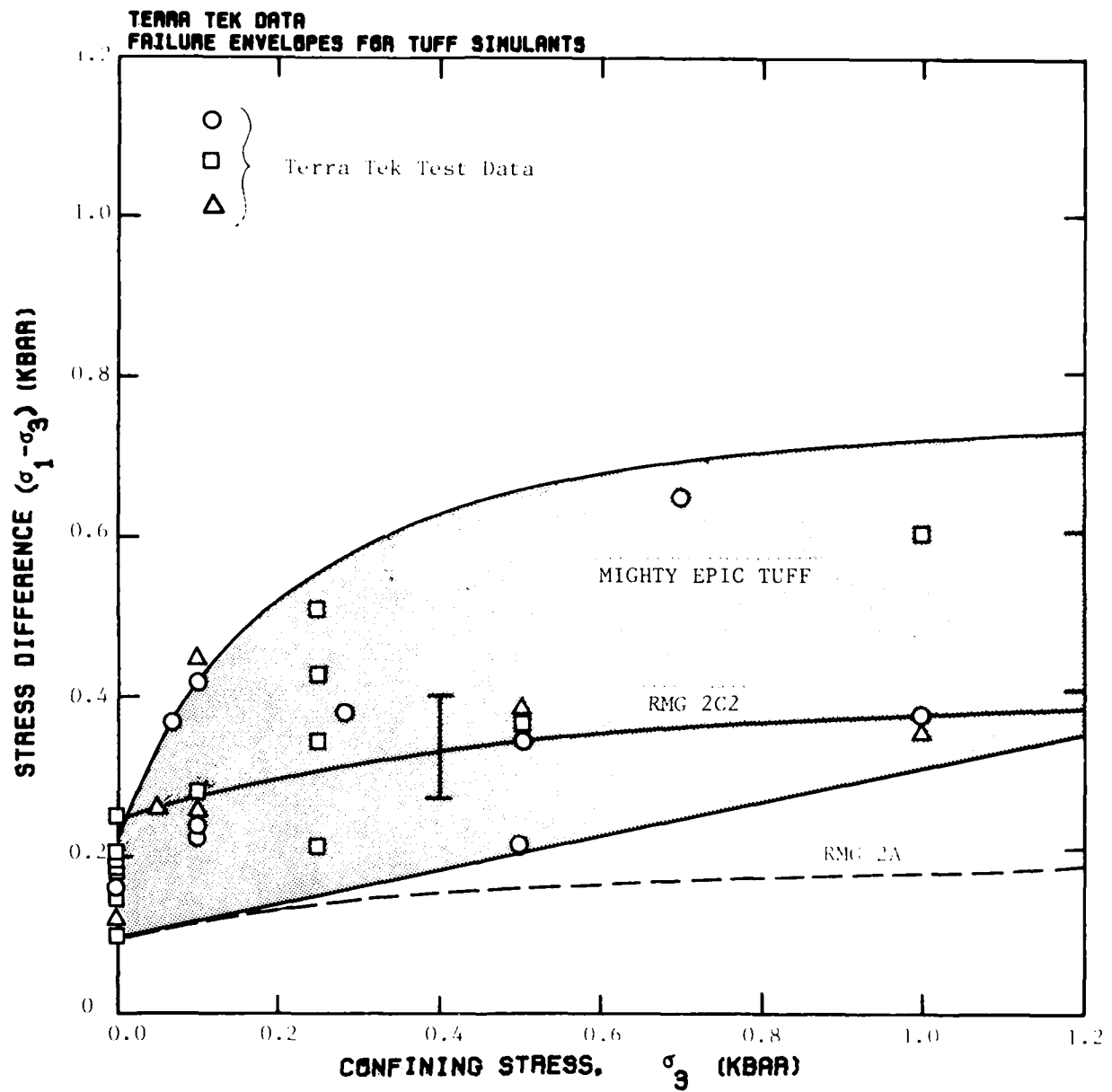


Figure 6.1 Failure Envelopes for MIGHTY EPIC/DIABLO HAWK Tuff and Grout Simulants. From SRI 5.

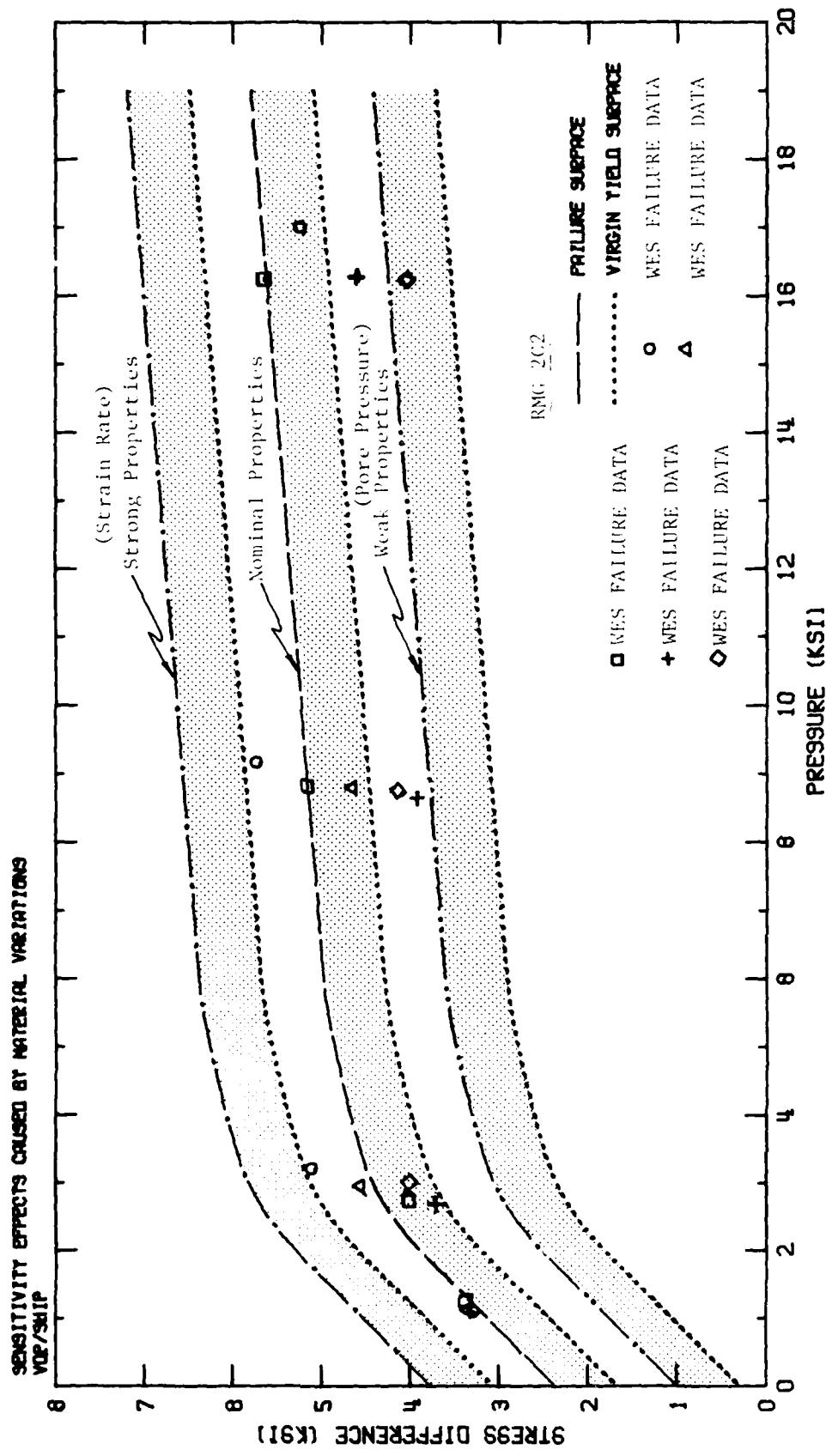


Figure 6.2. Variations in Material Properties for Sensitivity Study.

with unknown water content under static conditions, whereas in the SRI tests, the water content varied from dry to saturated under static and dynamic conditions. The three sets of material properties reflect assumed nominal (dry), strong (strain rate effect) and weak (porewater effect) behavior.

The numerical analyses regarding the effects of material variability on tunnel closure were performed using a plane strain model with rigid confinement on the lateral boundary at $r = 6.4a$, the numerical simulation of an ideal uniaxial strain boundary at $6.4a$. The results of this study are summarized in Figures 6.3 through 6.5. In Figure 6.3, the applied-confinement pressures for the material parameter study are compared with the SRI experimental data (the analytical lateral pressure represents the average lateral stress). Figures 6.4 and 6.5 compare tunnel crown and spring-line closures. The numerical predictions agree quite well with the experimental measurements for both confinement and closure.

The calculated results not only match the experimental, but also the band in experimental data matches reasonably well with the one for the assumed material variations. Actually, the scatter in the experimental data is more than likely a consequence of a small variation in lateral confinement, rather than a material variation. The variability in material strength used in this study represents a reasonable set of bounds to tuff found at the MIGHTY EPIC site. In summary, these analyses indicate that the scatter in SRI test data caused by material variations and/or slight variation in lateral confinement are likely to be less than those observed in-situ.

6.2 RATE EFFECTS

SRI test data for tunnel closure indicates that major differences occur under quasi-static and dynamic loading environments. Figure 4.1 shows typical static and dynamic test data for uniaxial

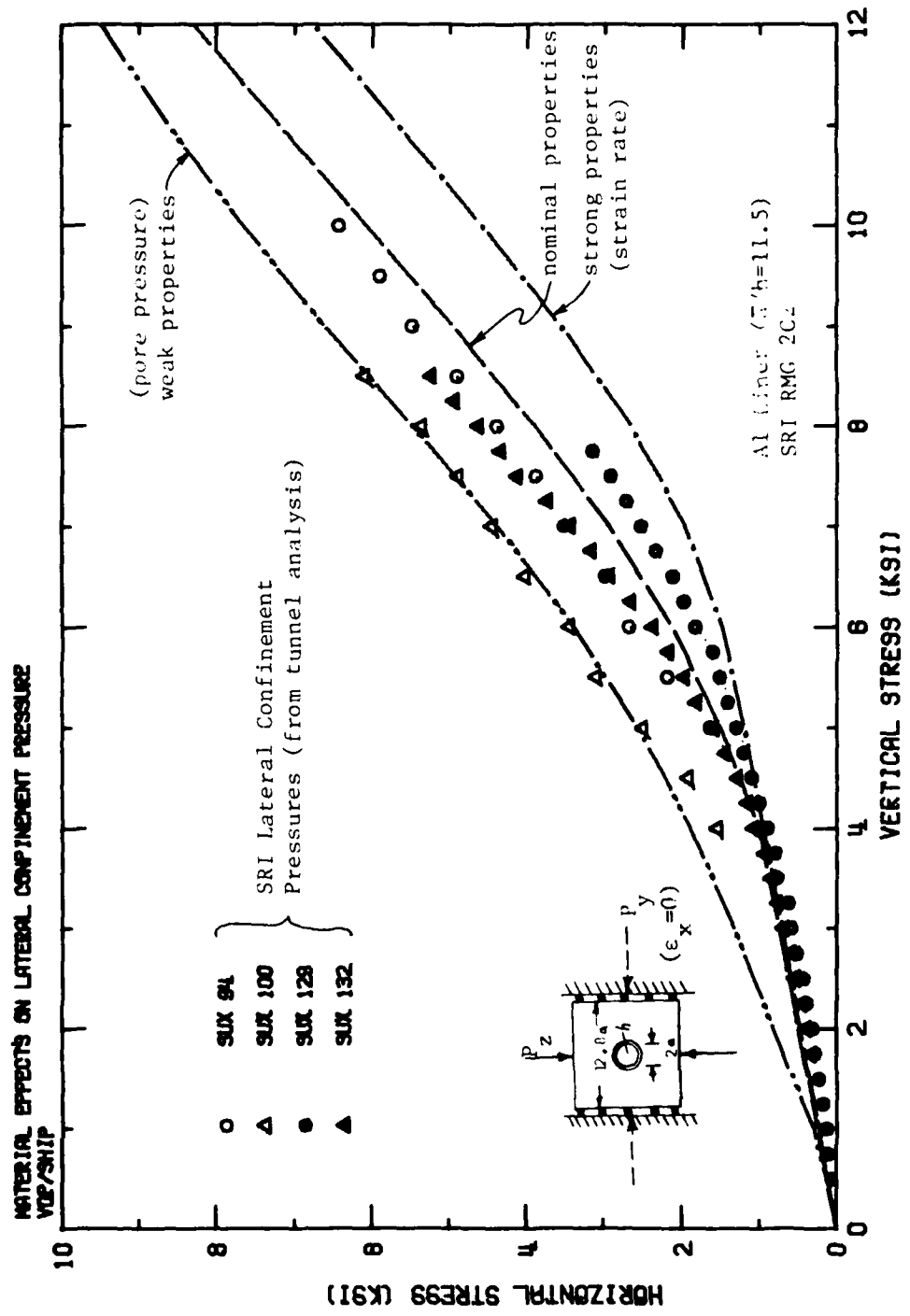


Figure 6.3. Effects of Material Property Variations on the Confinement Stress at the 6.4a Boundary.

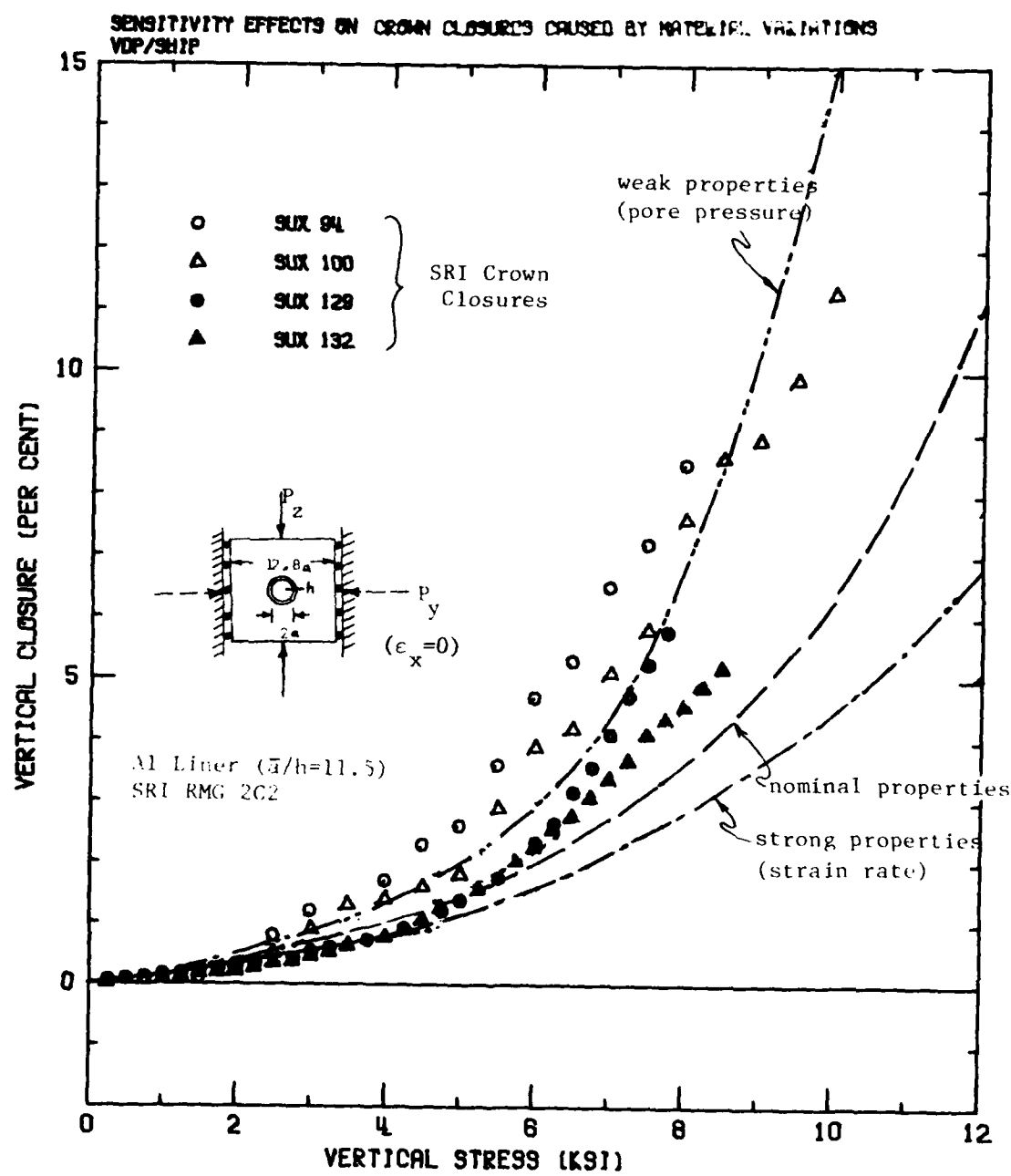


Figure 6.4. Effects of Material Property Variations on Tunnel Crown Closures.

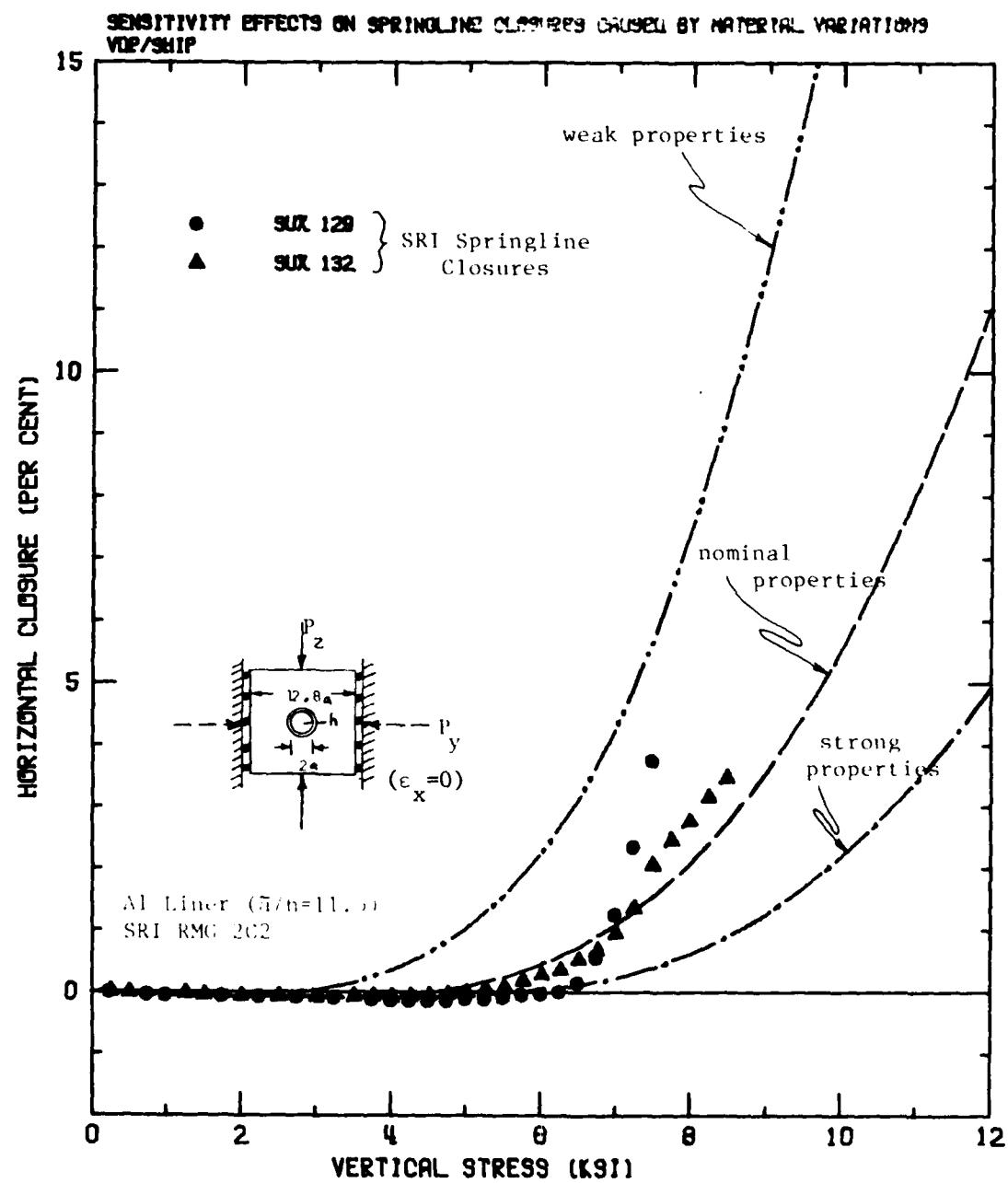


Figure 6.5. Effects of Material Property Variations on Tunnel Springline Closures.

strain loading of SRI RMG 2C2. This figure clearly indicates the relative reduction in tunnel distortion for dynamically loaded specimens. The loading in the SRI simulated dynamic *uniaxial strain* test is difficult to control, and most dynamic uniaxial strain tests were overconfined. Overconfinement results in less closure and may be responsible for at least a portion of the differences in closures between static and dynamic uniaxial strain tests. Nevertheless, substantial differences in tunnel distortions occurred for static and dynamic testing under *isotropic* loading (see Figure 1.5), where dynamic loading could be controlled. This implies that the differences in static and dynamic uniaxial strain tests are not merely the product of overconfined dynamic tests.

Typical rise times in the SRI dynamic tests are on the order of 2 msec. Based on the material properties and the dimensions of the test specimens (4-inch diameter) the rise times for the dynamic test loading are very slow compared to wave speeds. Hence, inertia effects should not be significant. However, the blast loading in the dynamic tests produces strain rates several orders of magnitudes greater than static tests. These high strain rates may effectively strengthen the material and thereby cause less closure in dynamic tests.

The procedure employed by SRI for the measurement of tunnel distortion varies under static and dynamic loadings. In static tests, tunnel closures are monitored with increasing load, providing a continuous closure-load relationship. It is also recognized that in dynamic tests, tunnel closure is measured only after the load is removed. This procedure provides only one closure-load relation, i.e., the *final* tunnel closure versus *peak* dynamic load. Therefore, the dynamic closure measurement does not represent the peak closure which may differ from final closure due to recovery that occurs during unloading. During unloading the medium near

the tunnel may also experience inelastic behavior (loss of strength in low pressure states), causing tunnel closure measurements to deviate substantially from the peak closure.

A series of numerical analyses were performed to provide information regarding the importance of the following effects:

- (1) Recovery during unloading
- (2) Inertia effects
- (3) Material rate effects

The results of this numerical investigation are summarized in Figure 6.6. The solid line illustrates the differences between peak closures and closures measured after unloading (7% peak versus 5%). This result was generated by a static analysis using nominal material properties. The dashed line shows the influence of *inertia* on closure. (As anticipated, the inertia effects are not significant, i.e., SRI dynamic tests are essentially quasi-static.) The dash-dot line shows the effect of increasing the yield strength to account for strain-rate dependent material properties. Finally, the dash-double-dot line gives the effect of decreasing the yield strength to account for pore-water pressure under static loading.

The increase in strength is assumed to account for strain rate effects (a 25% increase in failure strength for pressure levels at 12 ksi). Including strain rate effects and recovery due to unloading accounts for a significant portion of the differences that occur between tests (for $P_y = 12$ ksi: dynamic closure = 3.5%, static closure = 7%). These results agree very well with the experimental data.

In summary, it appears that material strain rate is the dominant effect in reducing tunnel closure in dynamic tests and

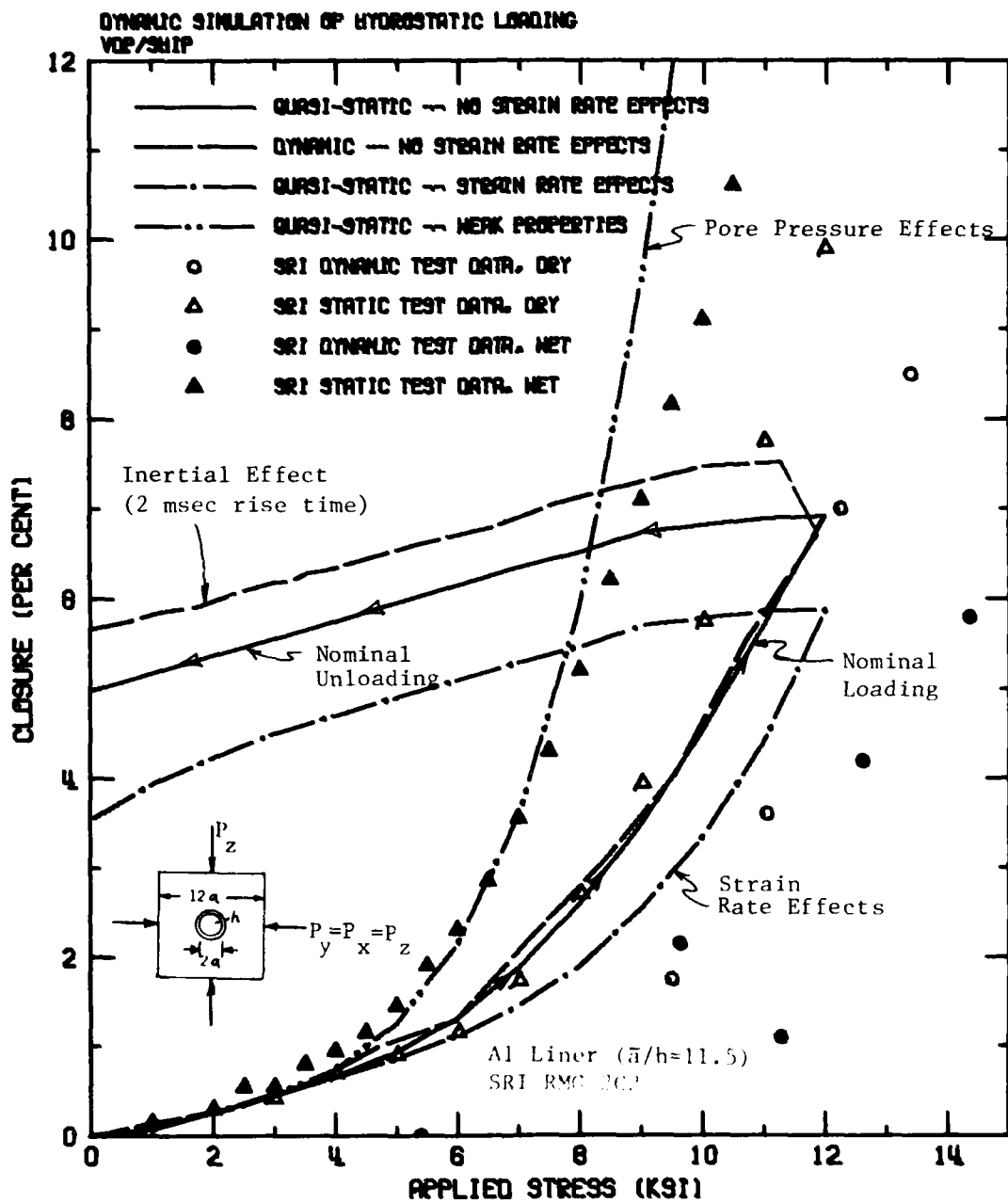


Figure 6.6. Comparison of Inertia and Strain Rate Effects for Dynamic Hydrostatic Loading Simulations.

porewater pressure is the dominant effect in increasing tunnel closure in static tests. Clearly the recovery during unloading is appreciable, but secondary. Inertia effects, as expected, are small.

Because of the substantial differences that occurred in static and dynamic tests, it would be prudent to first perform static and dynamic material tests on solid material specimens (i.e., no tunnel) in future test series. These tests would indicate material rate and porewater effects as well as provide a data base regarding strain rate and porewater effects.

SECTION 7

SENSITIVITY OF TUNNEL RESPONSE TO LATERAL CONFINEMENT

In this section the results of a series of numerical analyses are used to evaluate and interpret the sensitivity of small-scale tests (i.e., tunnel closures and lateral boundary behavior) to over- and underconfinement. An explicit definition for neutral confinement of a *finite* test specimen is difficult to establish, although four reasonable definitions are:

- (1) Uniform lateral confinement pressure that corresponds to the result obtained for tunnel-free uniaxial strain conditions. This gives a lower bound to the confinement pressure.
- (2) Uniaxial strain (roller) lateral boundary which could result in a non-uniform lateral confinement pressure. This gives an upper bound to the confinement pressure.
- (3) Uniform lateral confinement pressure required to maintain zero lateral displacement (hoop strain) on the specimen at the location corresponding to the SRI simulated* uniaxial test (i.e., $\sim 2a$ above the mid-height).
- (4) Uniform lateral confinement pressure required to maintain zero lateral displacement (hoop strain) on the specimen at the location corresponding to free-field analyses (e.g., $\sim 5a$ above the mid-height as indicated in Section 5).

Of course, as the specimen boundary increases (relative to the tunnel diameter, $2a$) all four definitions become more equivalent. It is the possible interaction of the tunnel response with the lateral

*In the SRI simulation the sum of two strain gauge (180° apart) measurements is set to zero. This usually implies that one measurement is positive and the other is negative, and not that the lateral displacement is actually zero.

boundary behavior which makes an explicit definition for neutral confinement difficult.

A series of five separate analyses were performed to evaluate the effects of uniform lateral confinement pressure on tunnel response. Figure 7.1 indicates the various ratios of vertical confinement-lateral confinement pressures used in this study. The lateral confinement pressure corresponding to a tunnel-free uniaxial strain test was used as the lower bound case. The lateral confinement pressure was increased in ten percent increments for the other four analyses. The tunnel crown and springline closures obtained for these analyses are shown in Figure 7.2 and 7.3, respectively. These results clearly indicate the sensitivity of tunnel crown closure to small changes in lateral pressure, especially near lower bound (underconfined) conditions.

The associated sensitivity of the response of the specimen's lateral boundary is shown in Figure 7.4. Note that as the confinement pressure is increased, the lateral bulging decreases with zero lateral displacement at $z = 5a$ for $P_H = \sim 1.1P_L^*$ and at $z = 2a$ for $P_H = \sim 1.2P_L^*$ (where P_L^* is the lower bound tunnel-free confinement pressure).

In order to show the sensitivity of tunnel closure to confinement, the results of the present study are re-plotted in Figure 7.5 and compared with the four definitions of neutral confinement. Examining Figure 7.5 shows tunnel closures to be extremely sensitive to underconfinement using all four definitions of neutral confinement. These results also show that the definition of neutral confinement can significantly influence the behavior of tunnel closure (and lateral boundary) response. On the other hand, as the test specimen is overconfined, the tunnel crown closure approaches that for the ideal uniaxial strain (roller) boundary state. Note, however, that the overall tunnel closure (e.g., springline) response is more sensitive to overconfinement. The isotropic (hydrostatic)

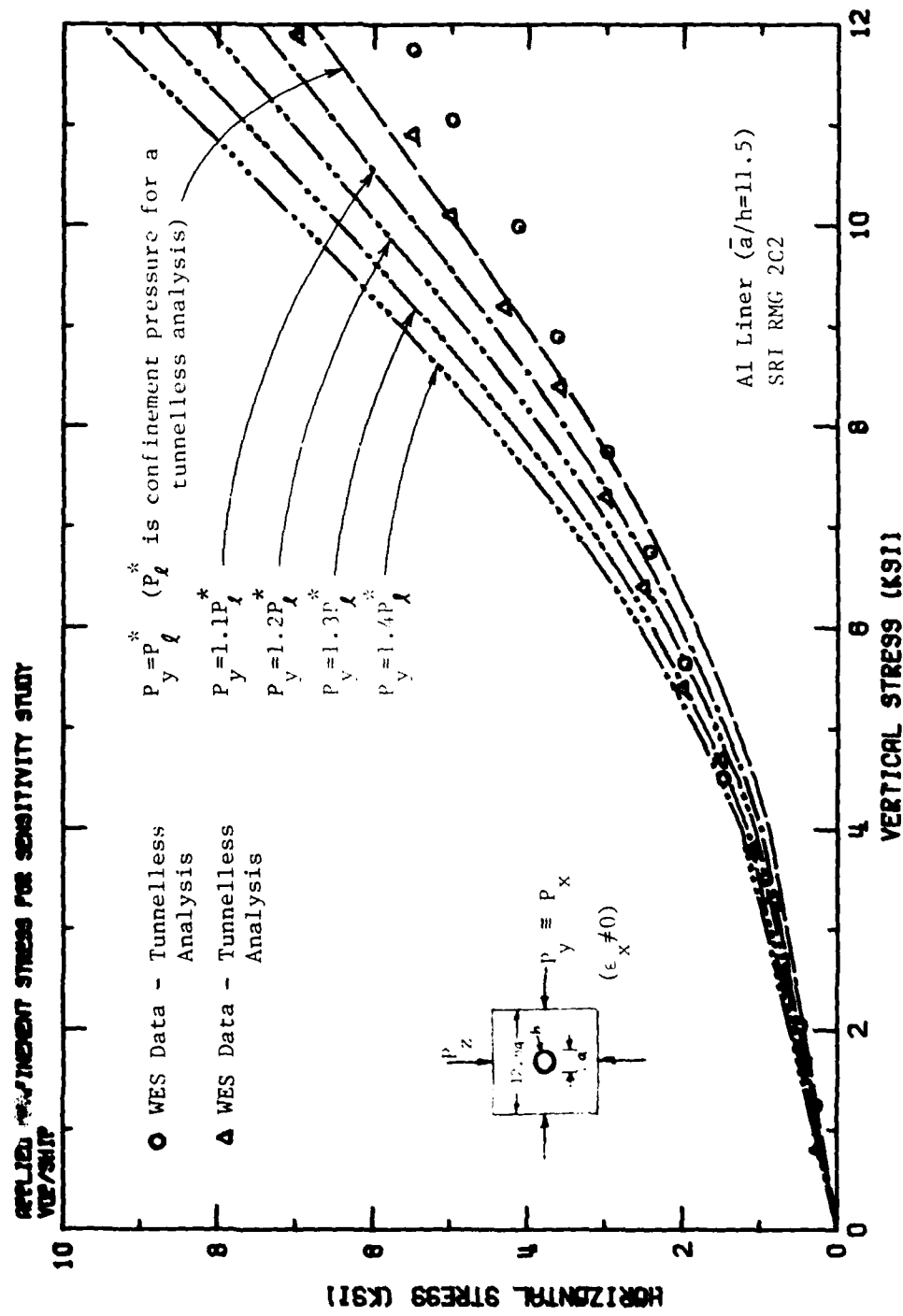


Figure 7.1. Ratios of Applied Stress/Confinement Stress Used for Sensitivity Study.

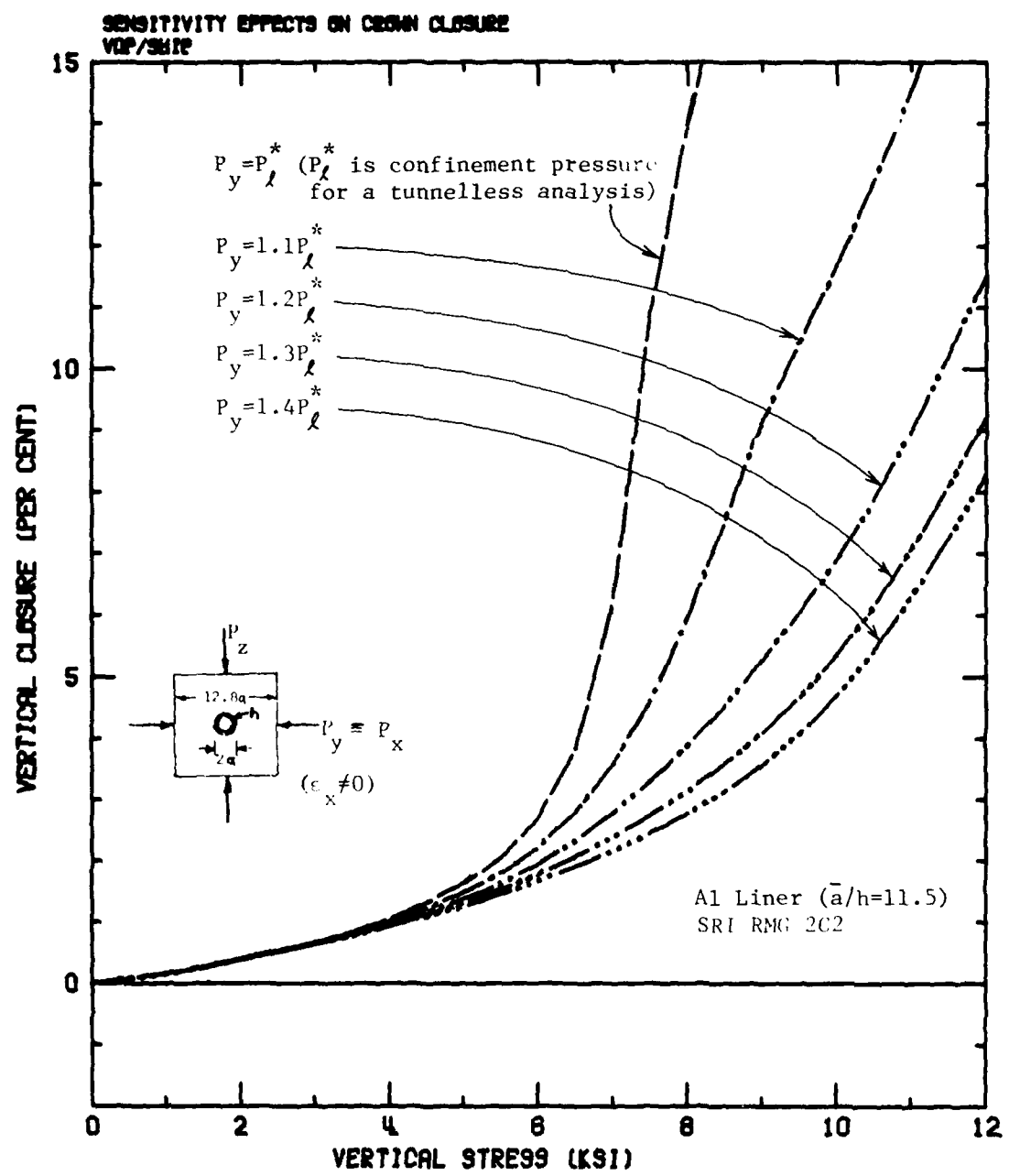


Figure 7.2. Sensitivity Effect of Lateral Confinement Pressures on Tunnel Crown Closures.

SENSITIVITY EFFECTS ON SPRINGLINE CLOSURE
VDP/SHIP

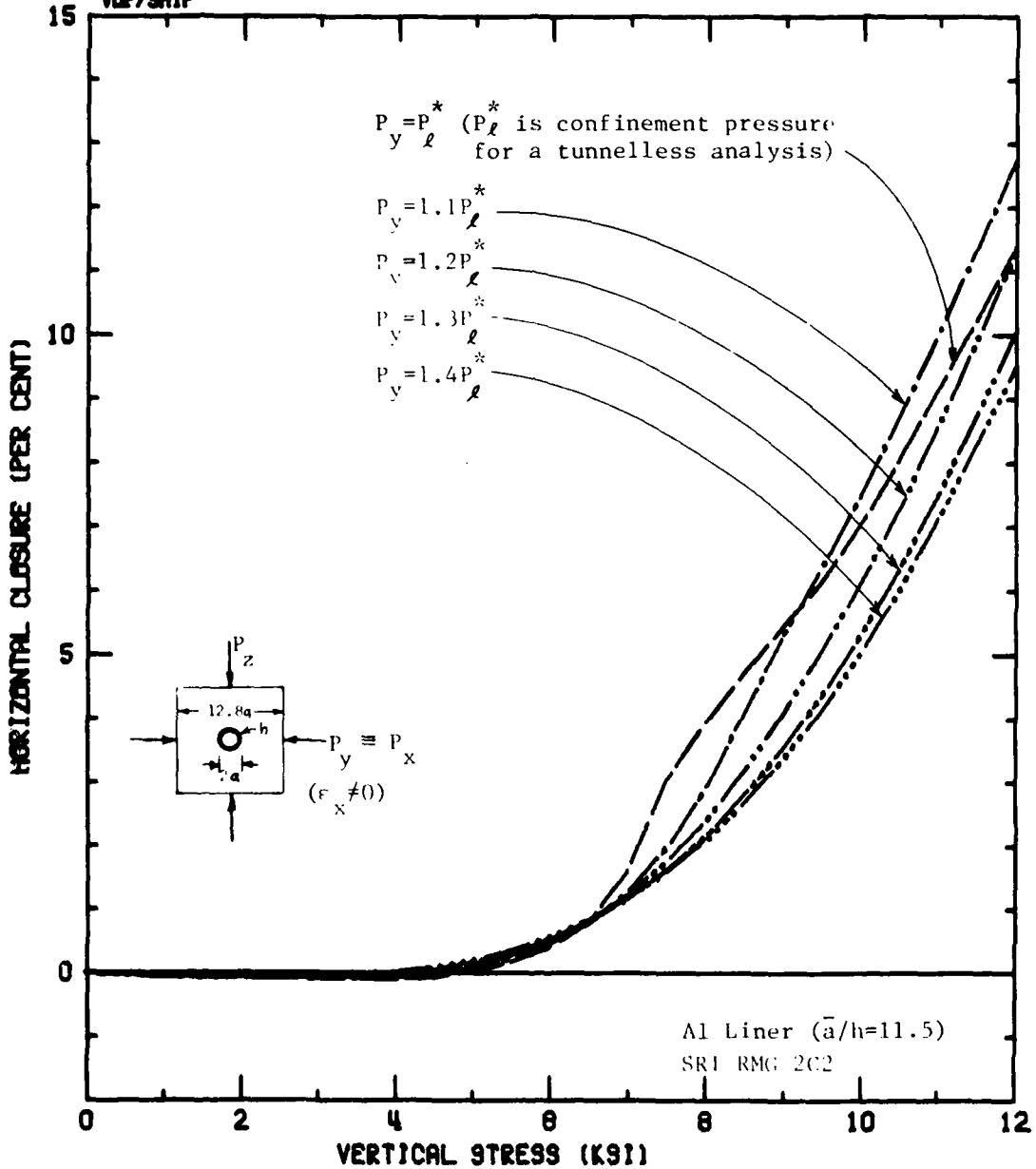


Fig. 3. Sensitivity Effect of Lateral Confinement Pressures on Tunnel Springline Closures.

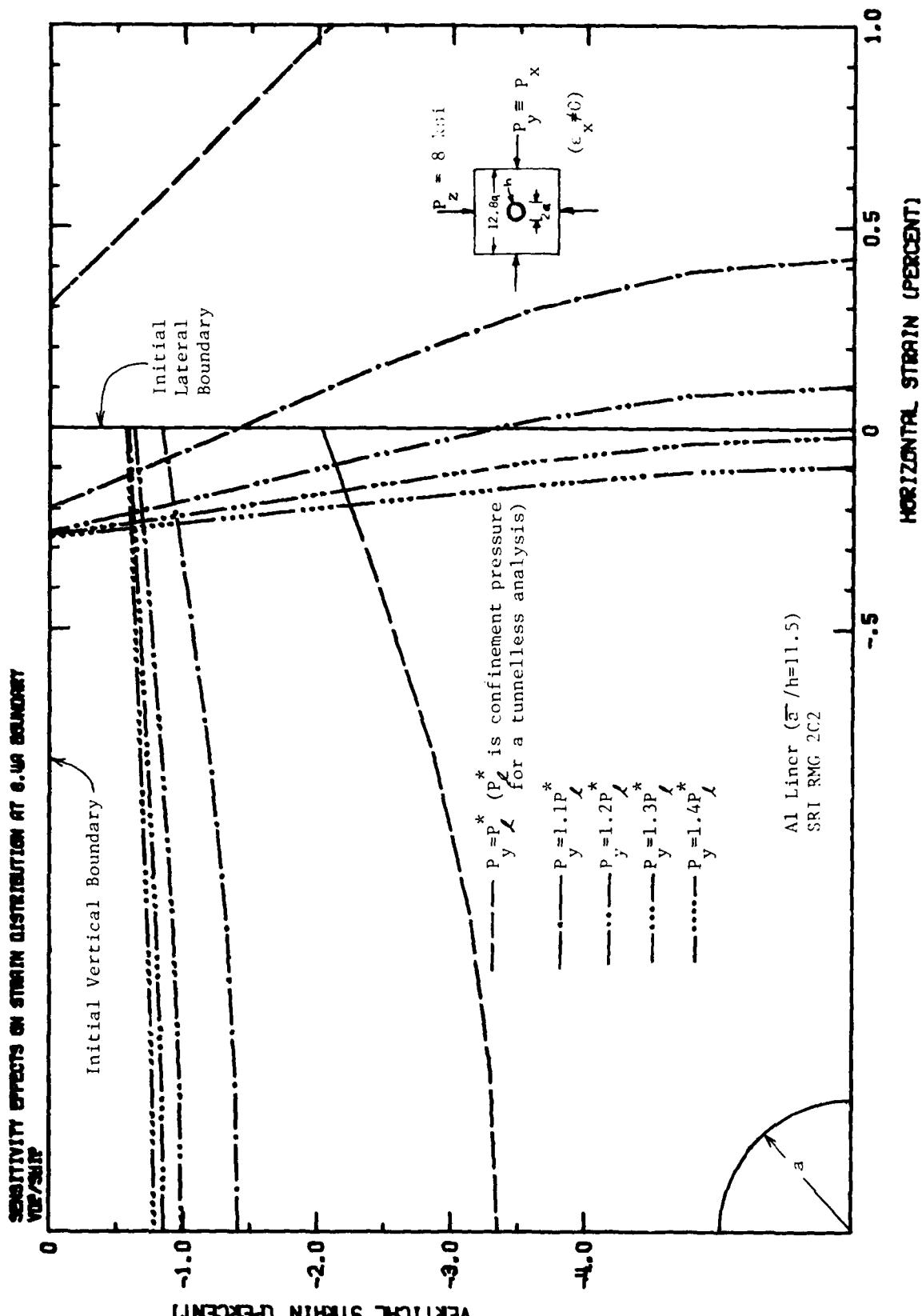


Figure 7.4. Lateral Confinement Pressure Sensitivity Effects on the Strain Profile at the 6.4a Boundary for a Vertical Applied Pressure of 8 ksi.

EFFECTS OF LATERAL CONFINEMENT STRESS ON CROWN CLOSURES
VDP/SHIP

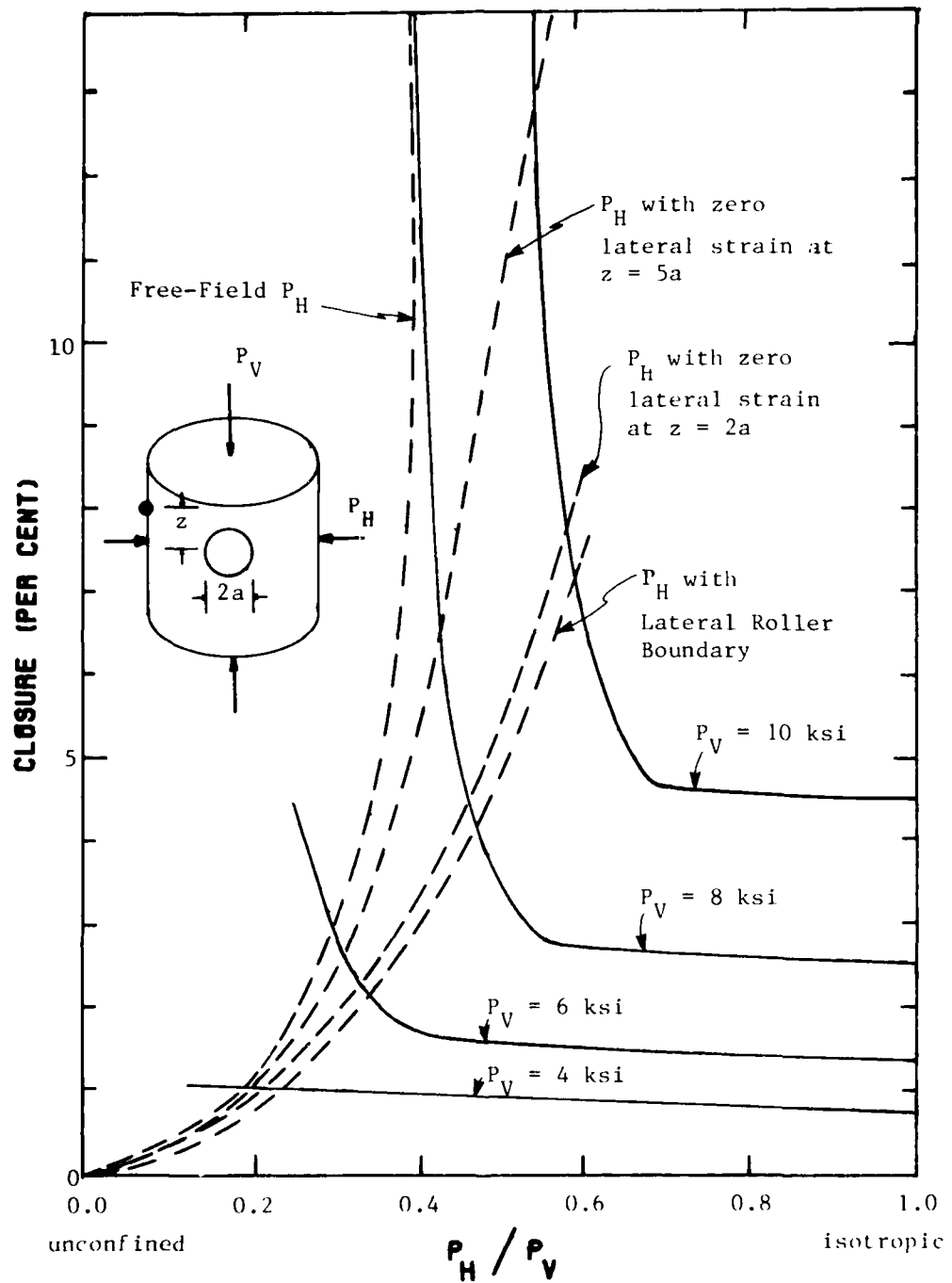


Figure 7.5. Sensitivity of Tunnel Crown Closure to Lateral Confinement Pressure for SRI RMG 2C2 Specimen with Aluminum Liner, $a/h = 11.5$.

loading condition gives smaller (less conservative) tunnel closures than uniaxial strain loading.

The numerical calculations regarding the sensitivity to lateral confinement of tunnel closure and lateral strain at the mid-height (i.e., the degree of lateral bulging) are compared with the SRI experimental results in Figures 7.6 and 7.7, respectively. The experimental closures are presented for lateral confinement pressures corresponding to the SRI simulated uniaxial strain condition (Definition 3 above), 20 percent overconfinement and 20 percent underconfinement. The theoretical calculations agree very well with experimental data with regard to the sensitivity of closure to lateral confinement, although numerical closure results are consistently smaller.

Figure 7.7 compares experimental and theoretical lateral boundary strains at mid-height. Again, the theoretical and experimental results indicate the same trends, although the analytical model predicts lateral motions *greater* than the experiment, e.g., for uniaxial loading at $P_V = 7.5$ ksi, the experimental mid-height strain was .02% compared to the analytical results of .08%, a factor of 4 greater.

It should be noted that the SRI data showed considerable scatter in lateral strain measurements apparently for identical tests. For example, six simulated uniaxial strain tests measured a scatter in lateral strain at mid-height for a vertical pressure of 7.5 ksi from +.04 percent (bulging) to -.01 percent (inward boundary motion). Although the calculated results do not lie within the band of the experimental, the numerical calculations do reflect the actual bulging observed in the experiment. Because of the scatter observed in experiments and the relative sensitivity of the lateral bulging to material variations, these differences in experimental and theoretical results should not be unexpected.

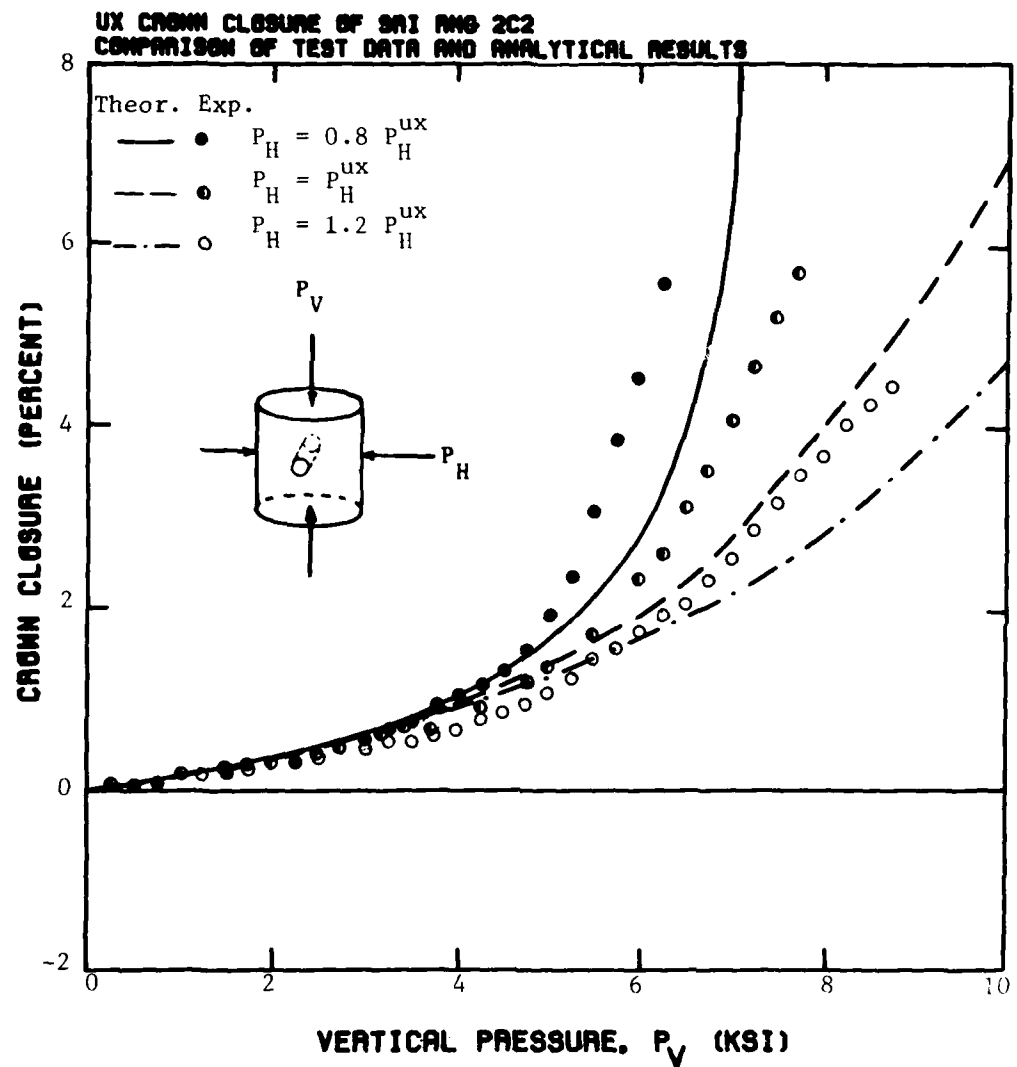


Figure 7.6. Comparison of Experimental and Theoretical Crown Closure in SRI RMG 2C2 for Uniaxial Strain, Over-confined and Underconfined Loadings. (Aluminum liner, $a/h = 11.5$. P_H^{UX} is lateral pressure required to maintain uniaxial strain as defined by SRI.)

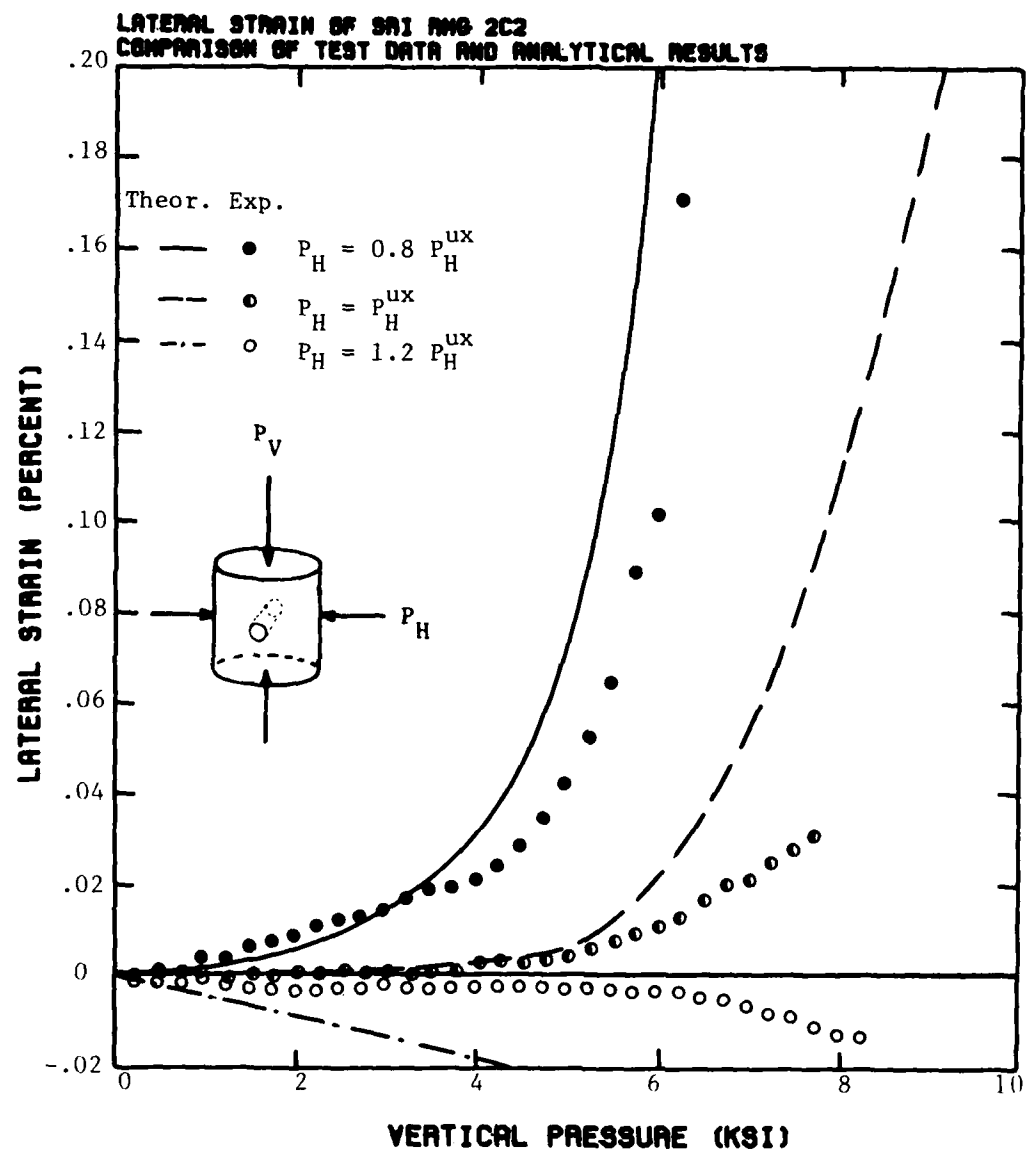


Figure 7.7. Comparison between Experimental and Theoretical Specimen Lateral Strain at Mid-Height Versus Vertical Pressure, for Uniaxial Strain, Over-confined and Underconfined Loadings of SRI RMG 2C2. (P_H^X is lateral pressure required to maintain uniaxial strain as defined by SRI.)

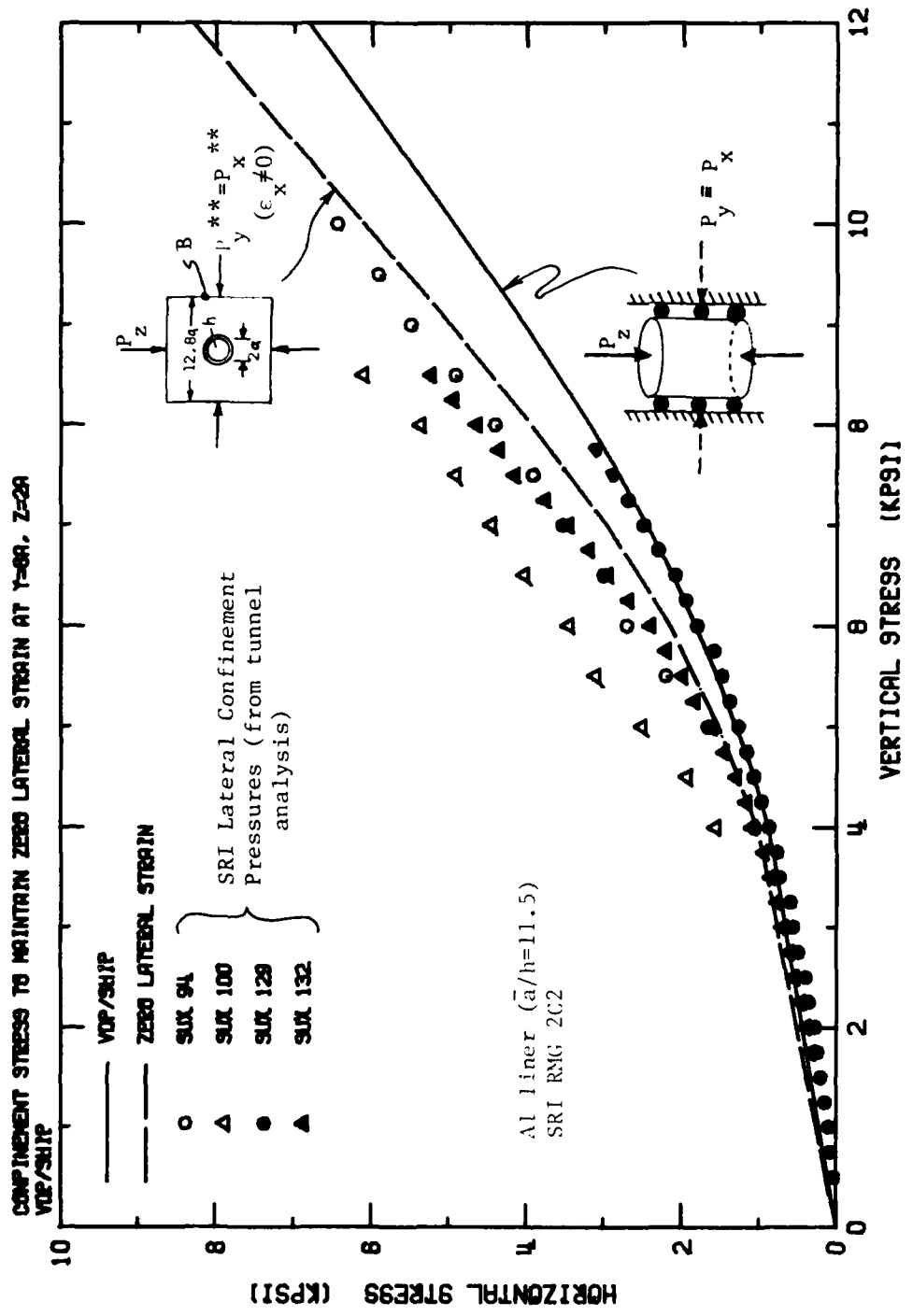
SECTION 8

NUMERICAL SIMULATION OF STATIC UNIAXIAL STRAIN EXPERIMENTS

The numerical simulation of the SRI test was performed using the generalized plane strain model described in Section 3 and the combined variable friction angle and strain hardening Drucker-Prager material model described in Appendix A. Comparing the results of these analyses with those for ideal uniaxial strain shows the following discrepancies and similarities that occur in the two tests in regard to tunnel closures, and the lateral boundary conditions.

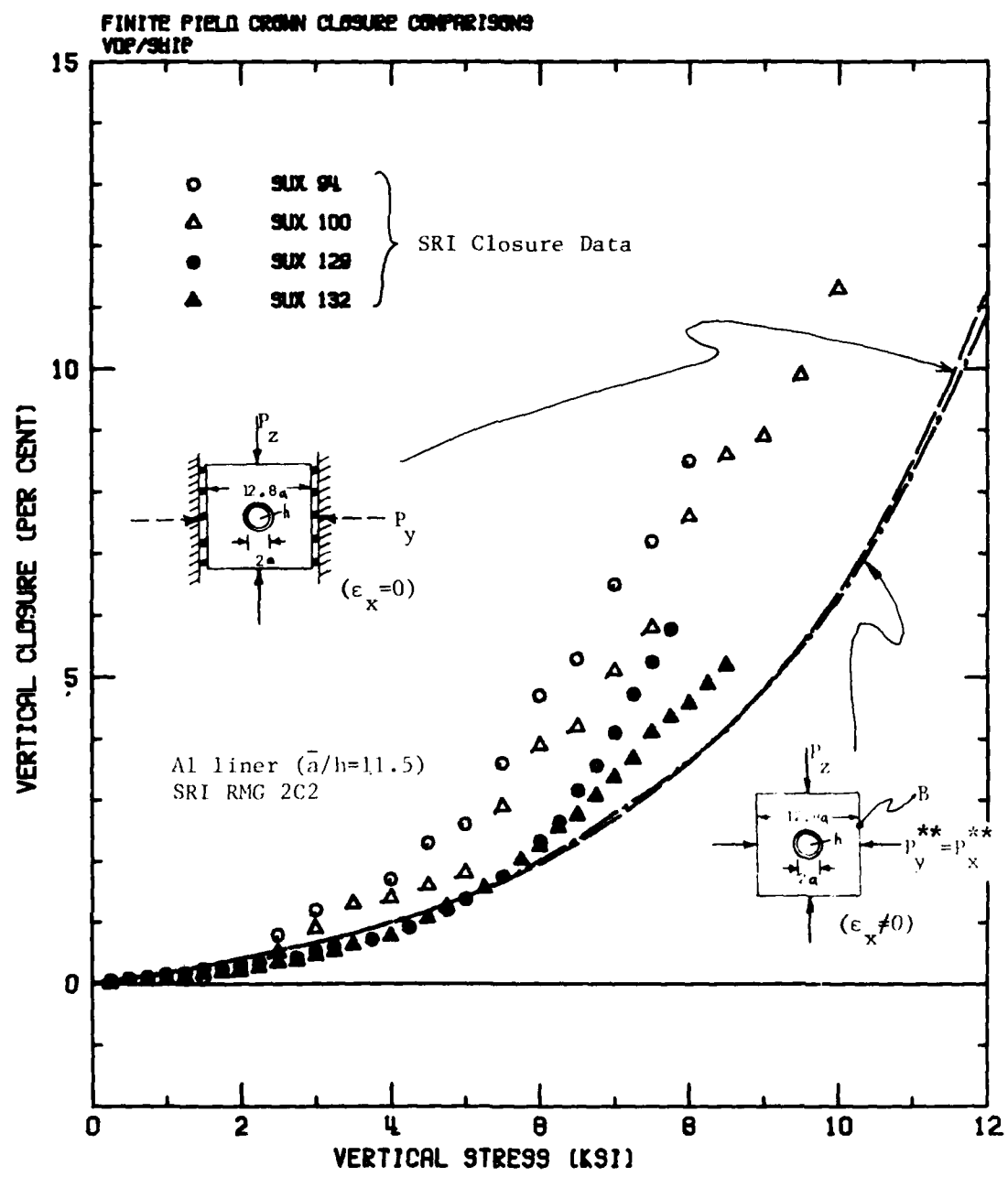
The influence of the tunnel on lateral confinement pressure is illustrated in Figure 8.1. Shown here are the ratios of the applied-confinement pressures corresponding to the free-field and the SRI simulated uniaxial strain test. Based on these results, the tunnel appears to *increase* the lateral confinement stress on the lateral boundary by approximately twenty percent. This explains the underconfined analytical results obtained in the preliminary analysis (Section 4) where the numerical simulation of the SRI uniaxial strain test was performed by essentially applying lateral pressures corresponding to free-field.

Tunnel crown and springline closures obtained from the numerical analysis for an ideal uniaxial strain and simulated uniaxial strain tests are shown in Figures 8.2 and 8.3, respectively. These numerical results indicate that for practical purposes, the SRI test duplicates tunnel closures corresponding to ideal uniaxial strain conditions. Although tunnel closures are equivalent, the deformation behavior on the lateral boundary differs significantly (see Figures 8.4 and 8.5). The analysis of the SRI test, Figure 8.5, shows significant axial variations in bulging along the lateral boundary caused by the uniform lateral pressure applied to the cylinder boundary. Note that the lateral motion is zeroed *one* tunnel diameter above the mid-height (similar to the SRI test).



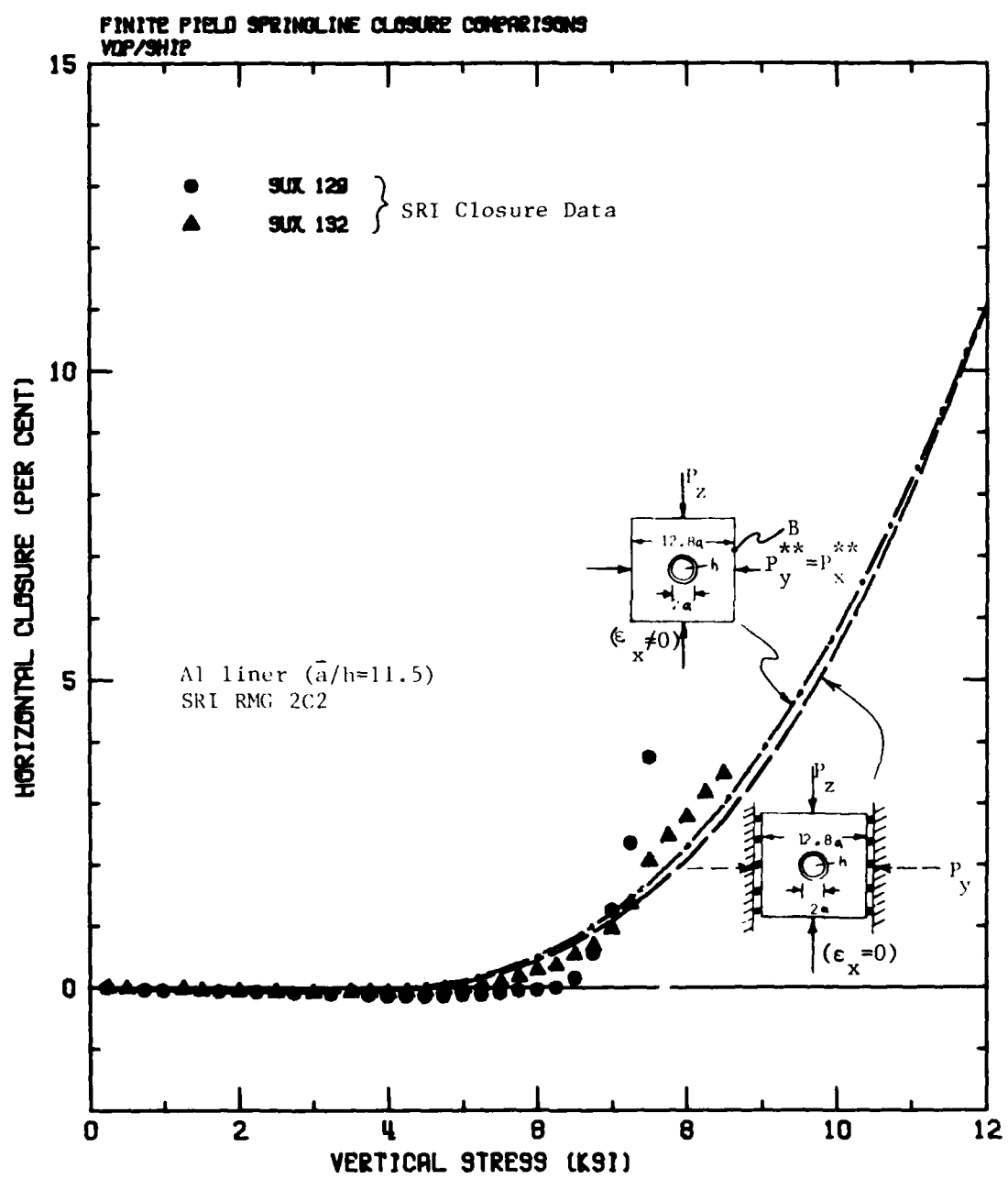
P_y^{**} is the confinement pressure adjusted until the lateral strain is zero at point B
 Located at $y = 6.4a$, $z = 2a$.)

Figure 8.1. Effects of the Tunnel on the Confinement Stress at the 6.4a Boundary.



$(p_y^{**}$ is the confinement pressure adjusted until the lateral strain is zero at point B located at $y = 6.4a$ and $z = 2a$.)

Figure 8.2. Comparison of Tunnel Crown Closures for Plane Strain and Generalized Plane Strain Analyses with Boundary Conditions Applied at 6.4a.



(P_y^{**} is the confinement pressure adjusted until the lateral strain is zero at point B located at $y = 6.4a$, $z = 2.a$.)

Figure 8.3. Comparison of Tunnel Springline Closures for Plane Strain and Generalized Plane Strain Analyses with Boundary Conditions Applied at 6.4a.

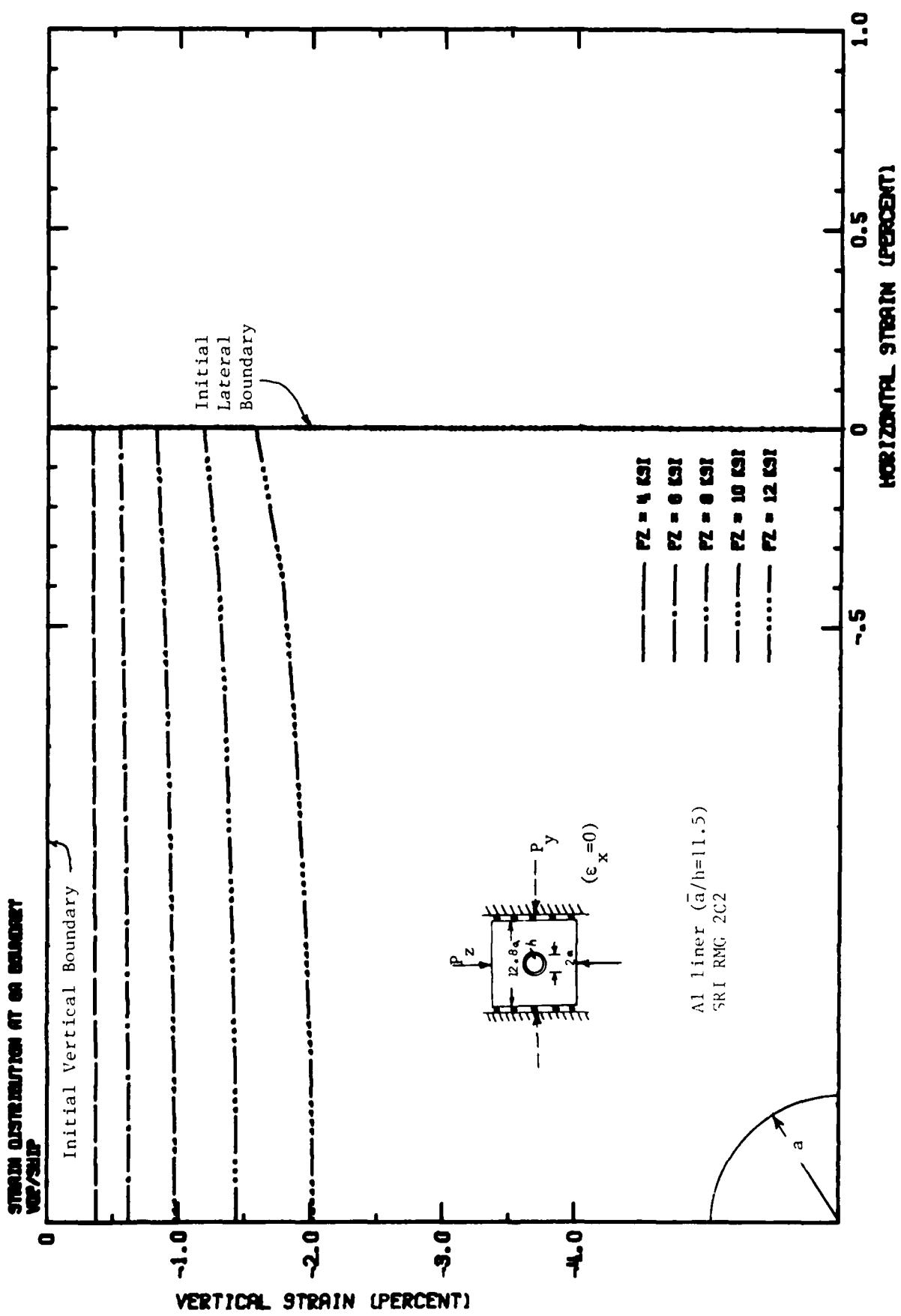
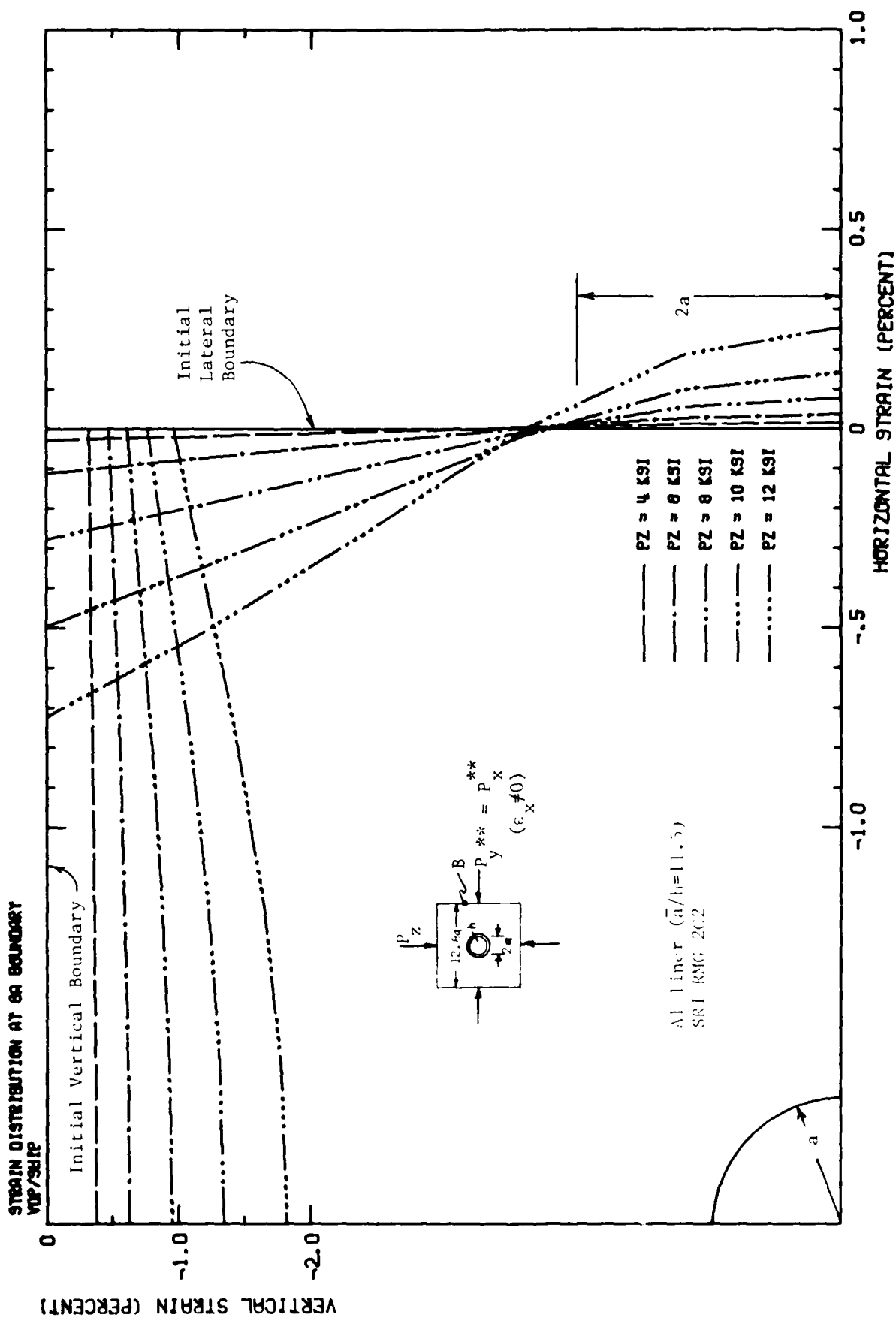


Figure 8.4. Strain Distribution at the 6.4a Boundary for the Plane Strain Analysis with Roller Boundaries at 6.4a.



(The confinement pressure P_{c}^* is adjusted until the lateral strain is zero at point B located at $y = 6.4a$, $z = 2a$.)

Figure 8.5. Strain Distribution at the 6.4a Boundary for the Generalized Plane Strain Analysis with Stress Boundaries at 6.4a, $y = 0.4a$, $z = 2a$.)

The degree of bulging follows tunnel closure, i.e., the closure and lateral bulging dependency on applied loads are similar.

The ideal uniaxial strain analysis indicates that the lateral stress P_H is *non-uniform*, see Figure 8.6, an effect which increases as tunnel closure increases. For low pressures, (elastic behavior) the ideal uniaxial strain results produced nearly uniform lateral pressures. Despite the differences in the lateral stress distributions, the intensity (average lateral stress) of the lateral forces are nearly equivalent (compare Figure 8.6 with 8.7). This suggests that tunnel response is more sensitive to the *intensity* of the lateral pressure than the *distribution*.

These analyses support the general validity of the SRI experiments as a means for predicting tunnel response of an idealized uniaxial strain test under a *static* loading environment. However, some of the results, specifically lateral boundary behavior appear inconsistent. For example, numerical analyses of the SRI simulated uniaxial strain test indicate that significant lateral bulging occurs especially at high pressure levels. This leads to the obvious question as to how the SRI test appears to deviate from the ideal uniaxial strain configuration, yet give tunnel closures which are essentially equal. The numerical investigation (see Section 7) on the sensitivity of tunnel closure and boundary behavior to over- and underconfinement suggests that lateral boundary behavior has only a secondary effect on tunnel closures when *overconfined*. Thus, any simulated uniaxial strain test that is slightly overconfined will essentially duplicate tunnel response of ideal uniaxial strain tests.

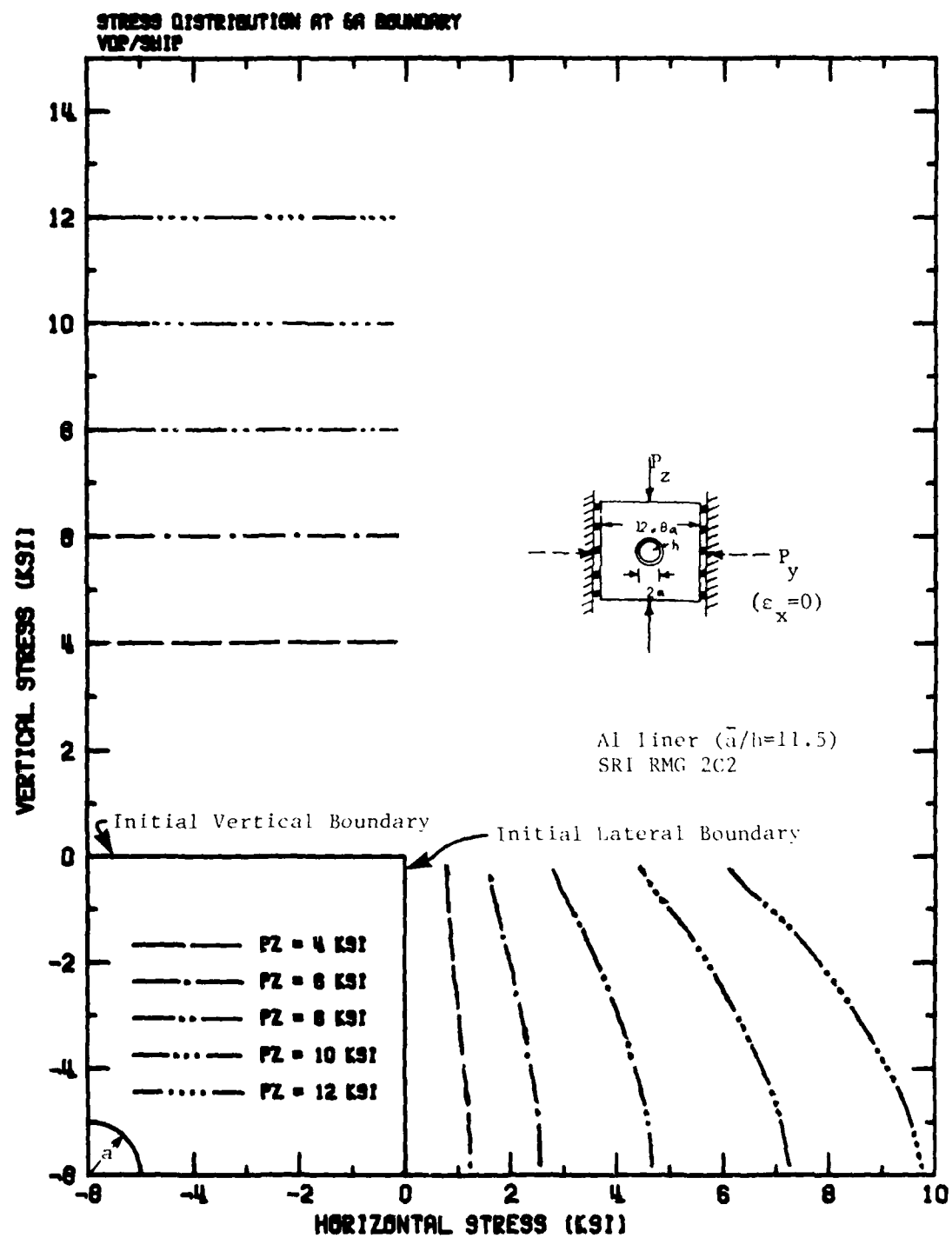
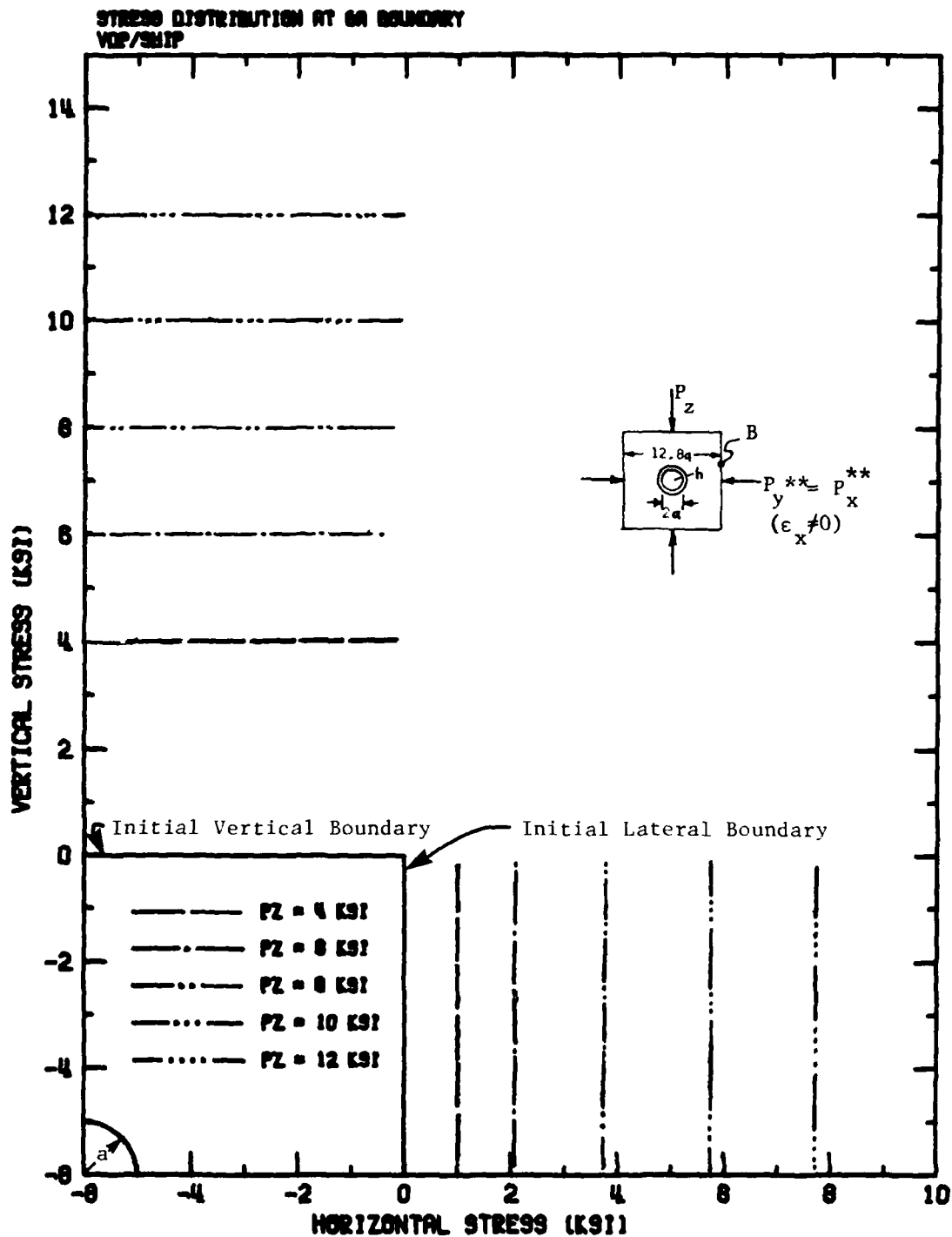


Figure 8.6. Stress Distribution at the 6.4a Boundary for the Plane Strain Analysis with Roller Boundaries at 6.4a.



(The confinement pressure P_y^* is adjusted until the lateral strain is zero at point B, located at $y = 6.4a$, $z = 2.4$.)

Figure 8.7. Stress Distribution at the 6.4a Boundary for the Generalized Plane Strain Analysis with Stress Boundaries at 6.4a.

APPENDIX A
COMBINED VARIABLE FRICTION ANGLE AND STRAIN
HARDENING DRUCKER-PRAGER MATERIAL MODEL

This appendix describes the fundamental relations for elastic-plastic materials. The mathematical development is presented for the general elastic-plastic material with the specific equations given for the combined variable friction angle and strain hardening Drucker-Prager model. Finally, the modeling capabilities of the variable Drucker-Prager model are compared with material test data for SRI RMG 2C2.

Incremental elastic-plastic behavior (i.e., derivation of the incremental stress-strain relations) requires [7] three separate entities: (1) a yield criterion that specifies three dimensional states of stress corresponding to initiation of plastic flow; (2) a flow rule relating the plastic strain increments to the current stress state; and (3) a hardening or softening rule which describes how the yield criterion is modified with the accumulation of plastic strains.

The initial yield and subsequent yield criterion for an isotropic hardening formulation can be written as

$$F(\sigma_{ij}, w^p) = 0 \quad (A-1)$$

where w^p is the accumulated plastic work defined as

$$w^p = \int_0^{\epsilon_{ij}^p} \sigma_{ij} d\epsilon_{ij}^p \quad (A-2)$$

For the combined variable friction angle and strain hardening Drucker-Prager yield criterion is defined as

$$F = \alpha J_1 + \sqrt{J_2} - K \quad (A-3)$$

where

$$\begin{aligned} J_1 &= \sigma_{kk} \\ \sqrt{J_2} &= \frac{1}{\sqrt{2}} \sqrt{(\sigma_{ij} - \frac{\sigma_{kk}}{3} \delta_{ij})(\sigma_{ij} - \frac{\sigma_{mm}}{3} \delta_{ij})} \end{aligned} \quad (A-4)$$

and α and K are material parameters which are functions of both mean stress, J_1 , and plastic work, W^p

$$\begin{aligned} \alpha &= \alpha(J_1, W^p) \\ K &= K(J_1, W^p) \end{aligned} \quad (A-5)$$

The variation in α and K with respect to hydrostatic pressure and plastic work are curve fitted to match experimental data using spline functions, Φ , where

$$\begin{aligned} \alpha &= \Phi_1(J_1) \Phi_2(W^p) \\ K &= \Phi_3(J_3) \Phi_4(W^p) \end{aligned} \quad (A-6)$$

The plastic strain increments were related to current stress state through the use of an associated flow rule. With an associated flow rule, the plastic strain increments are related to the yield function using a normality rule, i.e.,

$$d\epsilon_{ij}^p = \lambda \frac{\partial F}{\partial \sigma_{ij}} \quad (A-7)$$

For the variable Drucker-Prager model

$$d\epsilon_{ij}^p = \lambda \left[\alpha \frac{\partial J_1}{\partial \sigma_{ij}} + J_1 \frac{\partial \alpha}{\partial \sigma_{ij}} + \frac{1}{2\sqrt{J_2'}} \frac{\partial J_2'}{\partial \sigma_{ij}} - \frac{\partial K}{\partial \sigma_{ij}} \right]$$

Associate flow rules are particularly advantageous in implicit codes (e.g., NONSAP), since their use leads to symmetric system stiffness matrices. Moreover, in static analysis, associated flow rules for strain hardening materials guarantee uniqueness, whereas non-associated flow rules can lead to non-unique static solutions.

Having established the yield surface, a flow rule and the hardening characteristics, the incremental elastic-plastic stress-strain relations are obtained through algebraic manipulation. From the definition of the yield condition (i.e., during plastic flow, $F = 0$) we obtain

$$dF = 0 = \frac{\partial F}{\partial \sigma_{ij}} d\sigma_{ij} + \frac{\partial F}{\partial W^p} dW^p \quad (A-9)$$

for the variable Drucker-Prager yield condition

$$\begin{aligned} dF = 0 = & \left[\alpha \frac{\partial J_1}{\partial \sigma_{ij}} + J_1 \frac{\partial \alpha}{\partial \sigma_{ij}} + \frac{1}{2\sqrt{J_2'}} \frac{\partial J_2'}{\partial \sigma_{ij}} - \frac{\partial K}{\partial \sigma_{ij}} \right] d\sigma_{ij} \\ & + \left[J_1 \frac{\partial \alpha}{\partial W^p} - \frac{\partial K}{\partial W^p} \right] dW^p \end{aligned} \quad (A-10)$$

The increment plastic work in terms of the stress and the plastic strain increments is equal to

$$dW^p = \sigma_{ij} d\epsilon_{ij}^p \quad (A-11)$$

The stress increments are evaluated from the matrix of elastic constants and the elastic strain increments given by

$$d\sigma_{ij} = C_{ijkl}^{E1} (d\epsilon_{kl} - d\epsilon_{kl}^p) \quad (A-12)$$

Solving for λ in terms of the current stresses, σ_{ij} , and strain increments, $d\epsilon_{kl}$ (note that $\frac{\partial F}{\partial \sigma_{ij}}$ is defined in terms of the current stress state) by substituting equations A-7, A-11 and A-12 into A-9 leads to

$$\lambda = \frac{\frac{\partial F}{\partial \sigma_{ij}} C_{ijkl}^{E1} d\epsilon_{kl}}{\frac{\partial F}{\partial \sigma_{mn}} C_{mnop}^{E1} \frac{\partial F}{\partial \sigma_{op}} - \frac{\partial F}{\partial \sigma_{op}} \sigma_{op} \frac{\partial F}{\partial \sigma_{op}}} \quad (A-13)$$

The incremental stress-strain relationships are finally determined by substituting equations A-13 and A-7 into A-12 which gives the following tangent constitutive matrix

$$d\sigma_{ij} = C_{ijkl}^{\text{Tan}} d\epsilon_{kl}$$

where

$$C_{ijkl}^{\text{Tan}} = C_{ijkl}^{E1} - \frac{C_{ijrs}^{E1} \frac{\partial F}{\partial \sigma_{rs}} \frac{\partial F}{\partial \sigma_{tu}} C_{tukl}^{E1}}{\frac{\partial F}{\partial \sigma_{mn}} C_{mnop}^{E1} \frac{\partial F}{\partial \sigma_{op}} - \frac{\partial F}{\partial \sigma_{op}} \sigma_{op} \frac{\partial F}{\partial \sigma_{op}}}$$

A comparison of the combined variable friction angle and strain hardening Drucker-Prager model with the actual experimental data provided by WES is shown in Figures A-1 through A-3. These figures clearly demonstrate the improved modeling capabilities of the

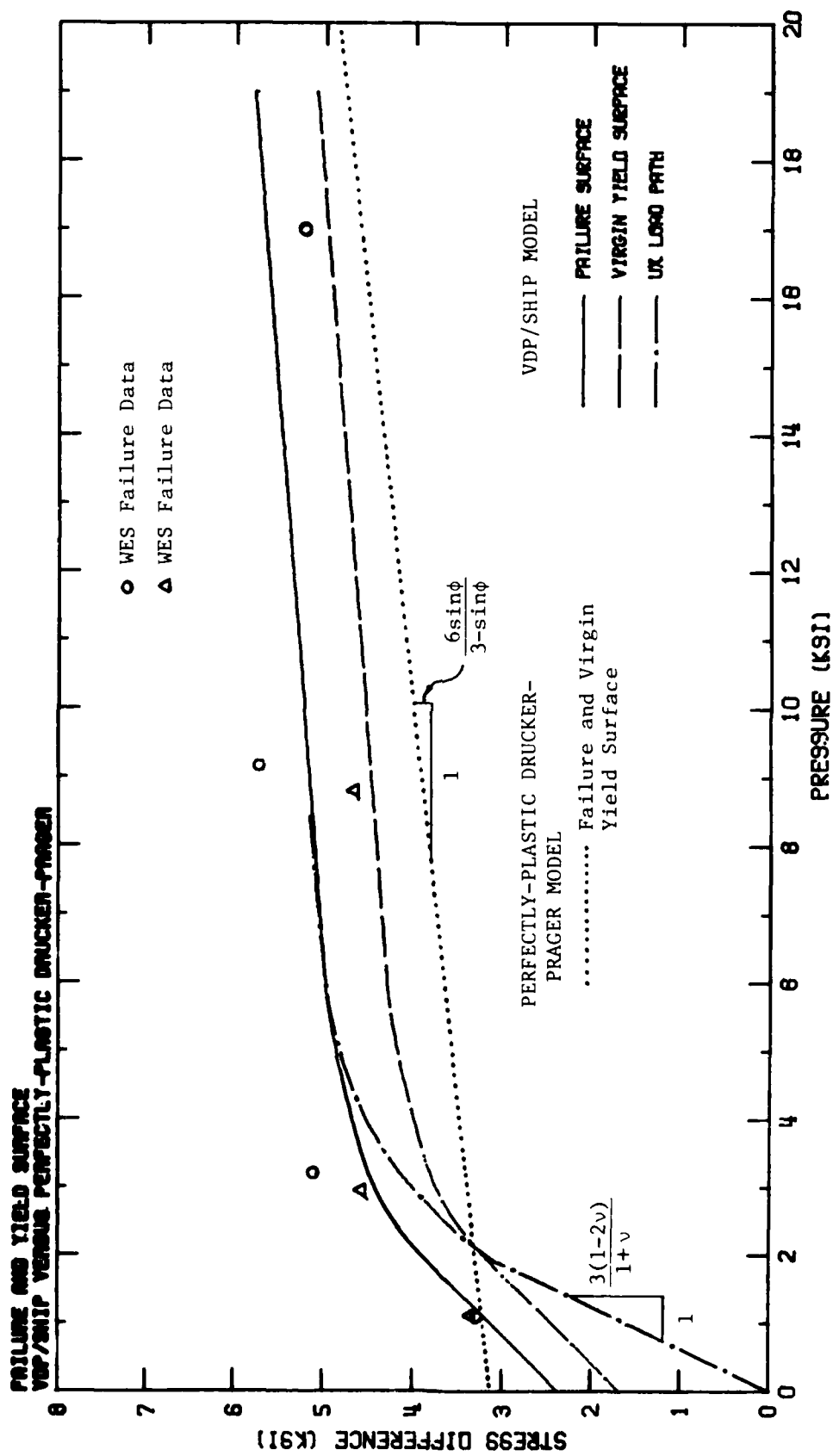


Figure A-1. Comparison of Failure and Yield Surfaces for the Combined Variable Friction Angle and Strain Hardening Versus Perfectly-Plastic Drucker-Prager Models of SRI RMG 2C2. ($v=0.182$, $\phi=2.5^\circ$)

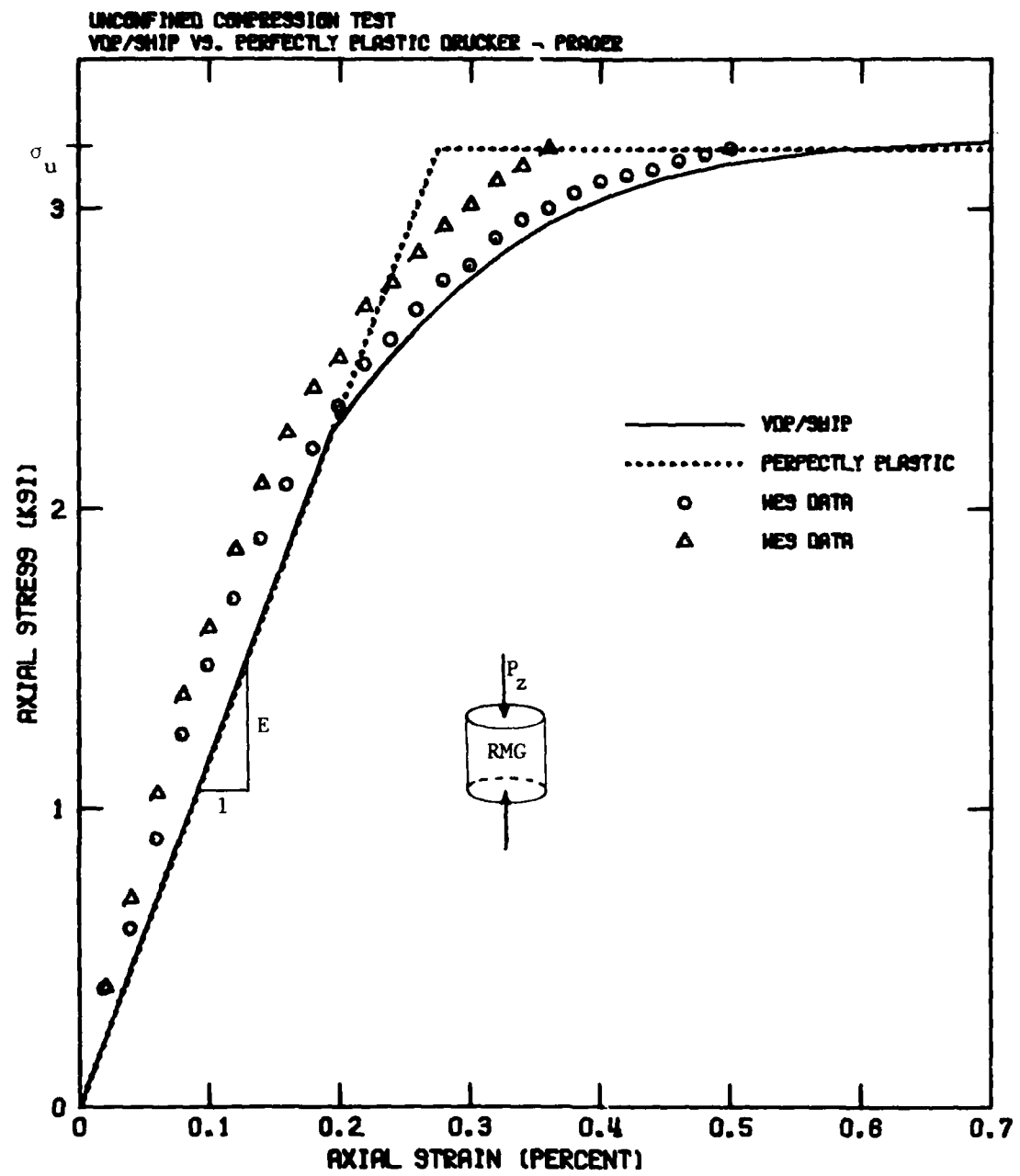


Figure A-2. Comparison of Unconfined Compression Stress-Strain Characteristics for the Combined Variable Friction Angle and Strain Hardening Versus Perfectly-Plastic Drucker-Prager Models of SRI RMG 2C2. ($E = 1.16 \times 10^6 \text{ psi}$, $\sigma_u = 3200 \text{ psi}$.)

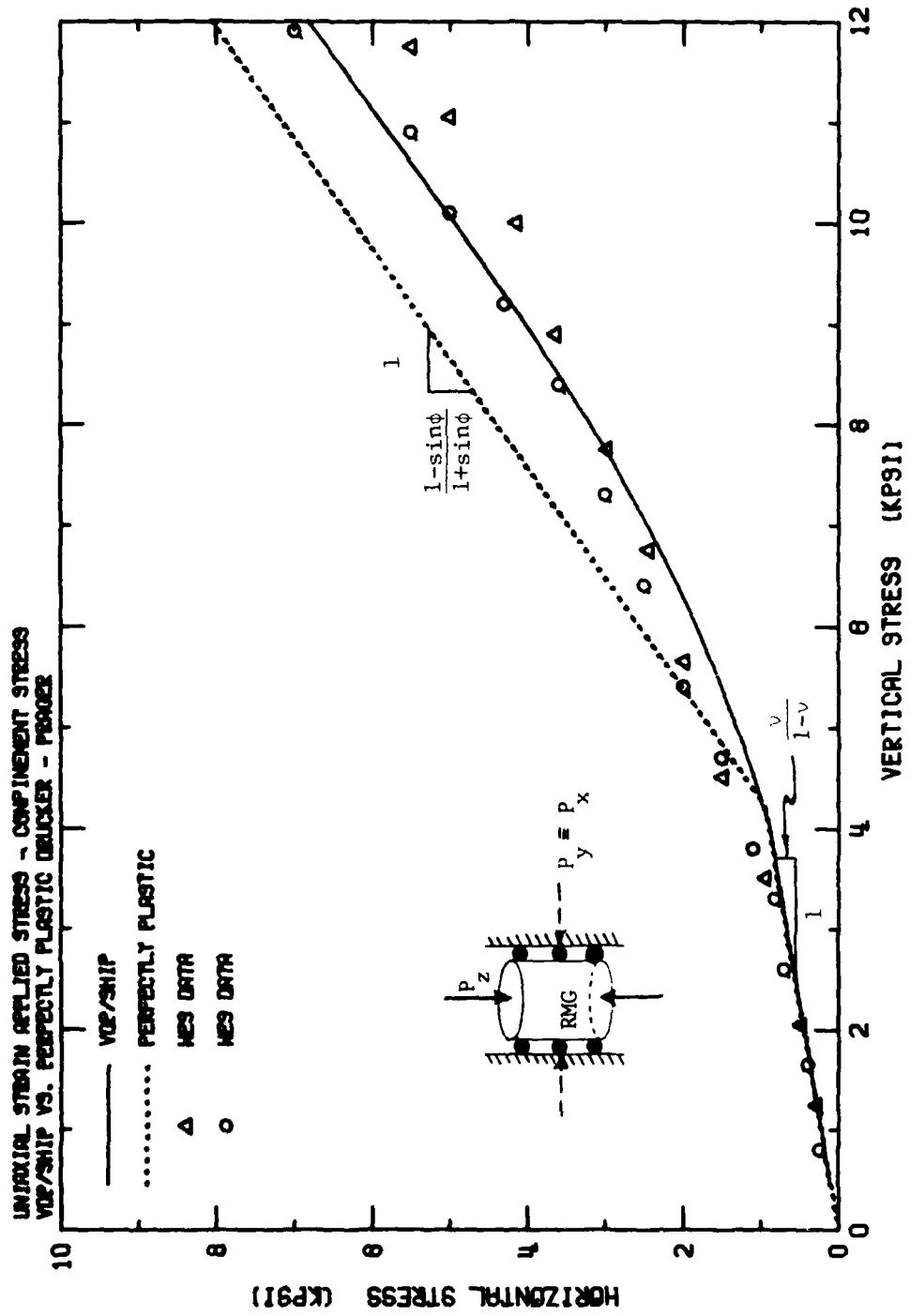


Figure A-3. Comparison of Uniaxial Strain Loading Applied Stress-Confinement Stress for the Combined Variable Friction Angle and Strain Hardening Versus Perfectly-Plastic Drucker-Prager Models of SRI RMG 2C2 ($\nu = 0.182$, $\phi = 2.5^\circ$).

combined variable friction angle and strain hardening Drucker-Prager model over the perfectly-plastic Drucker-Prager (or Mohr-Coulomb) model.

APPENDIX B
ELASTIC-PLASTIC MODIFIED MOHR-COULOMB
MATERIAL MODEL

The Drucker-Prager criterion originally evolved as a 3-D generalization to the planar Mohr-Coulomb yield law. The Drucker-Prager criterion simplifies the mathematics encountered with associated flow rules. In fact, the 3-D Mohr-Coulomb criterion cannot be directly used as a flow rule for states of stress having two identical principal stresses (e.g., triaxial compression). The Mohr-Coulomb criterion is modified to remove this problem, as detailed in the following.

The Mohr-Coulomb material model is based on the Coulomb slip concept. That is, the shear stress (τ) required for simple slip is considered to depend upon the cohesion (c) and linearly upon the normal stress (σ_n) to the slip surface, Figure B-1. This can be stated as:

$$\tau = c - \sigma_n \tan\phi$$

where ϕ is the so-called friction angle. In terms of principal stresses ($\sigma_1 > \sigma_2 > \sigma_3$) this becomes:

$$\sigma_1 - \sigma_3 = 2c \cos\phi - (\sigma_1 + \sigma_3) \sin\phi$$

This function, which can be considered a pressure dependent Tresca condition, represents a hexagonal pyramid in stress space, Figure B-2. The yield function depends only on the extreme values of stress and is independent of the intermediate stress. This is shown in the π -plane intersection as each side of the Mohr-Coulomb surface is parallel to a stress axis.

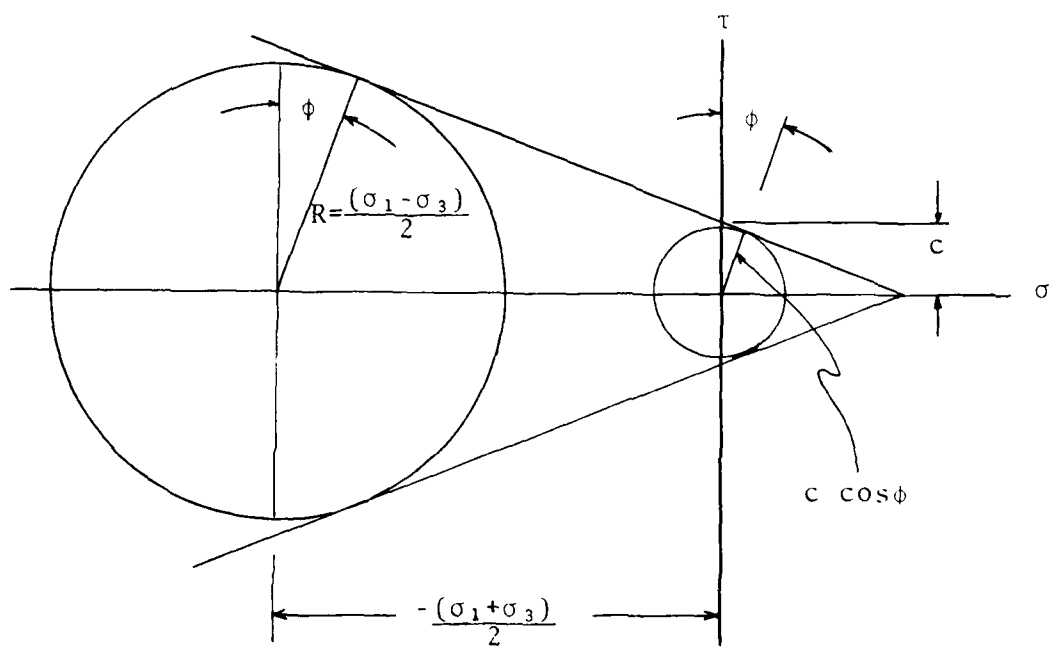


Figure B-1. Mohr Circle Representation of Mohr-Coulomb Yield Surface.

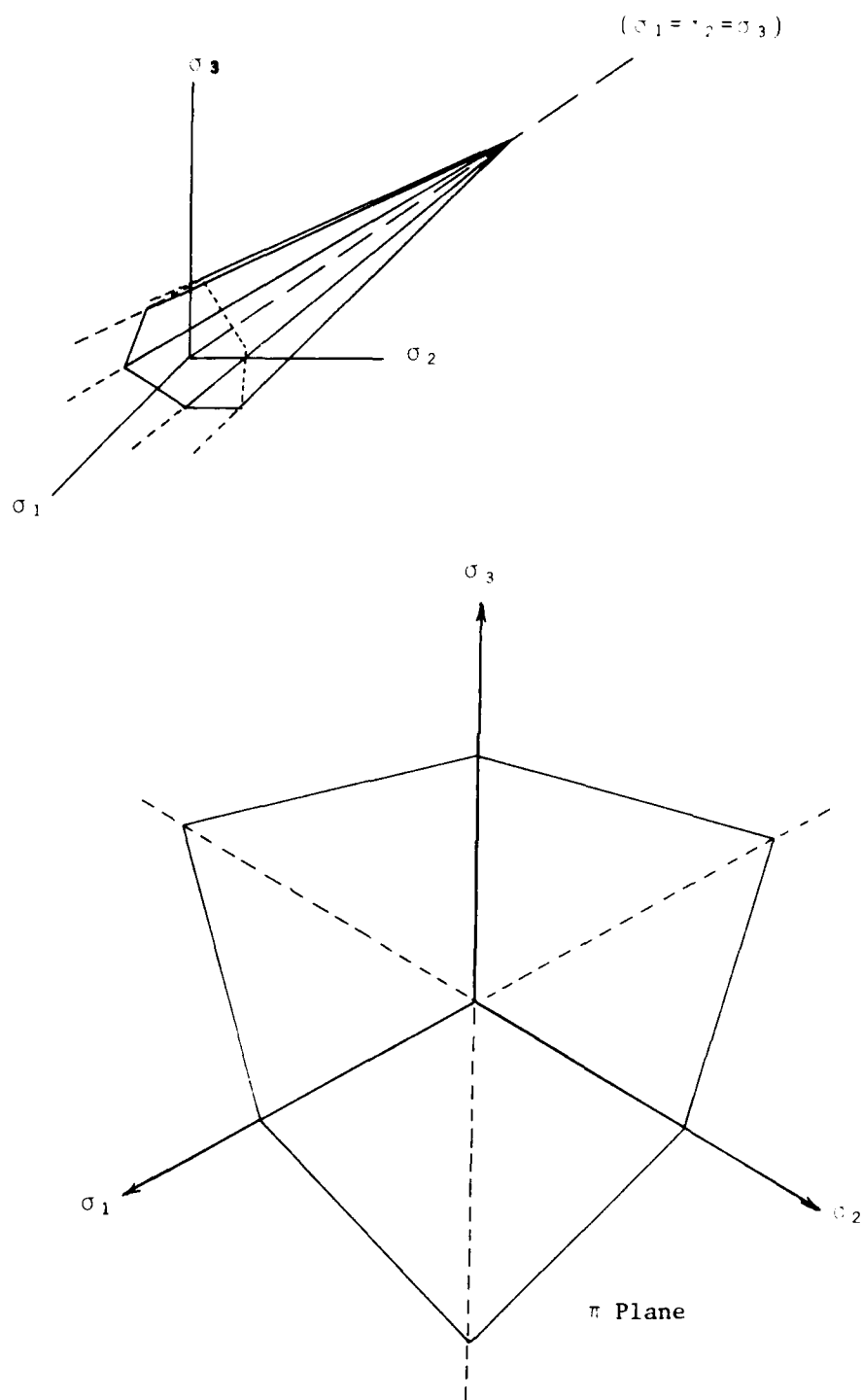


Figure B-2. Mohr-Coulomb Yield Function.

To put the yield function into invariant form, it is convenient to use a set of stress invariants introduced by Nayak and Zienkiewicz [11]. These new invariants (σ_m , $\bar{\sigma}$, θ_o) are related to the conventional invariants (J_1 , J_2 , J_3) by the following:

$$\sigma_m = \frac{1}{3} J_1$$

$$\bar{\sigma} = \sqrt{J_2}$$

$$\theta_o = \frac{1}{3} \sin^{-1} \left\{ \left(\frac{-3}{2} \sqrt{3} \right) \left(J_3 / \bar{\sigma}^3 \right) \right\} \quad \left(\frac{-\pi}{6} \leq \theta_o \leq \frac{\pi}{6} \right)$$

If one considers the π -plane (i.e., the stress space plane perpendicular to the line $\sigma_1 = \sigma_2 = \sigma_3$ and defined by the equation $\sigma_1 + \sigma_2 + \sigma_3 = 0$) located at the origin in stress space (Figure B-3), then θ_o serves as an angular measurement from the line of pure shear over to a stress axis projection. The term $\bar{\sigma}$ acts as a radial measurement outward from the π -plane origin, so $\bar{\sigma}$ and θ_o act as "polar" coordinates in the π -plane.

These invariants lend themselves well to the Mohr-Coulomb yield criterion, which can be expressed as a yield function, F in the following form:

$$F = \bar{\sigma} \cos \theta_o - (1/\sqrt{3}) \bar{\sigma} \sin \theta_o \sin \phi - c \cos \phi + \sigma_m \sin \phi$$

For associated flow rules (as found in NONSAP) plastic flow occurs normal to the yield surface, i.e.,

$$d\epsilon_{ij}^p = \lambda \frac{\partial F}{\partial \sigma_{ij}}$$

where $d\epsilon_{ij}^p$ and λ are the incremental plastic strains and a scalar,

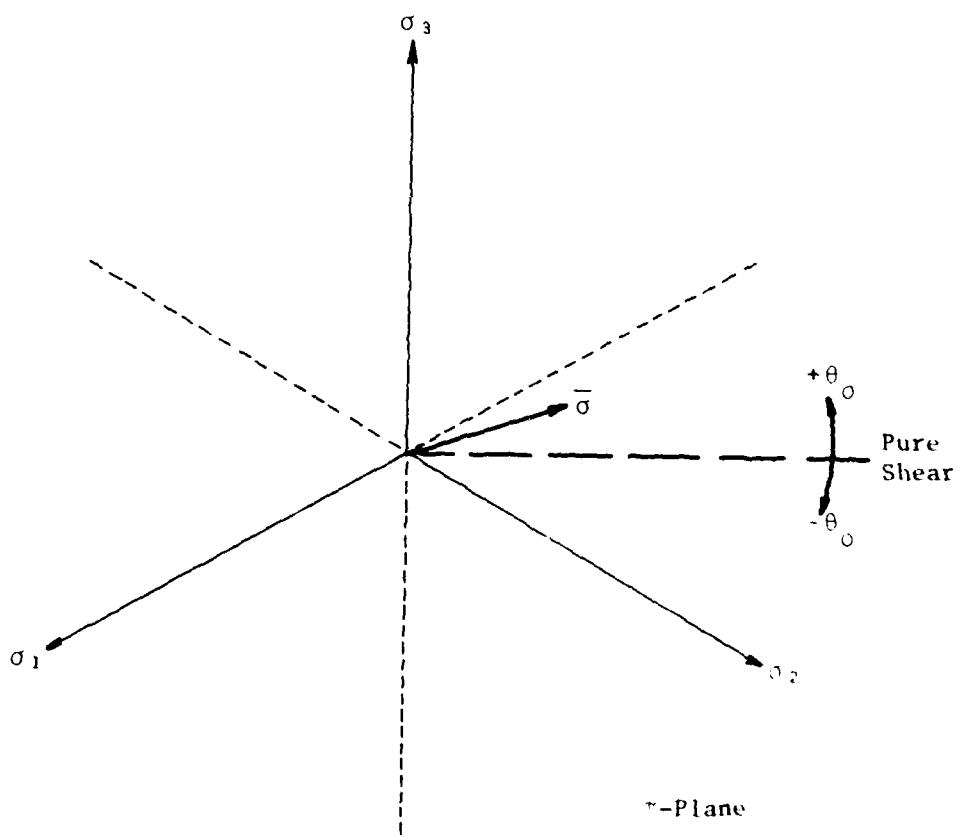
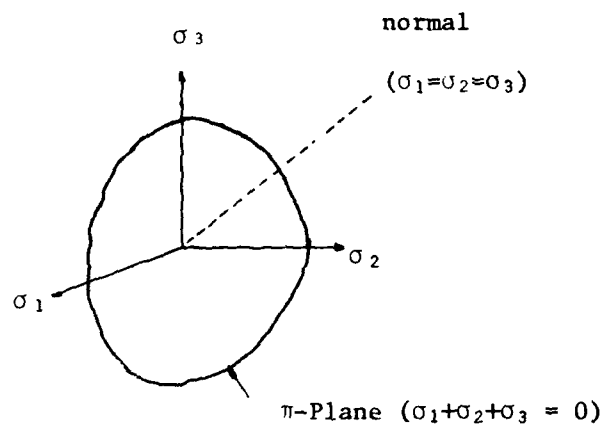


Figure B-3. The π -Plane in Stress Space.

respectively. Once the gradient of the yield surface is determined, the incremental stress-strain relations are defined using the procedures defined in Appendix A.

Using the Nayak and Zienkiewicz invariants, the gradient becomes:

$$\left\{ \frac{\partial F}{\partial \sigma} \right\} = \{q\} = \left\{ \frac{\partial F}{\partial \sigma_m} \right\} \left\{ \frac{\partial \sigma_m}{\partial \sigma} \right\} + \left\{ \frac{\partial F}{\partial \bar{\sigma}} \right\} \left\{ \frac{\partial \bar{\sigma}}{\partial \sigma} \right\} + \left\{ \frac{\partial F}{\partial \theta_o} \right\} \left\{ \frac{\partial \theta_o}{\partial J_3} \right\} \left\{ \frac{\partial J_3}{\partial \sigma} \right\}$$

or simply as:

$$\{q\} = C_1 \{q_1\} + C_2 \{q_2\} + C_3 \{q_3\}$$

where

$$\{q_1\} = \frac{1}{3} \{1, 1, 1, 0, 0, 0\}^T$$

$$\{q_2\} = \frac{1}{2\bar{\sigma}} \{s_x, s_y, s_z, 2\tau_{yz}, 2\tau_{xz}, 2\tau_{xy}\}^T$$

$$\{q_3\} = \left\{ \begin{array}{l} s_y \cdot s_z - \tau_{yz}^2 \\ s_x \cdot s_z - \tau_{xz}^2 \\ s_x \cdot s_y - \tau_{xy}^2 \\ 2(\tau_{xz} \cdot \tau_{xy} - s_x \cdot \tau_{yz}) \\ 2(\tau_{xy} \cdot \tau_{yz} - s_y \cdot \tau_{xz}) \\ 2(\tau_{yz} \cdot \tau_{xy} - s_z \cdot \tau_{xy}) \end{array} \right\} + \frac{1}{3} \bar{\sigma}^2 \left\{ \begin{array}{l} 1 \\ 1 \\ 1 \\ 0 \\ 0 \\ 0 \end{array} \right\}$$

where s_x , s_y and s_z are the stress deviators. The C constants for Mohr-Coulomb are given as

$$C_1 = \sin\phi$$

$$C_2 = \cos\theta_0 \left[1 + \tan\theta_0 \tan 3\theta_0 + \frac{\sin\phi}{\sqrt{3}} (\tan 3\theta_0 - \tan\theta_0) \right]$$

$$C_3 = \frac{(\sqrt{3} \sin\theta_0 + \cos\theta_0 \sin\phi)}{(2\bar{\sigma}^2 \cos 3\theta_0)}$$

A problem arises when the Mohr-Coulomb model is adapted to the numerical modeling. When the stress field is such that any two principal stresses are equal, the stresses lie on a corner of the Mohr-Coulomb yield surface (i.e., $\theta_0 = \pm \frac{\pi}{6}$). At this point, there is a non-unique normal to the surface and the gradient calculations are not defined. Numerically these calculations "blowup" ($C_3 \rightarrow \infty$ as $\theta_0 \rightarrow \pm \frac{\pi}{6}$).

To correct this problem, a Modified Mohr-Coulomb yield surface has been defined which is identical to the ordinary Mohr-Coulomb law except near the vertices of the polygonal surface. Here the corners have been rounded off to a circular arc within a certain tolerance, α_c , of the corner condition, $\theta_0 = \pm \frac{\pi}{6}$ (Figure B-4). The gradient vector is thus fully defined everywhere, including the region where $\theta_0 = \pm \frac{\pi}{6}$. Also, the gradient of a stress state on the yield surface is now a continuous function as the stress state traverses from one flat portion of the surface to another.

The Modified Mohr-Coulomb yield function, F , and gradient constants C_1 , C_2 and C_3 remain the same as Mohr-Coulomb except on the rounded corners, where they can be expressed as

$$F = 2\bar{\sigma}^2 - 2\sqrt{2} \bar{x} \bar{\sigma} \cos\bar{\alpha} + 2\sqrt{2} \bar{\sigma} \cos\bar{\alpha} \frac{P_1}{P_2} \tan\alpha_c - 2 \bar{x} \frac{P_1}{P_2} \tan\alpha_c + \bar{x}^2 \left(1 + \frac{P_1}{P_2^2} \tan^2\alpha_c \right)$$

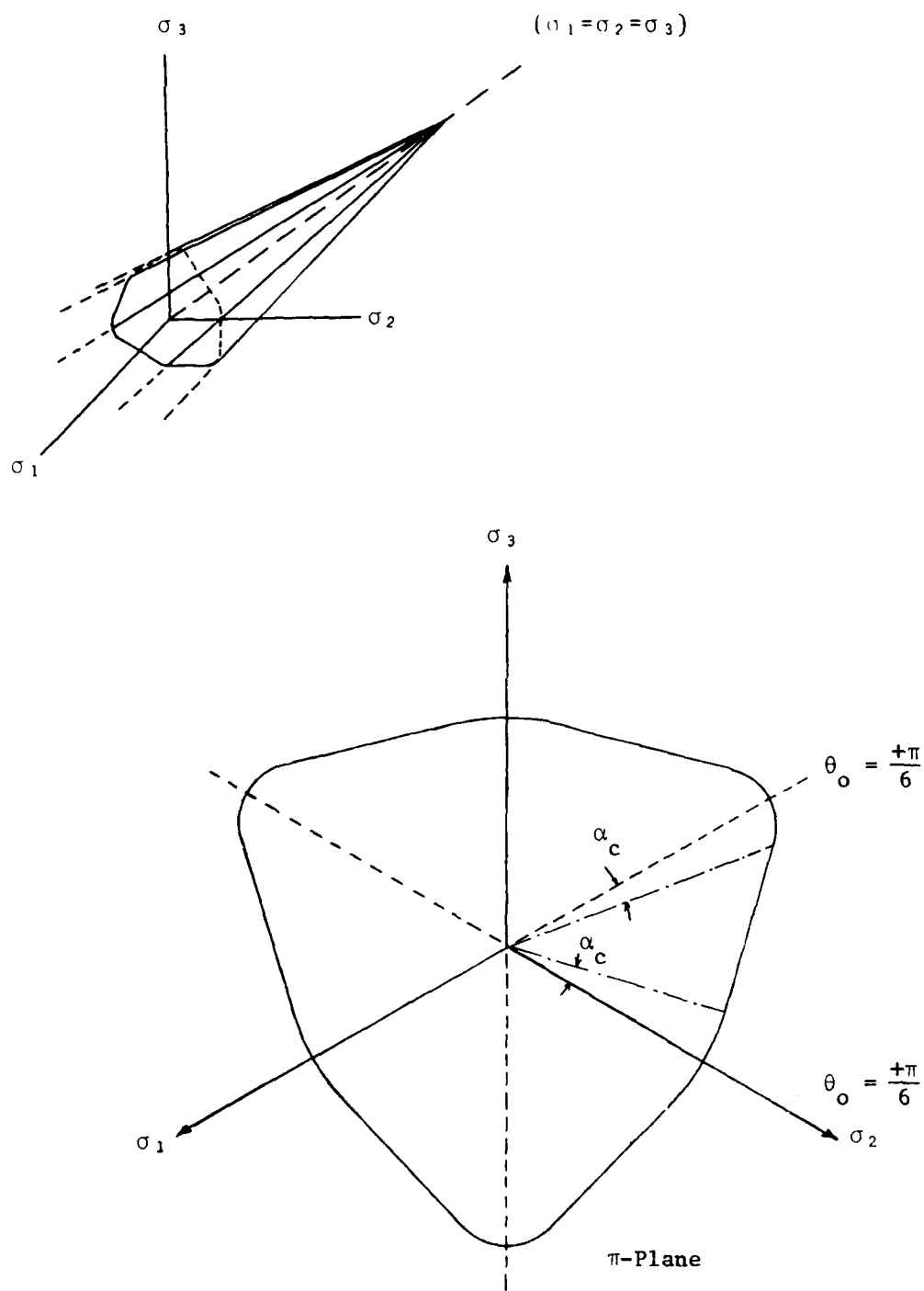


Figure B-4. Modified Mohr-Coulomb Yield Function.

$$C_1 = -2\sqrt{2} \bar{\sigma} \cos\bar{\alpha} (R_1 - R_2) - 2 \bar{x} R_2 - 2 \frac{P_1}{P_2} \tan\alpha_c R_1$$

$$+ 2 \bar{x} R_1 (1 + \frac{P_1}{P_2} \tan^2 \alpha_c)$$

$$C_2 = 4 \bar{\sigma} - R_3 \left(2\sqrt{2} \cos\bar{\alpha} + 3R_4 J_3 \right)$$

$$C_3 = \bar{\sigma} R_4 R_3$$

where for $\theta_0 \rightarrow \frac{\pi}{6}$:

$$\bar{x} = \frac{2\sqrt{6} (c \cos\phi - \sigma_m \sin\phi)}{(3 \mp \sin\phi)}$$

$$\bar{t} = \frac{\pi}{6} + \theta_0$$

$$P_1 = 32(c \cos\phi - \sigma_m \sin\phi)^2 \frac{(3 + \sin^2\phi)}{(3 \mp \sin\phi)^2 (1 \pm \sin\phi)^2}$$

$$P_2 = \frac{(c \cos\phi - \sigma_m \sin\phi)}{(3 \mp \sin\phi)(1 \pm \sin\phi)} \left[(3 \mp \sin\phi) 2\sqrt{2} + (1 \pm \sin\phi) 2\sqrt{6} \tan\alpha_c \right]$$

$$R_1 = \frac{-2\sqrt{6} \sin\phi}{3 \mp \sin\phi}$$

$$R_2 = \frac{-8\sqrt{2} \sin\phi (3 + \sin^2\phi) \tan\alpha_c}{[3 \mp \sin\phi + (1 \pm \sin\phi)\sqrt{3} \tan\alpha_c] (3 \mp \sin\phi)(1 \pm \sin\phi)}$$

$$R_3 = \bar{x} - \frac{P_1}{P_2} \tan\alpha_c$$

$$R_4 = \frac{\pm\sqrt{6}}{\bar{\sigma}^3(3 - 4\sin^2\alpha)}$$

and α_c is the angle measuring the tolerance region for rounding at the corners (see Figure B-4). (Note: The tolerance angle for $\theta_o = \frac{+\pi}{6}$ need not be the same as that for $\theta_o = \frac{-\pi}{6}$.)

For very small rounding of the corners, the Modified Mohr-Coulomb model gives virtually identical results to the ordinary Mohr-Coulomb model when the latter model can be used. The rounded surface, however, is generally applicable, while the ordinary Mohr-Coulomb condition is not. When the rounding region is made larger, the Modified Mohr-Coulomb model attains a form similar to the conical surface in the Drucker-Prager model.

Figures B-5 and B-6 compare the differences in tunnel closures that occurred with Drucker-Prager and Modified Mohr-Coulomb material models. In all cases, the Modified Mohr-Coulomb gave more closure than the Drucker-Prager. This was expected, since the Drucker-Prager material constants were selected so that the Drucker-Prager surface conservatively bounds the Modified Mohr-Coulomb surface. Nevertheless, both models predicted similar trends and differences in closure.

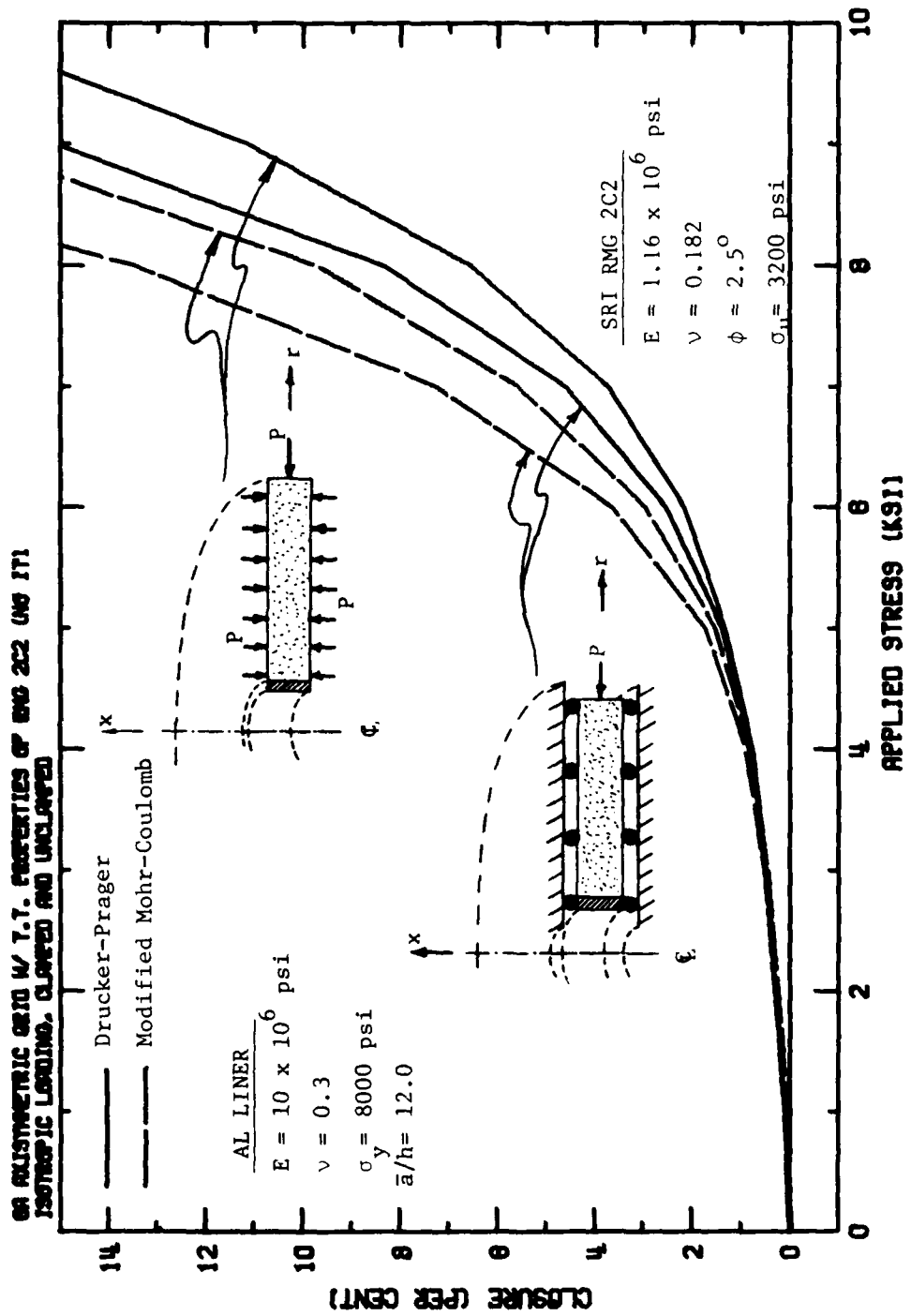


Figure B-5. SRI RMG 2C2 Closure Comparison Between Drucker-Prager and Modified Mohr-Coulomb for Hydrostatic Loading with Both Roller and Stress Confinement.

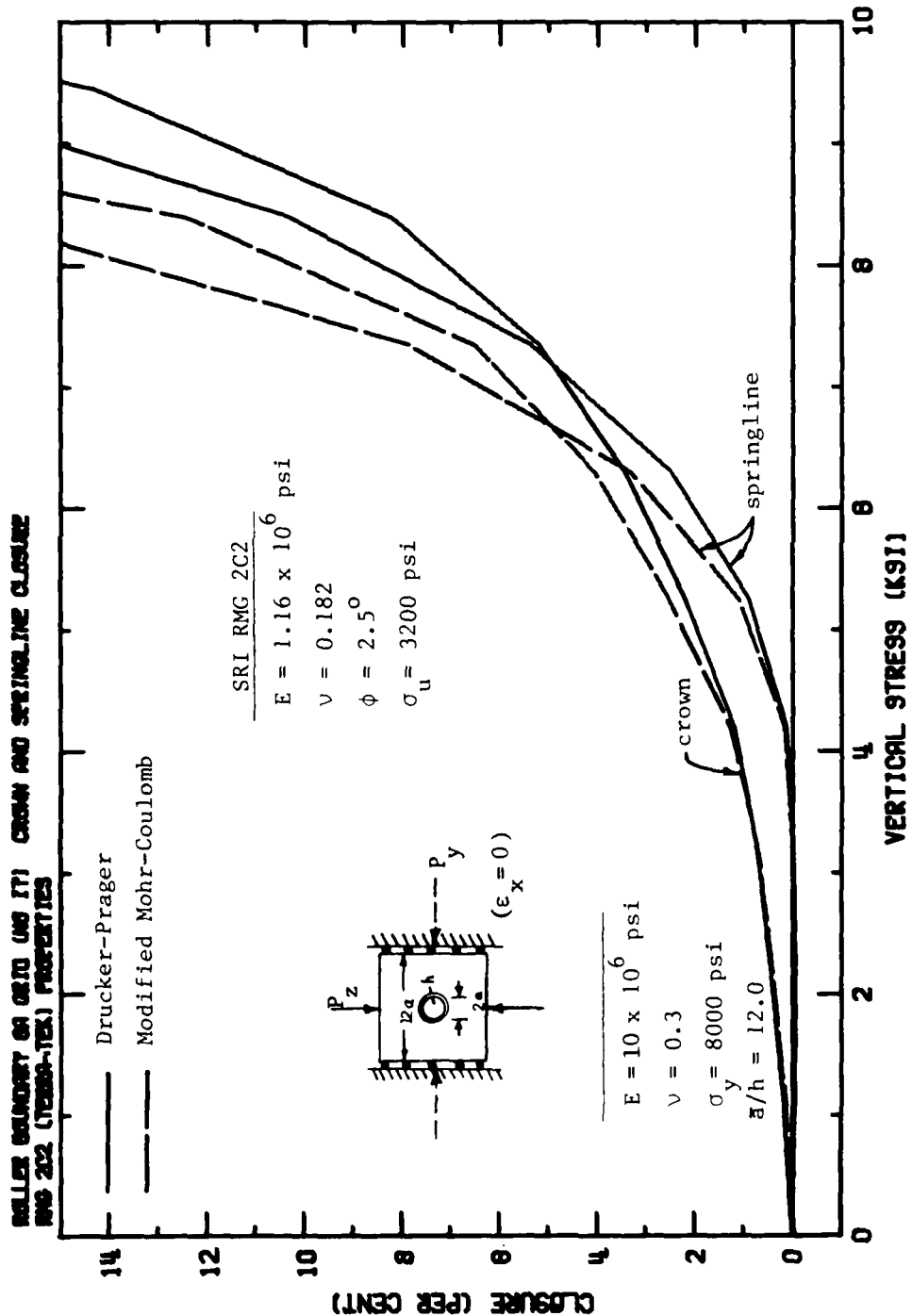


Figure B-6. SRI RMG 2C2 Closure Comparison Between Drucker-Prager and Modified Mohr-Coulomb for Plane Strain Roller Boundary Conditions.

REFERENCES

1. Kennedy, T.C., Zaccor, J.V. and Lindberg, H.E., "Laboratory Investigation of Response of Deep-Based Structures," DNA 3610F, SRI International, October 1975.
2. Kennedy, T.C. and Lindberg, H.E., "Laboratory Investigation of Rock Cavity Reinforcement," DNA 4025F, SRI International, April 1976.
3. Senseny, P.E. and Lindberg, H.E., "Theoretical and Laboratory Study of Deep-Based Structures, Volume II: Model Tests and Analysis of Mighty Epic Structures," DNA 4425F, SRI International, December 1977.
4. Senseny, P.E. and Lindberg, H.E., "Theoretical and Laboratory Study of Deep-Based Structures, Volume I: Triaxial Machine for Static and Dynamic Testing of 12-inch Diameter Rocks," DNA 4425F, SRI International, July 1977.
5. Senseny, P.E. and Lindberg, H.E., "Laboratory Study of Deep-Based Structures in Support of DIABLO HAWK," DNA 4380F, SRI International, February 1978.
6. Bathe, K-J., Wilson, E.L. and Iding, R.H., "NONSAP, A Structural Analysis Program for Static and Dynamic Response of Nonlinear Systems," SESM Report No. 74-3, University of California, Berkeley, February 1974.
7. Bathe, K-J., Ozpemir, H. and Wilson, E.L., "Static and Dynamic Geometric and Material Nonlinear Analysis," SESM Report No. 74-4, University of California, Berkeley, February 1974.
8. Mendelson, A., Plasticity, Theory and Application, MacMillian, New York, 1968.
9. Drucker, D.C. and Prager, W., "Soil Mechanics and Plastic Analysis or Limit Design," Quarterly of Applied Mechanics, Vol. 10, pp. 157-165, 1952.
10. Florence, A.L. and Schwer, L., "Axisymmetric Compression of a Mohr-Coulomb Medium Around a Circular Hole," International Journal for Numerical and Analytical Methods in Geomechanics, Vol. 2, pp. 367-379, 1978.
11. Nayak, G.C. and Zienkiewicz, O.C., "Convenient Form of Stress Invariants for Plasticity," Proceedings of A.S.C.E., Vol. 98, ST4, pp. 949-954, 1972.

DISTRIBUTION LIST

DEPARTMENT OF DEFENSE

Assistant to the Secretary of Defense
Atomic Energy
ATTN: Executive Assistant

Defense Intelligence Agency
ATTN: DB-4C2
ATTN: RDS-3A

Defense Nuclear Agency
ATTN: RAEV
ATTN: STNA
3 cy ATTN: SPSS
4 cy ATTN: TITL

Defense Technical Information Center
12 cy ATTN: DD

Field Command
Defense Nuclear Agency
ATTN: FCTMOF
ATTN: FCPR

Field Command
Defense Nuclear Agency
Livermore Branch
ATTN: FCPRL

Field Command Test Directorate
Defense Nuclear Agency
2 cy ATTN: FCTC, J. Lacomb

Joint Strat Tgt Planning Staff
ATTN: NRI, STINFO Library
ATTN: JLA

Under Secretary of Def for Rsch & Engrg
ATTN: Strategic & Space Sys (OS)

DEPARTMENT OF THE ARMY

Chief of Engineers
Department of the Army
ATTN: DAEN-MCE-D
ATTN: DAEN-RDL

Construction Engineering Rsch Lab
Department of the Army
ATTN: CERL-SOI-L

Harry Diamond Laboratories
Department of the Army
ATTN: DELHD-N-P

U.S. Army Ballistic Research Labs
ATTN: DRDAR-BLT, W. Taylor
ATTN: DRDAR-TSB-S
ATTN: DRDAR-BLT, J. Keefer
ATTN: DRDAR-BLV

U.S. Army Communications Command
ATTN: Technical Reference Division

U.S. Army Concepts Analysis Agency
ATTN: CSSA-AOL

DEPARTMENT OF THE ARMY (Continued)

U.S. Army Engineer Center
ATTN: DT-LRC

U.S. Army Engineer Dist, Omaha
ATTN: MROED-D, C. Distefano
U.S. Army Engineer Div, Huntsville
ATTN: HNDED-SR
3 cy ATTN: C. Huang

U.S. Army Engineer Div, Ohio River
ATTN: ORDAS-L

U.S. Army Engr Waterways Exper Station
ATTN: WESSE, L. Ingram
ATTN: WESSA, W. Flathau
ATTN: WESSS, J. Ballard
ATTN: J. Day
ATTN: Library
ATTN: P. Mlakar
ATTN: J. Drake
ATTN: WESSD, J. Jackson

U.S. Army Nuclear & Chemical Agency
ATTN: Library

DEPARTMENT OF THE NAVY

Chief of Naval Operations
Department of the Navy
ATTN: OP 943

Naval Civil Engineering Laboratory
ATTN: Code LO8A
ATTN: L51, R. Murtha
ATTN: Code L51, J. Crawford

Naval Electronic Systems Command
ATTN: PME 117-211, B. Kruger

Naval Postgraduate School
ATTN: Code 1424, Library

Naval Research Laboratory
ATTN: Code 2627

Naval Surface Weapons Center
ATTN: Tech Library & Info Svcs Br

Naval War College
ATTN: Code E-11

Strategic Systems Project Office
Department of the Navy
ATTN: NSP-43

DEPARTMENT OF THE AIR FORCE

Air Force Institute of Technology
ATTN: Library

Air University Library
Department of the Air Force
ATTN: AUL/LSE

DEPARTMENT OF THE AIR FORCE (Continued)

Air Force Weapons Laboratory
Air Force Systems Command
 ATTN: SUL
 ATTN: NTE, M. Plamondon
 ATTN: NT, D. Payton

Assistant Chief of Staff
Studies & Analyses
Department of the Air Force
 ATTN: AF/SASM
 ATTN: AF/SASM, W. Adams

Ballistic Missile Office
Air Force Systems Command
 ATTN: ENN
 ATTN: MNNH

Deputy Chief of Staff
Operations Plans and Readiness
Department of the Air Force
 ATTN: AFXODC

Deputy Chief of Staff
Research, Development, & Acq
Department of the Air Force
 ATTN: AFRDQI

Foreign Technology Division
Air Force Systems Command
 ATTN: NIIS, Library

Strategic Air Command
Department of the Air Force
 ATTN: NRI, STINFO Library
 ATTN: XPFS

OTHER GOVERNMENT AGENCIES

Central Intelligence Agency
 ATTN: OSWR/NED

Department of the Interior
Bureau of Mines
 ATTN: Tech Lib

Department of the Interior
U.S. Geological Survey
 ATTN: W. Twenhofel
 ATTN: R. Carroll

Department of the Interior
U.S. Geological Survey
 ATTN: D. Roddy

DEPARTMENT OF ENERGY CONTRACTORS

Lawrence Livermore National Lab
 ATTN: G. Smith
 ATTN: H. Heard
 ATTN: L-21, D. Oakley
 ATTN: Technical Info Dept Library

Los Alamos National Scientific Lab
 ATTN: L. Germaine
 ATTN: J. Johnson
 ATTN: B. Killian
 ATTN: MS 364

DEPARTMENT OF ENERGY CONTRACTORS (Continued)

Oak Ridge National Laboratory
 ATTN: Central Rsch Library

Sandia National Laboratories
 ATTN: Library & Sec Class Div

Sandia National Lab
 ATTN: 3141
 ATTN: L. Hill

DEPARTMENT OF DEFENSE CONTRACTORS

Aerospace Corp
 ATTN: Technical Info Services
 ATTN: P. Mathur

Agbabian Associates
 ATTN: M. Balachanda
 ATTN: C. Bagge
 2 cy ATTN: M. Agbabian

Applied Theory, Inc
 2 cy ATTN: J. Trulio

AVCO Research & Systems Group
 ATTN: Library A830

BDM Corp
 ATTN: T. Neighbors
 ATTN: Corporate Library

Boeing Co
 ATTN: M/S 42/37, K. Friddell
 ATTN: J. Wooster
 ATTN: T. Berg
 ATTN: H. Leistner
 ATTN: R. Dyrdahl
 ATTN: Aerospace Library

California Institute of Technology
 ATTN: D. Anderson

California Research & Technology, Inc
 ATTN: S. Schuster
 ATTN: K. Kreyenhagen
 ATTN: Library

California Research & Technology, Inc
 ATTN: D. Orphal

University of California
 ATTN: R. Goodman
 ATTN: N. Cook

Calspan Corp
 ATTN: Library

University of Denver
 ATTN: J. Wisotski

EG&G Wash Analytical Svcs Ctr, Inc
 ATTN: Library

Electromech Sys of New Mexico, Inc
 ATTN: R. Shunk

DEPARTMENT OF DEFENSE CONTRACTORS (Continued)

Eric H. Wang
Civil Engineering Rsch Fac
ATTN: N. Baum

Foster-Miller Associates, Inc
ATTN: J. Hampson for E. Foster

Franklin Institute
ATTN: Z. Zudans

IIT Research Institute
ATTN: Documents Library
ATTN: R. Welch
ATTN: M. Johnson

Institute for Defense Analyses
ATTN: Classified Library

J. D. Haltiwanger Consult Eng Svcs
ATTN: J. Haltiwanger

J. H. Wiggins Co., Inc
ATTN: J. Collins

Kaman Avidyne
ATTN: Library

Kaman Sciences Corp
ATTN: Library

Kaman Tempo
ATTN: DASIAC

Lockheed Missiles & Space Co., Inc
ATTN: T. Geers
ATTN: Technical Information Center

Massachusetts Inst of Technology
ATTN: W. Brace

Merritt CASES, Inc
ATTN: J. Merritt

City College of New York
ATTN: C. Miller

Northwestern University
ATTN: T. Belytschko

Pacific-Sierra Research Corp
ATTN: H. Brode

Pacific-Sierra Research Corp
ATTN: D. Gormley

Pacifica Technology
ATTN: G. Kent

Patel Enterprises, Inc
ATTN: M. Patel

Rand Corp
ATTN: A. Laupa

William Perret
ATTN: W. Perret

DEPARTMENT OF DEFENSE CONTRACTORS (Continued)

Physics International Co
ATTN: Technical Library
ATTN: F. Sauer
ATTN: E. Moore

R & D Associates
ATTN: D. Rawson
ATTN: Tech Info Center
ATTN: J. Lewis
ATTN: R. Port
ATTN: D. Srinivasa
ATTN: P. Haas

Science Applications, Inc
ATTN: Technical Library

Science Applications, Inc
ATTN: Technical Library

Science Applications, Inc
ATTN: W. Layson

Southwest Research Institute
ATTN: A. Wenzel
ATTN: W. Baker

SRI International
ATTN: H. Lindberg
ATTN: B. Holmes
ATTN: G. Abrahamson

Systems, Science & Software, Inc
ATTN: C. Archembeam
ATTN: Library
ATTN: R. Duff
ATTN: D. Grime

Terra Tek, Inc
ATTN: Library
ATTN: H. Pratt

Texas A & M University System
ATTN: J. Handin
ATTN: A. Rychlik

TRW Defense & Space Sys Group
ATTN: Technical Information Center
ATTN: P. Huff
ATTN: N. Lipner

TRW Defense & Space Sys Group
ATTN: E. Wong
ATTN: P. Dai

Universal Analytics, Inc
ATTN: E. Field

Weidlinger Assoc, Consulting Engineers
ATTN: M. Baron
ATTN: I. Sandler

Weidlinger Assoc, Consulting Engineers
ATTN: J. Isenberg